Deriving High Resolution 3D Information using Multibaseline Airborne SAR Interferometry

Dissertation

zur

Erlangung der naturwissenschaftlichen Doktorwürde
(Dr. sc. nat.)

vorgelegt der

Mathematisch-naturwissenschaftlichen Fakultät

der

Universität Zürich

von

Christophe Magnard

von

Carouge (GE)

Promotionskomitee

Prof. Dr. Michael E. Schaepman (Vorsitz)
Dr. Erich Meier (Leitung der Dissertation)
Dr. David Small
Prof. Dr. Uwe Stilla

Zürich, 2016

Front page: Progression of SAR focusing and interferometric processing. Acquisition made using the MEMPHIS sensor in 2012 at *Vordemwald*, Aargau, Switzerland.

This work was approved as a PhD thesis by the Faculty of Science of the University of Zurich in the spring semester 2016.

Doctorate committee: Prof. Dr. Michael E. Schaepman (chair), Dr. Erich Meier (thesis supervisor), Dr. David Small, Prof. Dr. Uwe Stilla.

SUMMARY

Synthetic aperture radar interferometry (InSAR) is a remote sensing technology that can be used to generate topography measurements such as digital elevation models (DEMs). The measurements are characterized by properties that highly depend on the system parameters. These properties include backscatter characteristics, penetration into vegetation, spatial resolution, geolocation accuracy, vertical noise, and coherence.

InSAR sensors have been used operationally on air- and spaceborne platforms to generate moderate resolution DEMs. They are able to cover large areas with a small number of acquisitions, with independence from weather and daylight conditions. Higher, submeter resolution topography measurements are typically achieved using airborne laser scanning (ALS) technology. While now a mature and widely-used technology, ALS uses narrow swaths for high resolution data acquisitions and therefore requires large numbers of acquisitions. InSAR has the potential of achieving high resolution 3D measurements using the appropriate system parameters, and therefore could combine high resolution data acquisition with a large coverage, reducing costs.

Data from an experimental airborne millimeter wave multibaseline InSAR system, the MEMPHIS system, were studied in this work. The datasets yielded decimeter resolution SAR images. The sensor uses the Ka-band wavelength that penetrates only marginally into vegetation, and multiple receiving antennas to combine straightforward phase unwrapping with reduced vertical noise. These unique properties enable the generation of high resolution three dimensional data, with accuracies that approach those of ALS data.

To fully exploit the provided raw data, they first have to be focused into high resolution SAR images. Subsequent interferometric processing yields the topographic information. The work presented here investigated the prerequisites, such as the required navigation data quality and appropriate SAR focusing algorithms, necessary to generate well-focused images, accurate geolocation, and trustworthy interferometric phase values.

SAR focusing and interferometric processing algorithms able to generate highly accurate point clouds or digital surface models (DSMs) are proposed. First a coarse-to-fine (C2F) interferometric phase estimation method is introduced, where interferograms generated using the shorter baselines are only used to help unwrap the interferogram generated using the longest available baseline. A maximum likelihood (ML) phase estimation method was also investigated, taking into account information from all receiving antennas to retrieve a better phase estimation. Signatures of corner reflectors were analyzed in the generated SAR images: measured resolutions yielded values close to the theoretical expectations. The planimetric geolocation accuracy was typically better than 0.1 m, validating the SAR system and focusing algorithm. InSAR DSMs were compared to ALS-based models to validate their absolute vertical accuracy; in grassland areas, the height difference between the ~2 m-resolution InSAR DSMs and the reference ALS models was typically 0 ± 0.25 m. The performance of the ML phase estimation was compared to results based on the C2F algorithm, with the ML method consistently delivering higher accuracies: the noise level using the ML approach was slightly but steadily lower than the noise level obtained using the C2F method.

The potential of InSAR-based point clouds is demonstrated in an application: the point cloud of a forest canopy was generated from multi-aspect multibaseline InSAR data and compared to equivalent products generated using ALS and stereo-photogrammetry techniques. Through a segmentation of the point cloud, single trees were detected and their position, height, and crown diameter estimated. These estimates were compared to reference forestry data. The InSAR, ALS,

and photogrammetry-based point clouds all showed similar geolocation accuracies, with 0.2 – 0.3 m relative shifts. A much more limited penetration into the canopy was observed for both the InSAR and photogrammetry derived point clouds as compared to ALS. Canopy height models agreed very well with each other, with the InSAR height ~1 m lower than those derived from the other point clouds. Most of the large trees were accurately detected, as well as approximately half of the smaller trees, with a localization accuracy typically better than 1 m. Asides from a slight underestimation, the tree heights agreed well with the reference data, and the estimation of the crown diameter was accurate in the mean. Results were more accurate for conifers than for broad-leaf trees. All these results are in line with similar studies that tested ALS data. They validate millimeter wave multibaseline InSAR-data as a reliable alternative for forest monitoring in comparison to other remote sensing techniques such as ALS and stereo-photogrammetry.

In the final chapter, a synthesis of the main findings is presented. The successful use of millimeter wave multibaseline SAR interferometry to carry out reliable and accurate high resolution topography measurements is highlighted, including its application in monitoring forested ecosystems. Limitations are identified: they range from motion compensation errors, to hardware-related severe range sidelobes when illuminating targets with intense backscattering, and to limited penetration into the forest canopy reducing detection of understory trees. Further improvements to the data processing are suggested: a reduction of the range sidelobes using multi-step adaptive pulse compression, an elaborate sample selection for the phase estimation, and the use of SAR tomography. Finally, several potential applications are proposed, such as monitoring and analysis of man-made objects, land cover classification using a combination of InSAR and polarimetric data, or change detection. In the latter case, the inherent 3D geolocation of the points removes the need for a precise external height model, and shadowed areas can be filtered using a coherence threshold, reducing the number of false alarms. Through its thorough validation, this work paves the way toward a more operational airborne or possibly spaceborne system that could combine high resolution topography measurements with a wide coverage.

ZUSAMMENFASSUNG

SAR-Interferometrie (InSAR) ist eine Fernerkundungstechnologie, welche topographische Messungen ermöglicht. Diese kann u.a. zur Herstellung digitaler Höhenmodelle (DHM) genutzt werden. Die Eigenschaften dieser Messungen sind in hohem Masse von den Systemparametern abhängig. Sie umfassen das Rückstreuverhalten der elektromagnetischen Wellen, ihre Eindringtiefe in Vegetation, die räumliche Auflösung, die Genauigkeit der Geolokalisierung, das vertikale Rauschen und die Kohärenz.

Flugzeug- und weltraumgestützte Sensoren werden operationell zur Erzeugung von DHMs mittlerer Auflösung eingesetzt. Dabei lassen sich grosse Flächen mit einer geringen Anzahl von Aufnahmen erfassen, unabhängig von Wetter und Tageslichtbedingungen. Topographische Messungen mit höherer Auflösung, z.B. im Sub-meter Bereich, werden in der Regel mittels *Airborne Laserscanning* (ALS) durchgeführt. ALS ist eine ausgereifte und weit verbreitete Technologie, welche aufgrund der begrenzten Streifenbreite eine grosse Anzahl von Aufnahmen erfordert. Demgegenüber verfügt die InSAR-Technologie über das Potential, mit geeigneten Systemparametern hochauflösende 3D-Messungen durchzuführen, welche über eine vergleichbare Auflösuung wie ALS verfügen, jedoch mit dem für Radarsysteme üblichen Vorteil der grossen Abdeckung und geringen Kosten.

In dieser Arbeit wurden Daten des experimentellen, luftgestützten *multibaseline* InSAR-Systems mit der Bezeichnung MEMPHIS verwendet. Es verfügt über eine Dezimeter-Auflösung und arbeitet im Ka-Band, im Bereich der sogenannten Millimeterwellen, welcher sich durch ein geringes Eindringen in Vegetationsdecken auszeichnet. Die mehreren Empfangsantennen erlauben ein unkompliziertes *Phase unwrapping* bei gleichzeitig reduziertem, vertikalen Rauschen. Diese einzigartigen Eigenschaften des MEMPHIS-Systems ermöglichen die Herstellung hochauflösender, dreidimensionaler Daten, mit einer Genauigkeit, die bis heute nur ALS-Systemen sowie der hochauflösenden Photogrammetrie vorbehalten war.

Um den Informationsgehalt der verfügbaren Rohdaten vollständig zu nutzen, müssen diese erst fokussiert und hochauflösende SAR-Bilder erzeugt werden. Die anschliessende interferometrische Verarbeitung liefert zusätzlich die 3D-Information. Die vorliegende Arbeit diskutiert die dazu notwendigen Voraussetzungen, namentlich die erforderliche Qualität der Navigationsdaten und die am besten geeigneten SAR-Fokussierungsalgorithmen. Diese garantieren neben gut fokussierten Bildern eine genaue Geolokalisierung und vertrauenswürdige interferometrische Phasenwerte.

SAR-Fokussierungs- und interferometrische Verarbeitungs-Algorithmen werden präsentiert, um hochgenaue Punktwolken sowie digitale Oberflächenmodelle zu erzeugen. Dazu wird zunächst ein interferometrisches *coarse-to-fine* (C2F) Phasenschätzverfahren eingeführt, bei dem Interferogramme, die mit kürzeren Basislinien erzeugt wurden, lediglich zum *Unwrappen* des Interferogramms mit der längsten Basislinie verwendet werden. Anschliessend wird ein *Maximum-Likelihood* (ML) Verfahren vorgestellt, welches die Informationen aller Empfangsantennen berücksichtigt, um eine verbesserte Phasenschätzung zu erhalten.

Zur Qualitätssicherung wurden die Signaturen von Winkelreflektoren in den SAR-Bildern untersucht: Die damit gemessenen, räumlichen Auflösungen ergaben Werte nahe an den theoretischen Erwartungen. Zusätzlich wurde das SAR-System und der Fokussierungs-algorithmus mit Hilfe der Geolokalisierungsgenauigkeit validiert; diese war in der Regel besser als 0.1 m. Die InSAR-Oberflächenmodelle wurden mit ALS-basierten Modellen verglichen, um die absolute vertikale Genauigkeit zu validieren; für Wiesen- und Ackerflächen lag die Höhendifferenz nahe bei Null, mit einer Streuung von ± 25 cm. Desweiteren wurden die Resultate

aus der ML-Phasenschätzung mit Ergebnissen des C2F-Algorithmus verglichen. Die ML-Methode lieferte durchwegs höhere Genauigkeiten: Das Rauschen war geringfügig aber stets niedriger als dasjenige der C2F-Methode.

Das Potenzial von InSAR-basierten Punktwolken wird anhand einer Anwendung gezeigt: Dazu wurde ein Waldbestand aus unterschiedlichen Richtungen beleuchtet und aus den resultierenden *multibaseline* InSAR-Daten Punktwolken hergeleitet. Diese wurden mit äquivalenten Produkten aus ALS und Stereo-Photogrammetrie verglichen. Die InSAR-, ALS-, und Photogrammetrie-basierten Punktwolken zeigten mit 0.2 – 0.3 m Relativverschiebungen ähnliche Genauigkeiten in der Geolokalisierung. Im Vergleich zu ALS wurde für die InSAR- und Photogrammetrie-basierten Punktwolken ein deutlich geringeres Eindringen in die Vegetationsdecke beobachtet. Die erstellten *Canopy*-Höhenmodelle (Maximalhöhen) stimmten für alle drei Verfahren jedoch gut miteinander überein, wobei die InSAR-Höhe ca. 1 m tiefer lag als die der anderen.

Durch eine Segmentierung der Punktwolke wurden anschliessend einzelne Bäume detektiert und deren Positionen, Höhen und Kronendurchmesser geschätzt. Diese Parameter wurden mit forstwirtschaftlichen Referenzdaten verglichen. Ein Grossteil der grossen Bäume sowie rund die Hälfte der kleineren Bäume wurden richtig erkannt, wobei der Lokalisierungsfehler typischerweise unter 1 m lag. Abgesehen von einer leichten Unterschätzung stimmten die Baumhöhen des InSAR-Verfahrens mit den Referenzdaten gut überein. Eine gute Übereinstimmung wurde auch bei der Schätzungen des mittleren Kronendurchmessers erreicht. Es zeigt sich, dass die Ergebnisse bei Nadelbäumen genauer sind als bei Laubbäumen. Alle diese Ergebnisse weisen eine hohe Übereinstimmung mit vergleichbaren ALS-basierten Studien auf. Sie bestätigen, dass *multibaseline* InSAR-Daten bezüglich Genauigkeit und Zuverlässigkeit eine valable Alternative für die Waldüberwachung darstellen.

Im letzten Kapitel wird eine Synthese der wichtigsten Ergebnisse vorgestellt. Der erfolgreiche Einsatz von *multibaseline* Millimeterwellen SAR Interferometrie zur präzisen und hochauflösenden Topographiemessung einschliesslich der Anwendung zur Beobachtung von Waldökosystemen wird hervorgehoben. Einschränkungen werden identifiziert: Sie reichen von der anspruchsvollen Bewegungskompensation über *hardware*-bedingte Radar-Nebenkeulen bis hin zur begrenzten Eindringtiefe in Vegetation mit der damit einhergehenden Reduktion der Detektionsrate für das Unterholz. Darüber hinaus werden weitere Verbesserungen der Datenverarbeitung vorgeschlagen. Dazu zählen u.a. eine Reduzierung der *Range*-Nebenkeulen durch mehrstufige, adaptive Pulskompression, eine sorgfältige Stichprobenauswahl für die Phasenschätzung, und die Verwendung von SAR-Tomographie. Abschliessend werden mehrere potenzielle Anwendungen vorgeschlagen, wie z.B. die Beobachtung und Analyse von künstlichen Objekten, die Klassifizierung der Landbedeckung mit einer Kombination aus InSAR und polarimetrischen Daten, oder das Potential zum Detektieren von Veränderungen bei zeitlich versetzten Aufnahmen (*Change Detection*). Im letzteren Fall ersetzt die inhärente 3D-Geolokalisierung der Punkte den Bedarf eines präzisen, externen Höhenmodells. Eine Begrenzung der Kohärenz erlaubt das einfache Ausmaskieren von Schattenflächen und damit eine substantielle Reduktion der Falschalarmrate. Die im Rahmen dieser Arbeit durchgeführte Validierung ebnet den Weg in Richtung eines operationellen flugzeug- oder möglicherweise weltraumgestützten Systems, das hochauflösende Topographiemessungen mit einer grossräumigen Abdeckung kombinieren lässt.

TABLE OF CONTENTS

1 INTRODUCTION

1.1 Remote sensing using synthetic aperture radar interferometry

Synthetic aperture radar interferometry (InSAR) is a remote sensing technique that combines two or more SAR measurements acquired using spatial baselines oriented either in the cross-track or along-track directions. The phase difference between these measurements is computed to generate additional information: in the case of a cross-track baseline, this phase difference contains information about the topography of the mapped area, while in the case of an along-track, temporal baseline, movements or changes in the mapped area can be detected.

This thesis deals with the cross-track case, to obtain topography measurements. A first report of that technique was published by (Graham, 1974). It was then developed and used on space- and airborne platforms. Research based on ERS-1 in the 1990s was critical in developing the technology (Small et al., 1995). Operational spaceborne InSAR measurements from the SRTM (Farr et al., 2007) and TanDEM-X (Krieger et al., 2007) missions resulted in global digital elevation models (DEMs) covering most of the Earth surface. Taking advantage of their increased flexibility, InSAR measurements were achieved with several airborne platforms such as the CCRS Convair 580 (Gray & Farris-Manning, 1993), E-SAR (Horn, 1996), AeS-1 (Wimmer et al., 2000), GeoSAR (Hensley et al., 2001), mainly for experimental purposes. An exhaustive review of the InSAR processing techniques, systems, applications and limitations was published by (Rosen et al., 2000).

Techniques such as airborne laser scanning (ALS) (Wehr & Lohr, 1999), stereo-photogrammetry (James & Robson, 2012) and radargrammetry (Capaldo et al., 2011) can also provide topography measurements, each with strengths and weaknesses. The InSAR technique keeps the same advantages as the SAR technique: it has a low sensitivity to weather and seasonal conditions and its spatial resolution is independent of the range distance, which gives the possibility to cover large areas with high resolution and to design spaceborne missions with properties similar to airborne systems.

Potential applications are influenced by the system characteristics: the wavelength defines the penetration depth into vegetation, snow or even ground layers, as well as the scattering mechanisms that occur given various ground roughnesses. The penetration depth and scattering mechanisms are also influenced by the wave polarization; the PolInSAR technique combining multiple polarizations and interferometry can thus be used to estimate vegetation height (Papathanassiou & Cloude, 2001). The range resolution depends on the system bandwidth. The azimuth resolution is inversely proportional to the carrier frequency and the synthetic aperture length. At the same time, a long synthetic aperture is more sensitive to short-term movements on the ground, such as wind-blown trees. The vertical resolution is influenced by the baseline length and the wavelength.

Recent advances in electronics, computational power and navigational systems gave rise to airborne InSAR systems able to perform high resolution measurements in three dimensions. This thesis focuses on the data delivered by such a system: the Millimeterwave Experimental Multifrequency Polarimetric High-resolution Interferometric System (MEMPHIS) (Schimpf et al., 2002).

1.2 MEMPHIS airborne multibaseline millimeter wave system and data characteristics

All the multibaseline millimeter wave InSAR data used in this dissertation were acquired by the MEMPHIS system. The system characteristics were therefore a crucial component of the research that was carried out. They also constrained the potential applications. The experimental data were acquired over the course of several field campaigns; basic knowledge of some of their practicalities is useful for understanding the studies presented in Chapters 2 – 4.

Fig. 1.1 Left: C-160 Transall. Right, from top to bottom: infrared camera, Ka- and W-band InSAR antennas (covered by polycarbonate dielectric lenses, used to reduce the azimuth beam width).

1.2.1 System characteristics

MEMPHIS is an experimental SAR system developed and operated by Fraunhofer/FHR (Wachtberg, Germany), usually installed onboard a C–160 Transall airplane. The SAR antennas are installed at the rear left parachute door, as shown in Fig. 1.1. While this thesis only deals with the Ka-band (35 GHz) InSAR antenna, monopulse and polarimetric antennas can also be installed for other applications such as GMTI or man-made object detection, and the MEMPHIS system can also operate in W-band at 94 GHz.

The Ka-band carrier frequency corresponds to a wavelength of 8.6 mm. Millimeter waves barely penetrate into vegetation, snow or soil, and are backscattered by surfaces of even low roughness that tend to predominantly scatter forward specularly at longer wavelengths. Their use in an InSAR system allows the generation of surface models in sand, snow- or ice-covered areas, returning the crown height in forests.

The choice of the baseline in SAR interferometry is a trade-off between two main phenomena. The sensitivity to phase errors is inversely proportional to the perpendicular baseline (Rosen et al., 2000): the larger the perpendicular baseline, the lower the sensitivity to a constant level of noise and the better the height resolution that can be obtained. At the same time, the larger the baseline, the smaller the ambiguity height (the height corresponding to a 2π interval, see Section 1.3.2). Phase unwrapping of data acquired with small ambiguity heights/large baselines is a difficult task.

MEMPHIS Ka-band InSAR antennas use one transmitting and four receiving horns aligned vertically (see Fig. 2.1), forming baselines with a set of lengths. The shortest baseline results in a large, easy-to-unwrap ambiguity height (~208 m), and high sensitivity to the phase noise. The longest baseline produces a small, difficult to unwrap ambiguity height (~42 m), but has low sensitivity to the phase noise. With this setup, the combination of all baselines can be used to simplify the phase unwrapping process. Note that increasing the baseline also increases the spatial decorrelation, which results in higher phase noise. In the MEMPHIS case, even the longest baseline is relatively short and is hardly affected by this phenomenon.

At the time of MEMPHIS development in the middle of the 1990s, only moderately large bandwidths were available due to hardware limitations on the sampling rate. To overcome these limitations, a stepped-frequency chirp was chosen. Therefore, MEMPHIS signals are transmitted through 8 linear chirps, each with 200 MHz bandwidth and carrier frequencies separated by 100 MHz, to build up a 900-MHz full bandwidth. The full bandwidth results in a slant range resolution of 0.167 m. The theoretical azimuth resolution is 0.082 m. While InSAR processing requires multilooking, effectively reducing the spatial resolution, the resulting spatial resolution is typically approx. 0.4 to 2 m, i.e., similar to that from ALS systems. This opens up new perspectives for InSAR systems in the generation of high resolution digital surface models (DSMs) and the detection and mapping of meter-sized objects.

MEMPHIS was recently complemented with high quality navigation data: the combination of differential GPS (DGPS) and inertial measurement unit (IMU) data provides extremely precise and accurate positioning, velocity and attitude measurements. These data enable a straightforward SAR and InSAR processing of MEMPHIS data, effectively removing a need for complicated autofocus or multisquint techniques that were required with other airborne systems.

1.2.2 Potential applications

The characteristics of the MEMPHIS InSAR system enable applications e.g. in topographic mapping, monitoring ecosystems, change detection, and 3D-mapping such as:

- Generation of high resolution DSMs and canopy height models (CHMs).
- Single tree detection and tree parameter estimation.
- Observation of vegetation, snow and ice levels compared to reference levels.
- Use of the third dimension and coherence to improve robustness in change detection.
- Mapping and estimation of the shape and dimensions of meter-sized man-made objects.

1.2.3 Data acquisition campaigns

While the acquisition campaigns were carried out over many different areas, they contained recurrent characteristics:

- Before each campaign, the transmitted signal was measured in a static setup, using a corner reflector. These types of calibration measurements are useful to ensure high quality range compression.
- Each acquisition was carefully planned including altitude, start and end position; InSAR acquisitions were typically flown along straight lines.
- Corner reflectors were placed at diverse locations in the test site. Their positions were measured using DGPS. They were used to calibrate and ensure high geolocation accuracy and focusing quality.
- In each InSAR campaign, series of acquisitions were planned over “featureless” areas such as grasslands to be used for phase calibration. In some cases, the test site itself was found to be suitable to assist in achieving such calibration.
- “Ground truth” data were documented; they consisted mainly of pictures, annotated with the positions where they were taken.
- These campaigns involved many people and institutions: e.g., pilots, sensor operators, technical staff for preparing the airplane and installing the sensor, air traffic controllers, office of communication, workforce preparing test sites.

Hence, the acquisition campaigns were very carefully planned and executed, and represented a demanding effort. They enabled a thorough quality control of all collected data and measured values.

1.3 Data processing

A fundamental element of this thesis is the effort to exploit the source data in an optimal way. It affects all processing steps, from those responsible for focusing the raw data, to producing 3D data through the interferometric processing, to the application-oriented treatment of generated point clouds.

1.3.1 Focusing SAR data

SAR data focusing is a two-step process: the data are first focused in the range direction and then in the azimuth direction. As MEMPHIS uses a stepped-frequency bandwidth, the range compression also has to include the reconstruction of the full bandwidth. The SAR focusing process is summarized in Fig. 1.2. A short description of the processing stages is given next, including characteristics of methods typically used for transforming between them.

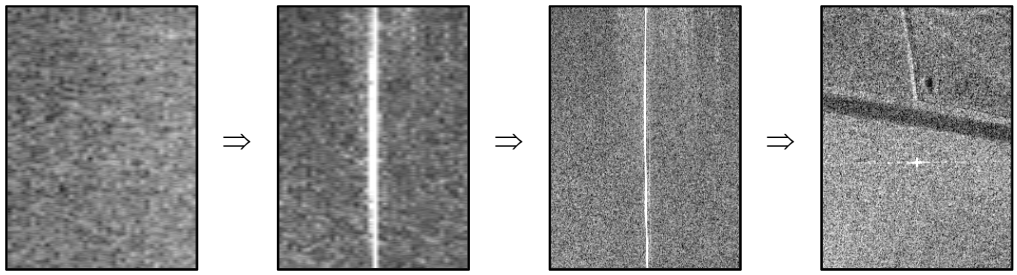

Fig. 1.2 Amplitude images of MEMPHIS Ka-band data showing a corner reflector and its surroundings: (a) raw data of a single chirp, (b) range-compressed data of a single 200 MHz chirp, (c) range-compressed data using the reconstructed 900 MHz stepped-frequency bandwidth, (d) range-compressed and azimuth-focused image. The horizontal and vertical axes correspond to the range and azimuth directions, respectively. Dimensions: ~30 × 51 m.

(a) Range compression: Conventionally, range compression is carried out using a matched filter: the received signal is correlated with the transmitted signal (Curlander & McDonough, 1991). The transmitted signal can either be synthetically generated or measured; in the latter case, using a so-called chirp replica, better results are typically achieved. Alternatively, range compression can be achieved with a multi-step adaptive processing using, e.g., adaptive pulse compression (Blunt & Gerlach, 2006) or the Capon minimum variance method (López-Dekker & Mallorquí, 2010). They are computationally heavy algorithms, and typically provide results with lower sidelobes at the cost of a slightly decreased SNR.

(b) Stepped-frequency processing: The synthesis of the full stepped-frequency bandwidth can either be achieved directly using the raw data or after range compression of the individual chirps. The underlying process is a concatenation of the bandwidth parts in the time or frequency domain (Lord, 2000; Schimpf et al., 2003). Depending on the method used, the results differ in the achieved resolution and level of the sidelobes.

(c) Azimuth compression: Azimuth focusing is carried out either in the time or frequency domain.

Algorithms working in the time domain can handle non-linear trajectories (Frey et al., 2009); they are often the best choice for light, unstable platforms strongly affected by atmospheric conditions or when flexible acquisition trajectories are desired. In the past, the computational load was a strong disadvantage of time domain algorithms; however, fast computation is now achieved thanks to highly parallelized computing in graphics processing units (GPUs).

For InSAR applications, the phase-to-height transformation is not straightforward: for each resolution cell, a very accurate estimation of the sensor position and baseline are required to be able to calculate a point's height and position. As an alternative, voxel-based tomoSAR algorithms such as Capon or MUSIC can also be considered in combination with time domain azimuth focusing (Capon, 1969; Schmidt, 1986; Frey & Meier, 2011).

Frequency domain algorithms require linear acquisitions at constant velocity; minor deviations are dealt with in a motion compensation step. An ideal, linear flight path with constant velocity is calculated, typically using a linear fit of the actual navigation data. The deviations of the actual trajectory compared to the idealized linear flight path are computed, and their expected effect on the SAR data is compensated. Both extended chirp scaling (Moreira et al., 1996) and extended Omega-K (Reigber et al., 2006) algorithms can handle range- and topography-dependent motion compensation for high quality focusing. For InSAR applications, the linearized flight path can then be used in combination with the interferometric phase for a straightforward calculation of the 3D coordinates of the backscattering element. For improved accuracy, compensation of second order effects and approximation errors also requires accurate estimation of the sensor position and baseline at each resolution cell.

Autofocus algorithms used to be necessary to focus data with high quality in the azimuth direction (Wahl et al., 1994). For MEMPHIS data, the accuracy and sampling rates of the available navigation data were so high that no autofocus was necessary for high quality focusing of the SAR data.

1.3.2 Interferometric processing

The interferometric processing can be split into three main tasks: calculation of the interferometric phase, phase unwrapping, and phase-to-height conversion. The results of these tasks are illustrated in Fig. 1.3.

(a) Interferometric phase calculation: In the case of a single baseline, the calculation of the interferometric phase is a well-known equation. Concretely, the goal is to retain as much useful information as possible. The range-compressed and azimuth-focused SAR data, also called single look complex (SLC) data, are typically oversampled by a factor of two, to account for the increased bandwidth linked to the multiplication of two complex SLC values and avoid aliasing (Small, 1998). For this, the spectrum has to be centered before carrying out the oversampling to avoid creating artifacts.

For multiple baselines, the phase information from each SLC is used to calculate a combined interferometric phase. Various methods are possible: e.g., using the shorter baselines only to help unwrap the phase from the longest baseline, maximum likelihood (ML) phase estimation, least squares based on the phase alone, least squares weighted by coherence, wavelet domain approach, or maximum a posteriori (Ferretti et al., 1999; Lombardini & Griffiths, 2001; Ferraiuolo et al., 2004). The choice of a method is constrained by the input data characteristics. Optimal integration of information from all receivers should reduce the phase noise.

The resulting phase noise is closely linked to the number of looks: the larger the number of looks, the lower the phase noise (Rodriguez & Martin, 1992). The conventional technique uses a boxcar window, suitable for areas with homogeneous textures. It assumes local stationarity, i.e., all pixels used for the estimation of one interferometric phase value belong to the same statistical distribution. In specific cases, e.g., with man-made objects, the local stationarity assumption does not hold; there, a more elaborate sample selection may be desirable, such as a non-local InSAR technique (Deledalle et al., 2011) or adaptive sample selection (Vasile et al., 2006).

(b) Phase unwrapping: Phase unwrapping reconstructs the physically continuous phase variation by adding $k \cdot 2\pi, k \in \mathbb{Z}$ to each interferometric phase value. Algorithms use neighboring values and phase gradients to calculate optimum values for k (Chen & Zebker, 2001). Multibaseline

InSAR data are partially unwrapped through the phase estimation process; hence, depending on the topography, an additional phase unwrapping step may not always be necessary.

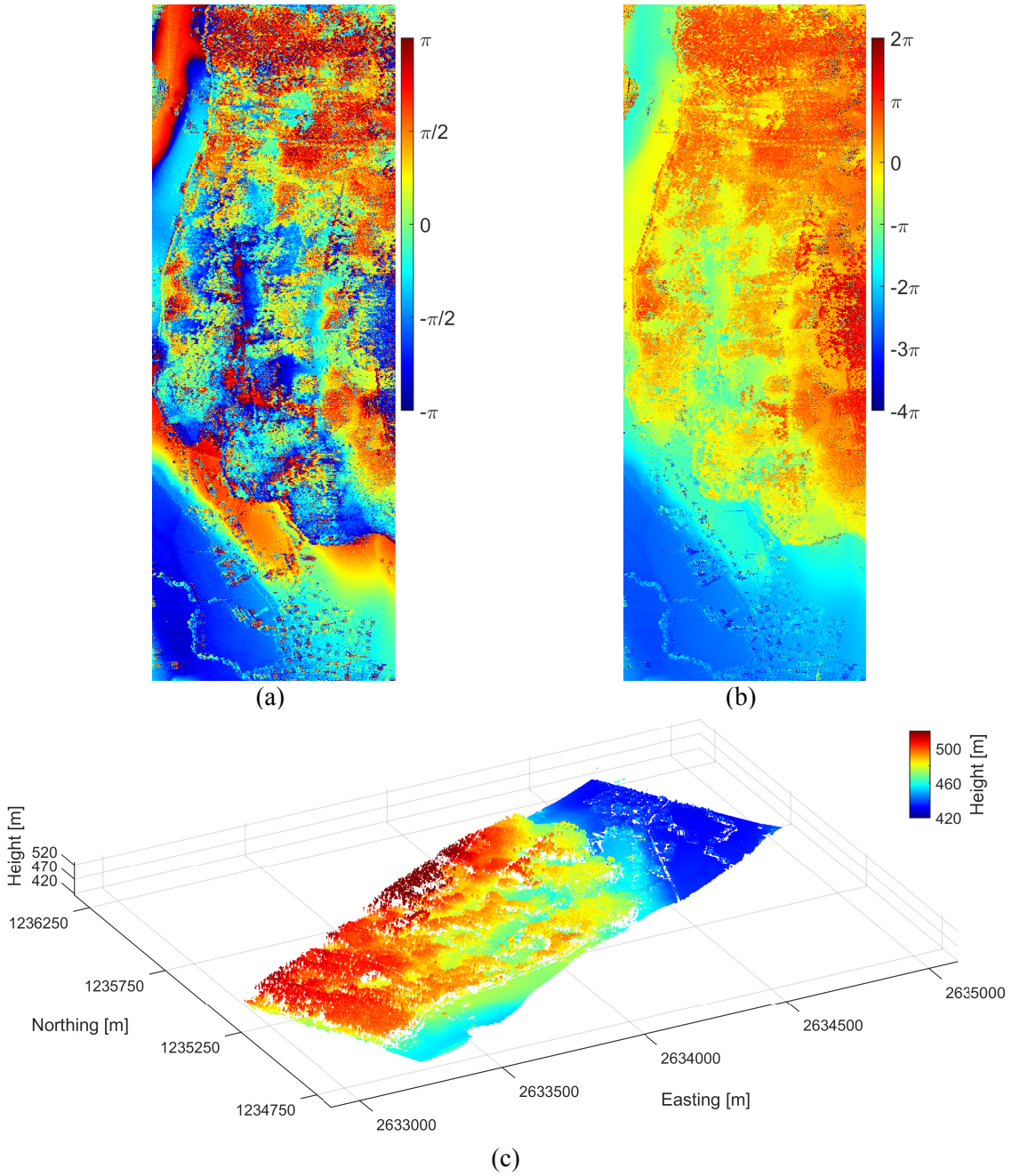

Fig. 1.3 Illustration of the interferometric processing: (a) wrapped interferogram ("flat Earth" phase removed), (b) unwrapped interferogram, (c) point cloud. The illustrations are from a 2012 acquisition over *Vordemwald*, canton *Aargau*, Switzerland. In (a) and (b), range is in the horizontal direction, azimuth in the vertical direction; (c) is in Swiss local map coordinates (LV95).

(c) Phase-to-height conversion: This last step consists of calculating the height and geolocation corresponding to each phase value (Small, 1998; Rosen et al., 2000). Knowing the absolute interferometric phase, the slant range distance, the Doppler frequency and illumination direction (left or right looking), we can compute the vector linking the sensor position to the location of the backscattering element. To achieve this, the relative interferometric phase must be transformed into an absolute measurement by adding a constant phase offset. A precise computation, also

taking into account potential misalignment of the receivers, is best achieved using at least one tie point. To avoid errors linked to approximating the Earth as a flat surface, all calculations should be performed in Cartesian coordinates. For each range-azimuth cell, the corresponding Cartesian coordinates are calculated, which can then be transformed into local map coordinates. The result is a point cloud: it can be resampled into a rasterized DEM or used directly for further analysis.

1.3.3 Point cloud segmentation

High level analysis of point clouds generated from InSAR data can be achieved through a segmentation process (Jain & Dubes, 1988). In general, point cloud segmentation consists of attribution of points to clusters, where points share high similarity within the cluster and high dissimilarity to points in other clusters (Shi & Malik, 2000). The similarity can be defined based on any measurable criterion: e.g., position, coherence, intensity, polarization or texture properties. Fig. 1.4 shows an InSAR-based point cloud of a forested area before and after segmentation.

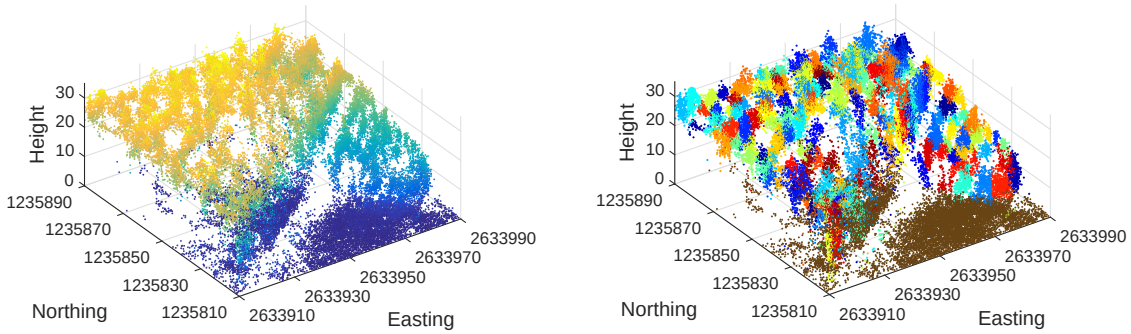

Fig. 1.4 Left: InSAR-based point cloud of a forested area. Right: Segmented point cloud.

1.4 Objective and research questions

The intent of this thesis is to show the ability of an airborne millimeter wave, multibaseline InSAR system to deliver valuable 3D information that can be used, e.g., for accurate, high resolution DSM generation and for forest ecosystem monitoring using point clouds. The work aims to answer the following research questions, encompassing technical and methodological developments as well as a high level application.

Technical and methodological development

The MEMPHIS data were acquired by an experimental system, the raw signal data were provided. To be able to generate valuable 3D information from such raw data, they first have to be sharply focused, the geolocation has to be accurate, and the interferometric phase must depend only on the topography. Achieving such quality presupposes that the raw data, navigation data, and additional meta-data all fulfill strict requirements. Calibration steps have to be designed, the focusing algorithms must be carefully selected and eventually adapted to the provided data characteristics, and an interferometric chain has to be developed that considers potential errors, minimizing them when required. These considerations lead to the first two research questions of the dissertation:

1. What are the prerequisites for generating high resolution images, accurate geolocation, and a trustworthy interferometric phase?
2. Which SAR focusing and interferometric processing algorithms are most suitable to generate point clouds or DSMs?

In the literature, articles can be found about many different algorithms carrying out the interferometric phase estimation from multibaseline data. Their characteristics were studied based on real and simulated spaceborne data, as well as simulated airborne data. Actual airborne single-

pass multibaseline systems are only marginally concerned by typical issues, such as atmospheric effects, temporal decorrelation; they use baselines at least 10 times shorter than the critical baseline. However, issues such as dissimilar receiver properties leading to different antenna phase patterns, nonperfectly aligned phase centers, and inaccuracies in the motion compensation have to be addressed in order to ensure that the data fit the models behind the phase estimation algorithms.

A model-based ML phase estimation combines data from all receiving antennas and weighs their contribution based on the data and their coherence; in theory, it should be the optimal method for estimating the interferometric phase. The third research question therefore studies the possibility of using such a ML phase estimation method with experimental data, including the necessary calibration steps, and evaluates the results by comparing them to a coarse-to-fine method effectively only using the longest available baseline:

3. Can we use a maximum likelihood phase estimation algorithm that takes into account the information from all receiving antennas to achieve better phase estimation, and is it superior to using the longest baseline alone?

Application to forest ecosystem monitoring

Forest ecosystem monitoring at the single tree level is typically achieved using field observations, for sampling purposes. Upscaling these data to cover large areas may lead to large deviations from the reality. A consistent monitoring of larger areas at the single tree level requires remote sensing data; ALS-based point clouds are typically used to detect single trees and derive their positions, heights and crown diameters.

Compared to ALS systems, airborne SAR systems have potential to employ much wider swaths, independent of the resolution. In addition, they are less disturbed by the weather and seasonal conditions. Generating dense InSAR-based point clouds of forest canopies and successfully detecting trees and deriving their characteristics could therefore potentially reduce the costs of forest ecosystem monitoring and increase data availability. This leads to the following research questions:

4. How does the point cloud of a temperate coniferous forest generated from multi-aspect, multibaseline InSAR data compare to equivalent products from other sensors?
5. How do the tree parameters estimated from the segmented point cloud compare to reference forestry data and alternative remote sensing approaches?

Single tree detection using InSAR-based point clouds was recently introduced and validated over sparsely planted broad-leaved trees in an urban park context. The work presented here is the first to be carried out over a long-term forest ecosystem research site, and therefore to be validated using independent, systematically sampled forest inventory data, as well as using ALS and stereophotogrammetry data.

1.5 Structure of the dissertation

Chapter 1 provides the framework required for understanding the aim of the thesis. It introduces the InSAR technique, describes the characteristics, potential applications and limitations of the non-conventional sensor used for all data presented. It familiarizes the reader with the data processing concepts and challenges addressed in Chapters 2 – 4, and introduces the research questions studied later in detail.

Chapter 2 is based on a first author, peer-reviewed article (Magnard et al., 2014) published in *IEEE Journal of Selected Topics in Applied Earth Observations and Remote Sensing*. It presents the SAR focusing method and a first interferometric processing chain using a coarse-to-fine (C2F) phase unwrapping method. It analyzes the focusing quality and geolocation accuracy of the SAR images; the generated DSMs are compared to reference ALS products. Potential errors

are studied and their magnitudes estimated. The publication is self-contained in terms of structure and content.

Chapter 3 is based on a first author, peer-reviewed article (Magnard et al., 2016a) published in *IEEE Journal of Selected Topics in Applied Earth Observations and Remote Sensing*. It studies a ML phase estimation method fully exploiting information from all four receiving antennas and includes improvements in data calibration and processing required by that phase estimation method. Validation is carried out by comparing the phase noise obtained using the ML and C2F phase estimation methods. The publication is self-contained in terms of structure and content.

Chapter 4 is based on a first author, peer-reviewed article (Magnard et al., 2016b) submitted to *Remote Sensing of Environment*. It builds upon Chapters 2 and 3 by using the developed processing method to generate an InSAR point cloud of a forest canopy. Individual trees are detected through a segmentation of the point cloud using the normalized cut technique. For validation, the point cloud is compared to equivalent products from other sensor types, and the detected trees and their estimated position, height and crown diameter are compared to reference forestry data. The publication is self-contained in terms of structure and content.

Chapter 5 compiles the main findings from Chapters 2 – 4 to address the research questions. Following discussion of the results, it provides concluding remarks and an outlook to potential future research and developments.

2 PROCESSING OF MEMPHIS KA-BAND MULTI-BASELINE INTERFEROMETRIC SAR DATA: FROM RAW DATA TO DIGITAL SURFACE MODELS

This chapter has been published as: Magnard, C., Frioud, M., Small, D., Brehm, T., Essen, H., & Meier, E. (2014). Processing of MEMPHIS Ka-Band Multibaseline Interferometric SAR Data: From Raw Data to Digital Surface Models. *IEEE Journal of Selected Topics in Applied Earth Observations and Remote Sensing, 7*: 2927-2941.

For clarity, the paper has been reformatted and the references are listed at the end of the thesis; otherwise, the contents are the same as in the journal article.

Contributions of first author and co-authors: CM, HE, EM designed the study. CM, MF, DS developed the methodology. CM, TB collected the data. CM performed the analysis. CM, MF, DS, EM wrote the paper.

Abstract

MEMPHIS is an experimental millimeter-wave synthetic aperture radar (SAR) system that acquires cross-track multibaseline interferometric data at high resolution in a single pass, using 4 receive horns. In this paper, we present the SAR system and navigation data, and propose a processing chain from the raw data input to a digital surface model (DSM) output. This processing chain includes full bandwidth reconstruction of the stepped-frequency SAR data, azimuth focusing with an Extended Omega-K algorithm, generation of interferograms for each available baseline, phase unwrapping using the multibaseline data, and phase-to-height conversion. The hardware and processing chain were validated through the analysis of experimental Ka-band data. The SAR image resolution was measured with point targets and found to be ~2% and ~15% coarser than the theoretical value in range and azimuth respectively. The geolocation accuracy was typically better than 0.1 m in range and 0.2 m in azimuth. Observed depression angle-dependent interferometric phase errors were successfully removed using a correction function derived from the InSAR data. Investigation of the interferometric phase noise showed the utility of a multibaseline antenna setup; the number of looks and filter size used for the DSM generation were also derived from this analysis. The results showed that in grassland areas, the height difference between the ~2 m-resolution InSAR DSMs and the reference ALS models was 0 ± 0.25 m.

2.1 Introduction

Synthetic aperture radar (SAR) interferometry is a well-known technique that can be used for generating digital elevation models (DEMs). The best-known product is the DEM built using data acquired during the SRTM space shuttle mission (Farr et al., 2007). The current TanDEM-X mission (Krieger et al., 2007) aims to provide a similar product with a higher resolution, height accuracy and almost worldwide coverage. Although airborne cross-track interferometry systems cover smaller areas, they provide flexibility in the acquisition strategy for the area surveyed, in the choice of radar wavelength (e.g. to control the amount of penetration into vegetation canopies), and they lend themselves affordably to higher resolution capabilities. Multipass baselines are most often flown with longer wavelengths, while single-pass interferometry can be employed using wavelengths covering the whole radar spectrum, i.e. ranging from P-band (e.g., GeoSAR (Hensley et al., 2001)) down to millimeters. Many airborne systems have been used for interferometry measurements; fewer are able to generate DEMs with a resolution and accuracy approaching that of airborne laser scanning (ALS) products. F-SAR (Reigber et al., 2012), PAMIR (Brenner & Roessing, 2008), RAMSES (Dubois-Fernandez et al., 2002) and SETHI (Ruault Du Plessis et al., 2011) offer interferometric modes at high resolution in X- and/or Ku-bands. Building on the methods presented within this paper, digital surface models (DSMs) of urban areas were generated from multi-aspect MEMPHIS Ka-band InSAR data through a maximum-likelihood estimation procedure (Schmitt & Stilla, 2014c).

Shorter millimeter waves have a decisive advantage that facilitates the generation of high resolution/high accuracy DEMs: for a defined height accuracy, they require shorter baselines compared to instruments operating at longer wavelengths. This enables the use of a compact hardware made or assembled as a single block/piece (vs. separate antennas attached to various points of the airplane for longer wavelengths). This reduces the relative movements caused by vibrations and their related effects on the InSAR data. A very accurate positioning of the phase centers is possible (related to the manufacturing accuracy). Short baselines also imply easier coregistration: the projection of the baseline on the look vector is proportional to baseline length: for a defined pixel spacing, the displacements between the data received from short baseline antennas are small.

Millimeter waves barely penetrate into vegetation or snow, and are backscattered by surfaces of even low roughness that tend to scatter forward specularly at longer wavelengths. Thus they allow the generation of surface models in sand, snow- or ice-covered areas, returning the crown height in forests. The UAVSAR from JPL has been used to acquire single pass interferometric data at Ka-band (Moller et al., 2011). It is able to survey wide areas at ~2 m resolution using a single baseline. ESA is studying a high resolution interferometric Ka-Band SAR system mounted on a satellite, able to carry out single-pass cross-track interferometry (Dupuis et al., 2013).

Several SAR and interferometric processing methods can be found in the literature. For airborne SAR data, the SAR focusing method should include a range- and topography-dependent motion compensation to achieve high accuracy, as available in the Extended Chirp Scaling (Moreira et al., 1996) and Extended Omega-K (Reigber et al., 2006) algorithms. End-to-end processing from raw data to elevation models using the Extended Chirp Scaling algorithm is described in (Scheiber, 2004). An overview of interferometric processing is provided by (Rosen et al., 2000), and a comparison of algorithms taking advantage of multiple baselines is conducted in (Lombardini & Griffiths, 2001).

In this paper, we introduce the MEMPHIS multibaseline interferometric SAR sensor working at Ka- and W-bands (Schimpf et al., 2002). It combines the possibility to provide high resolution SAR data, multiple baselines for resolving phase ambiguities (Essen et al., 2007) and the particular properties of millimeter wavelengths. We propose an end-to-end processing chain including a reconstruction of the full bandwidth from stepped-frequency transmitted chirps, use of the Extended Omega-K algorithm for the azimuth focusing of the raw data, a robust multibaseline phase unwrapping procedure well adapted to MEMPHIS data, and a phase to DSM conversion taking

advantage of an appropriate coordinate system and the zero-Doppler geometry of the processed SAR data. We present experimental results from two test sites: 1) a flat area; and 2) a mountainous region. We determine the geolocation accuracy and focusing quality of the signatures of corner reflectors, introduce a depression angle-dependent phase correction based on the acquired data, analyze the effects of the phase noise at different multilook levels and median filters, and finally compare the generated DSMs to reference ALS models. The results show that in grassland areas, the height differences between the produced ~2 m resolution DSMs and the reference ALS models averages 0 ± 0.25 m (1σ). We finally analyze possible error sources and estimate their sizes using MEMPHIS acquisition parameters.

The paper is structured as follows: after a description of the system characteristics, the processing method is detailed from raw data extraction to DEM generation. Next, the results of the focusing and interferometric processing using experimental data are reported. A discussion of the results and an outlook to future concerns conclude the paper.

2.2 System characteristics

2.2.1 MEMPHIS InSAR system

MEMPHIS stands for Millimeterwave Experimental Multifrequency Polarimetric High-resolution Interferometric System. It is an experimental SAR system developed and operated by Fraunhofer/FHR (Wachtberg, Germany), usually installed onboard a C–160 Transall airplane (see Fig. 2.1). This paper focuses on the setup for cross-track multibaseline interferometry. It is also possible to use monopulse or polarimetric antennas for ground moving target indication (GMTI) and polarimetry applications (Schimpf et al., 2002; Rüegg et al., 2007).

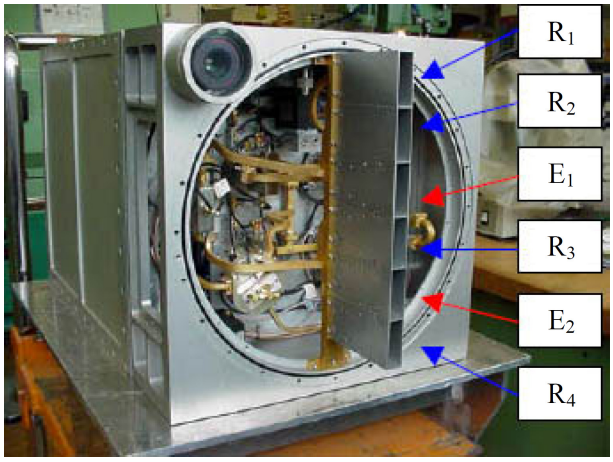

Fig. 2.1 MEMPHIS Ka-band interferometric antenna. E_1, E_2: transmit horns, $R_1 - R_4$: receive horns. Only one transmit horn can be used at a time.

Two carrier frequencies are available, 35 GHz (Ka-band) and 94 GHz (W-band); however, only Ka-band data are presented in this paper. The signal is transmitted as a stepped-frequency chirp through 8 linear chirps, each with 200 MHz bandwidth and carrier frequencies separated by 100 MHz, and used to build up a 900-MHz full bandwidth. MEMPHIS multibaseline interferometric antennas use one transmit and four receive horns. Table 2.1 summarizes some important parameters of the MEMPHIS system.

TABLE 2.1
MEMPHIS SAR SYSTEM PARAMETERS

Carrier frequencies	35 GHz (Ka-band) and 94 GHz (W-band)
Bandwidth	900 MHz (stepped-frequency)
PRF	1500 Hz
Typical airplane velocity	77 m/s
Airplane altitude	300 – 1000 m a.g.l.
Depression angle	20° – 35°
Theoretical rg. resolution	0.167 m
Theoretical az. resolution	0.082 m in Ka-band, 0.061 m in W-band

2.2.2 Navigation data

The precision and sampling rate of the navigation data is a prerequisite for high quality focusing of the SAR data, geolocation and InSAR DEM generation. For the May 2011 campaign presented here, a DGPS system composed of a GPS L1/L2 antenna (AeroAntenna AT2775-41) and a Trimble R7 DGPS receiver running at 20 Hz with a precise iNAV-RQH INS (Dorobantu & Gerlach, 2004) working at 500 Hz from the company iMAR were installed. Their measurements were synchronized through a National Marine Electronics Association (NMEA) communication link and second markers, and with the SAR data through second and event markers.

The lever arms between the DGPS, INS and SAR antennas fixed in operating position were measured using terrestrial surveying methods with a few centimeters accuracy. MEMPHIS SAR antennas are installed at the rear left parachute door of the C-160 aircraft and the system is placed in its operating position during the flight. The absolute position of the antennas, i.e. the lever arms to the SAR antennas, may therefore not be exactly the same for each test site.

The DGPS and INS data were postprocessed together with commercial Novatel Inertial Explorer software, further improving their accuracy. The resulting navigation data contained a few outliers, and were too noisy (in the mm range) for direct use in the SAR processor. A postprocessing step was therefore implemented to remove the outliers and smooth the navigation data through a Kalman filter for the position and velocity and a mean filter for the attitude data.

2.3 Method

MEMPHIS data are delivered by Fraunhofer/FHR in a raw signal format. Steps from raw data extraction and calibration, SAR data focusing, and interferometric processing up to the final digital surface model generation were carried out. Because of MEMPHIS particularities, a dedicated processing chain had to be developed that includes both conventional and MEMPHIS-specific steps. The full processing chain is described in this section, with particular emphasis on azimuth focusing, multibaseline phase unwrapping and phase-to-DSM calculations.

2.3.1 Focusing the raw data

The raw data are first synchronized with the navigation data using the event and/or second markers and then focused by following the processing chain described below.

2.3.1.1 Range compression and stepped-frequency processing

The raw data from each stepped chirp are range-compressed (RC) using chirp replicas through a conventional matched filtering technique. The chirp replicas are generated by measuring the return of a corner reflector in a static ground measurement before the first mission of each campaign. The full bandwidth is reconstructed using an algorithm based on (Wilkinson et al., 1998; Lord, 2000):

1) We apply a range FFT to the range-compressed data corresponding to each stepped chirp.

2) The subspectra are placed side by side in a new array according to the frequencies they contain.
3) The data in regions of overlapping frequencies are coherently added.
4) The full spectrum is filtered with a weighting filter defined as the inverse of the impulse response spectrum. The impulse response spectrum is approximated by stepping together the measurements of a corner reflector return for each frequency step, in our case the range compressed chirp replicas (i.e. the chirp replicas multiplied by their conjugate).
5) The reconstructed spectrum is further filtered with a Kaiser window.
6) An inverse FFT is applied to the reconstructed spectrum.

Possible phase offsets between the frequency steps are corrected using the overlapping frequencies. For each pixel in the range frequency domain, we compute the phase difference between the overlapping frequencies and multiply it by their mean amplitude as a weighting factor. Computing a histogram of the weighted phase difference, its maximum is used as a first phase offset approximation. Finally the weighted average of the phase difference in a $\pi/2$ sector around the first approximation is computed. This process is repeated for the 7 overlapping regions, and the computed phase offsets applied to the data before reconstructing the full spectrum.

2.3.1.2 Azimuth compression with Extended Omega-K algorithm

The azimuth compression is performed with the Extended Omega-K algorithm (Reigber et al., 2006). This algorithm was modified from the conventional Omega-K algorithm (Cafforio et al., 1991) by separating the azimuth compression from the range cell migration (RCM) correction now achieved by a modified Stolt mapping, allowing a second-order, range-dependent, motion compensation. For clarification purposes, we present a corrected derivation of the key focusing equation in the Extended Omega-K reference paper (Reigber et al., 2006).

The modification starts from the Omega-K focusing equation

$$\psi_{\text{tot}}(x,-t_0,r) = \frac{1}{(2\pi)^2}\iint \tilde{\Psi}_{\text{tot}}(k_x,\omega,r=0) \cdot \exp\left[i\left(k_x x - \omega t_0 + \frac{2\omega r}{c}\sqrt{1-\frac{k_x^2 c^2}{4\omega^2}}\right)\right] \mathrm{d}\omega\, \mathrm{d}k_x \tag{2.1}$$

where $\psi_{\text{tot}}(x,-t_0,r)$ is the original wavefield emitted at $t=-t_0$, $\tilde{\Psi}_{\text{tot}}(k_x,\omega,r=0)$ is the 2-D Fourier transform of the data, x is the azimuth position, r is the range position, ω is the radar frequency, k_x is the wavenumber in azimuth and c is the speed of light. The equation can be rearranged as follows:

$$\psi_{\text{tot}}(x,-t_0,r) = \frac{1}{(2\pi)^2}\iint \tilde{\Psi}_{\text{tot}}(k_x,\omega,r=0) \cdot \exp[i(k_x x - \omega t_0)] \cdot \exp\left[ir\sqrt{\left(\frac{2\omega}{c}\right)^2 - k_x^2}\right] \mathrm{d}\omega\, \mathrm{d}k_x \tag{2.2}$$

A zero-term is introduced into equation (2.2), yielding

$$\psi_{\text{tot}}(x,-t_0,r)=\frac{1}{(2\pi)^2}\iint \tilde{\Psi}_{\text{tot}}(k_x,\omega,r=0)\cdot\exp[i(k_x x-\omega t_0)]$$
$$\cdot\exp\left[ir\left(\sqrt{\left(\frac{2\omega}{c}\right)^2-k_x^2}-\sqrt{\left(\frac{2\omega_0}{c}\right)^2-k_x^2}\right)\right] \tag{2.3}$$
$$\cdot\exp\left[ir\sqrt{\left(\frac{2\omega_0}{c}\right)^2-k_x^2}\right]\mathrm{d}\omega\,\mathrm{d}k_x$$

where ω_0 is the carrier frequency. The following change of variables is applied on equation (2.3):

$$k_r'=\sqrt{\left(\frac{2\omega}{c}\right)^2-k_x^2}-\sqrt{\left(\frac{2\omega_0}{c}\right)^2-k_x^2} \tag{2.4}$$

where k_r' is the wavenumber in range. This change of variables represents the modified Stolt mapping, i.e., an interpolation of the data spectrum, different from the conventional Omega-K algorithm. With this change of variables, (2.5) is derived

$$\psi_{\text{tot}}(x,-t_0,r)=\frac{1}{(2\pi)^2}\int\exp[ir\Delta k_r]$$
$$\cdot\int\tilde{\Psi}_{\text{tot}}\left(k_x,\frac{c}{2}\sqrt{(k_r'+\Delta k_r)^2+k_x^2},r=0\right)$$
$$\cdot\exp\left[\frac{-ict_0}{2}\sqrt{(k_r'+\Delta k_r)^2+k_x^2}\right] \tag{2.5}$$
$$\cdot\frac{c}{2}\frac{k_r'+\Delta k_r}{\sqrt{(k_r'+\Delta k_r)^2+k_x^2}}\cdot\exp[i(k_r'r+k_x x)]\mathrm{d}k_r'\,\mathrm{d}k_x$$

where $\Delta k_r=\sqrt{\left(\frac{2\omega_0}{c}\right)^2-k_x^2}$.

For implementation purposes, we finally shift the origin of the r variable through the change of variable $r=r_0+\rho\ =\frac{ct_0}{2}+\rho$. This leads to the final focusing equation

$$\psi_{\text{tot}}(x,-t_0,\rho)=\frac{1}{(2\pi)^2}\int\exp[i(r_0+\rho)\Delta k_r]$$
$$\cdot\int\tilde{\Psi}_{\text{tot}}\left(k_x,\frac{c}{2}\sqrt{(k_r'+\Delta k_r)^2+k_x^2},r=0\right)$$
$$\cdot\exp\left[\frac{-ict_0}{2}\left(\sqrt{(k_r'+\Delta k_r)^2+k_x^2}-k_r'\right)\right] \tag{2.6}$$
$$\cdot\frac{k_r'+\Delta k_r}{\sqrt{(k_r'+\Delta k_r)^2+k_x^2}}\cdot\exp[i(k_r'\rho+k_x x)]\mathrm{d}k_r'\,\mathrm{d}k_x$$

The first exponential term of equation (2.6) is responsible for the final azimuth focusing, and the second integral performs the RCM and frequency-dependent corrections of the focusing function. The second-order, range-dependent, motion compensation is achieved after the RCM and frequency-dependent corrections, and is followed by the final azimuth focusing.

The final azimuth focusing term causes a range spectrum shift in the presence of squint (Bara et al., 2000); it is corrected after the final IFFT by multiplying the signal with the following expression:

$$\exp\left[-i(r_0+\rho)\sqrt{\left(\frac{2\omega_0}{c}\right)^2-\left(\frac{2\pi\cdot f_{\text{Doppler}}}{v_{\text{platform}}}\right)^2}\right] \tag{2.7}$$

where f_{Doppler} is the Doppler centroid frequency and v_{platform} is the linearized sensor speed.

The modified Stolt mapping changes the extension of the responses in the azimuth time-domain. The data are thus corrected accurately in the second-order motion compensation step only for the points of the response at the central carrier frequency. A residual block-wise third-order motion compensation step was demonstrated in (Reigber et al., 2006). This third-order motion compensation corrects errors introduced in the second-order motion compensation at the other frequencies. These errors are very limited with MEMPHIS due to the relatively low bandwidth compared to the carrier frequency.

The Extended Omega-K algorithm can be summarized as follows.

1) First-order motion compensation:
   a) The navigation data are upsampled to the PRF rate.
   b) A linearized track is defined using a least squares method on the position data in global Cartesian coordinates. A constant linearized velocity is defined.
   c) For each echo, the projection of the vector linking the real and the linearized track onto the mid-range line of sight is evaluated. The phase and position of the RC data are corrected according to this value.
   d) The RC data are interpolated in the azimuth direction according to the constant linearized velocity, generating a regular (constant) spatial sampling interval in azimuth.
2) 2-D FFT into the $k_x - \omega$ domain.
3) Modified Stolt mapping:
   a) The interpolation is implemented using B-Spline interpolation method (Unser et al., 1993a, 1993b) done separately on the real and imaginary parts of the 2-D-FFT transformed data.
   b) The data are then multiplied by the second exponential term and last scalar factor of equation (2.6).
4) 2-D IFFT into the $x - r$ domain.
5) Second-order motion compensation: The vector linking the real and linearized track is projected onto the line of sight of each range sample. The difference between this projection and the one applied in the first order motion compensation is used for correcting the phase and position of the data.
6) Block-wise third order motion compensation: the data are processed in small overlapping blocks, each transformed into the $k_x - r$ domain through a FFT. A phase correction is conducted using the expression (22) in (Reigber et al., 2006), and they are transformed back into the $x - r$ domain through an IFFT.
7) Azimuth FFT into the $k_x - r$ domain.
8) Final azimuth focusing by multiplying the data by the first exponential term of (2.6).
9) Azimuth IFFT into the $x - r$ domain.
10) Range spectrum shift by multiplying the data by the expression (2.7).

A range- and topography-dependent motion compensation is achieved, using the central beam approximation: inside all motion compensation steps, the line of sight is computed using a low resolution DEM, i.e., with a resolution below the dimension of the synthetic aperture. For each of the four receiving antennas, we set the lever arm as the vector from the reference position to the center-point between transmitting and receiving antennas, achieving an individual motion compensation for each antenna.

2.3.2 Interferometric processing

The interferometric processing starts from the four single look complex (SLC) images focused as explained above. The data are then processed using the interferometric processing chain described in the following.

2.3.2.1 Interferogram generation

Interferograms are generated for each spatial baseline, i.e., five interferograms are generated for each data take. No coregistration step is needed, as the data are already coregistered precisely enough due to the sensor setup (the antennas are aligned vertically on the support and the support is tilted to be perpendicular to the line of sight, see Section 2.5.1.4). To simplify the phase unwrapping step, a "flat Earth" phase subtraction is applied to the interferograms.

2.3.2.2 Multibaseline phase unwrapping

The choice of the baseline in SAR interferometry is a trade-off between two main phenomena. The sensitivity to phase errors is inversely proportional to the perpendicular baseline. As shown in (Rosen et al., 2000), the sensitivity of the target location $\vec{T}$ to the interferometric phase φ is given by

$$\frac{\partial \vec{T}}{\partial \varphi} = \left(\frac{-\lambda r}{2p\pi B\cos(\theta-\alpha)}\right)\begin{bmatrix}0\\ \cos\theta\\ \sin\theta\end{bmatrix} \tag{2.8}$$

where λ is the wavelength, r the slant range, B the baseline length, θ the off-nadir angle and α the baseline inclination. The parameter p depends on the interferometric mode (p = 1 given a common transmitter, p = 2 for ping pong mode), in the MEMPHIS case, we have p = 1. Thus, the larger the perpendicular baseline $B_\perp = B\cos(\theta-\alpha)$, the lower the sensitivity to a constant level of noise and the better the height resolution that can be obtained. Phase unwrapping of data acquired with small ambiguity heights/large baselines is a difficult task. In the case of height jumps (cliffs, buildings), it can become impossible to locally resolve the height ambiguity. Through the use of *multiple* baselines, one can take advantage of the low sensitivity to phase errors of a large baseline while simplifying the phase unwrapping step. The available baselines with corresponding typical ambiguity heights using the MEMPHIS Ka-band antenna are shown in Table 2.2. The ambiguity height $h_{2\pi}$ is computed using the formula

$$h_{2\pi} = \frac{\lambda r \sin\theta}{pB\cos(\theta-\alpha)} \tag{2.9}$$

A coarse-to-fine approach was chosen for the multibaseline phase unwrapping (Essen et al., 2007; Magnard et al., 2007). For the initial reference, we use the phase given by the interferogram built with the largest ambiguity height, i.e., the shortest baseline. This interferogram may need to be unwrapped, for example in acquisitions over mountainous areas. We use the statistical-cost network-flow algorithm for phase unwrapping SNAPHU (Chen, 2001). The interferograms generated using larger baselines are then successively unwrapped with the help of the phase information from the already unwrapped interferograms.

TABLE 2.2
AVAILABLE BASELINES AND CORRESPONDING TYPICAL AMBIGUITY HEIGHTS FOR THE KA-BAND ANTENNA

Receiving Horns	Baseline [m]	Ambiguity Height [m][a]
R_1, R_2	$B_1 = 0.055$	208.41
R_2, R_3 or R_3, R_4	$B_2 = 0.11$	104.21
R_1, R_3	$B_3 = 0.165$	69.47
R_2, R_4	$B_4 = 0.22$	52.1
R_1, R_4	$B_5 = 0.275$	41.68

[a]At mid-range (1547 m), sensor altitude: 770 m a.g.l., and depression angle: 30°.

The phase unwrapping of the fine interferogram is a two-step process: first the phase of the reference interferogram $\varphi_{\text{j, ref}}$ is calibrated to match the phase of the fine interferogram $\varphi_{\text{j, fine}}$ by computing a phase offset φ_{offset} that minimizes

$$\min_{\varphi_{\text{offset}} \in [-\pi;\, \pi]} \left[\sum_{\text{j}} \left(\left(\varphi_{\text{j, ref}} \cdot \frac{B_{\text{fine}}}{B_{\text{ref}}} + \varphi_{\text{offset}} \right) \bmod 2\pi - \varphi_{\text{j, fine}} \right)^2 \right] \tag{2.10}$$

Where B_{ref} and B_{fine} are the baseline lengths of the reference and fine interferograms and j the running index of the pixels. Once φ_{offset} has been computed, the fine interferogram $\varphi_{\text{j, fine, unw}}$ is unwrapped using the following equation:

$$\varphi_{\text{j, fine, unw}} = \left\lfloor \frac{\varphi_{\text{j, ref}} \cdot \frac{B_{\text{fine}}}{B_{\text{ref}}} + \varphi_{\text{offset}} - \varphi_{\text{j, fine}}}{2\pi} + 0.5 \right\rfloor \cdot 2\pi + \varphi_{\text{j, fine}} \tag{2.11}$$

Possible errors are corrected with the addition or subtraction of 2π, while taking care that the gradients with neighboring pixels stay in the interval $[-\pi - \varepsilon, \pi + \varepsilon]$, where ε is the phase noise. This process is conducted on the first pair of interferograms (with baselines B_1 for the reference interferogram and B_2 for the fine interferogram). It is then repeated using the resulting unwrapped phase map as the reference interferogram and the next interferogram (with baseline B_3) as the fine interferogram, and so on, until the interferogram with the longest baseline is unwrapped. A median filter can optionally be applied to the final unwrapped phase values to further reduce the noise level.

2.3.2.3 Phase to DSM

The "flat Earth" phase is first added back to the unwrapped interferogram. The phase-to-DSM conversion is then realized in two steps, i.e., the position and height corresponding to each pixel are first computed, followed by a filtering and regridding step. The SAR images processed through the chain described in Section 2.3.1 are in a zero-Doppler geometry, as are therefore the interferograms. This allows developing the phase-to-DSM processing method presented here, derived from the one introduced in (Small et al., 1993).

The interferometric phase φ_{j} is described by

$$\varphi_{\text{j}} = \frac{2p\pi}{\lambda} \delta_{\text{j}} - \varphi_{\text{const}} \tag{2.12}$$

where φ_{const} is a constant phase offset binding the measured interferometric phase with the absolute geometric interferometric phase.

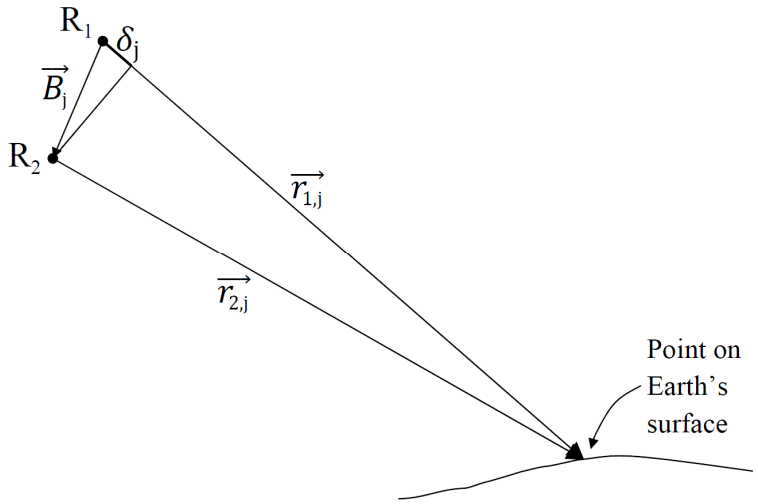

Fig. 2.2 SAR interferometry geometry.

In the far field, δ_j is approximated by the projection of the baseline vector $\overrightarrow{B_j}$ on the look vector $\overrightarrow{r_{1,j}}$ (see (Rosen et al., 2000) and Fig. 2.2)

$$\delta_j = \left\|\overrightarrow{r_{2,j}}\right\| - \left\|\overrightarrow{r_{1,j}}\right\| \cong -\frac{\overrightarrow{r_{1,j}} \cdot \overrightarrow{B_j}}{\left\|\overrightarrow{r_{1,j}}\right\|} \tag{2.13}$$

The baseline vector $\overrightarrow{B_j}$ is calculated for pixel j as the position difference between the linearized tracks calculated in the motion compensation step at the corresponding azimuth time. As these positions correspond to the mid-point between the transmitting and receiving antennas, the computed baseline must be multiplied by 2. With the help of at least one tie point and by combining (2.12) and (2.13), φ_{const} can be determined.

The range vector corresponding to each position in the interferogram is calculated next. We choose an orthonormal basis with one of the basis vectors being the normalized linearized velocity $\overrightarrow{e_v}$. The velocity vector and a vector linking the sensor to the Earth center are used to derive the cross-track vector $\overrightarrow{e_c}$ through a cross-product; the normal vector $\overrightarrow{e_n}$ is then computed between the two unit vectors to complete the orthonormal basis $\{\overrightarrow{e_v}, \overrightarrow{e_c}, \overrightarrow{e_n}\}$. Expressing $\overrightarrow{r_{1,j}}$ and $\overrightarrow{B_j}$ in this coordinate system (2.14) allows the approximations made in (2.15) and (2.16).

$$\overrightarrow{r_{1,j}} = \begin{pmatrix} r_{1v,j} \\ r_{1c,j} \\ r_{1n,j} \end{pmatrix}, \overrightarrow{B_j} = \begin{pmatrix} B_{v,j} \\ B_{c,j} \\ B_{n,j} \end{pmatrix} \tag{2.14}$$

$$\left\|\overrightarrow{r_{1,j}}\right\| = \sqrt{r_{1v,j}^2 + r_{1c,j}^2 + r_{1n,j}^2} \cong \sqrt{r_{1c,j}^2 + r_{1n,j}^2} \tag{2.15}$$

$$\delta_j \cong -\frac{\overrightarrow{r_{1,j}} \cdot \overrightarrow{B_j}}{\left\|\overrightarrow{r_{1,j}}\right\|} = -\frac{r_{1v,j}B_{v,j} + r_{1c,j}B_{c,j} + r_{1n,j}B_{n,j}}{\left\|\overrightarrow{r_{1,j}}\right\|} \cong -\frac{r_{1c,j}B_{c,j} + r_{1n,j}B_{n,j}}{\left\|\overrightarrow{r_{1,j}}\right\|} \tag{2.16}$$

Equations (2.12), (2.15) and (2.16) can then be rewritten as follows:

$$\delta_j = \frac{\lambda}{2p\pi}\left(\varphi_j + \varphi_{const}\right) \tag{2.17}$$

$$r_{1c,j}^2 + r_{1n,j}^2 - \left\|\overrightarrow{r_{1,j}}\right\|^2 = 0 \tag{2.18}$$

$$r_{1c,\mathrm{j}} = \frac{-\delta_{\mathrm{j}} \left\| \overrightarrow{r_{1,\mathrm{j}}} \right\| - r_{1n,\mathrm{j}} B_{n,\mathrm{j}}}{B_{c,\mathrm{j}}} \tag{2.19}$$

Combining the equations above, we solve a second-degree polynomial to retrieve $r_{1n,\mathrm{j}}$ and $r_{1c,\mathrm{j}}$. Only one solution fulfills the condition of $r_{1n,\mathrm{j}}$ being below the sensor in the interval $\left[0, \left\| \overrightarrow{r_{1,\mathrm{j}}} \right\| \right]$ and $r_{1c,\mathrm{j}}$ being on the correct side (MEMPHIS is left-looking). $r_{1v,\mathrm{j}}$ is set to 0 due to the zero-Doppler geometry. The range vectors $\overrightarrow{r_{1,\mathrm{j}}}$ are transformed back into global Cartesian coordinates and added to the sensor position at their given azimuth time.

A regridding is subsequently applied to regularize the sample intervals in local map coordinates using a convolutional gridding technique:

1) We first build a regular grid in the local map coordinates system.
2) For each position, we weight the contribution of the neighboring height measurements through a Gaussian function multiplied by the measurement coherence value.
3) We add all the weighted contributions and divide them by the weighting sum.
4) If the weighting sum is below a chosen threshold value, a null cell value replaces the result.

2.4 Results

We focus on the Ka-band data from two test sites: 1) Feldberg in the Black Forest, Baden-Württemberg, Germany; and 2) Memmingen, Bavaria, Germany. Feldberg is a 1493-m high mountain with a ridge ~3 km long. The test site Memmingen was close to the airport in a mostly flat area. Trihedral corner reflectors were placed at the test sites (four at Memmingen and five at Feldberg) and their positions measured with DGPS. They could be illuminated from four directions and were visible from almost all directions. Four datasets (F1–F4) were acquired at Feldberg and six (M1–M6) at Memmingen. The acquisitions were achieved under rather calm weather conditions, with squint angles ranging from $-1.7°$ to 3.5°. Nevertheless, two acquisitions were troubled by large and rapid Doppler centroid variations. They had to be processed using a variable Doppler centroid, which was implemented using a block processing along azimuth.

We first analyze the data focusing quality and geometric accuracy, followed by a description of a depression angle-dependent correction to the interferometric phase. We characterize the effect of the interferometric phase noise using flat grassland areas, where ALS measurements were available. Finally the InSAR surface model is compared against ALS-based digital terrain models (DTM).

2.4.1 Results of the focusing and geometric accuracy

The raw data were focused as described in Section 2.3.1. The DEMs used for the motion compensation in both Feldberg and Memmingen were coarse DTMs with 100-m resolution. For all accuracy investigations, the entire focused datasets were used. An example from each test site is shown in Fig. 2.3. The signature of each reflector was analyzed for each receiving antenna, i.e., four times for each data take. The analysis was realized on oversampled data, generated with the following method.

1) Spectrum shift in azimuth direction to the Doppler centroid frequency.
2) Oversampling through FFT interpolation (zero-padding the spectrum in both range and azimuth directions).
3) Shifting back of the spectrum.

Fig. 2.3 Examples of MEMPHIS Ka-band SAR images. (a) Acquisition M1 at Memmingen, Germany. (b) Acquisition F3 at Feldberg, Germany. Azimuth and slant range extent of both acquisitions: 2.1×0.6 km.

The resolution was calculated on the oversampled amplitude data of the reflector signature by computing the width of the main lobe 3 dB below its peak. On each side of the main lobe, a linear interpolation between the two values over and below the -3 dB mark was used to improve the reliability of this measurement. For the measurement of the peak sidelobe ratio (PSLR), we considered sidelobes within a $[20\rho_r, 20\rho_a]$ rectangle, excluding a main lobe rectangle of $[2\rho_r, 3\rho_a]$ with ρ_r and ρ_a the measured range and azimuth resolutions respectively (Vu et al., 2008). The results are summarized in Table 2.3 for Memmingen and Table 2.4 for Feldberg. Fig. 2.4 and Fig. 2.5 show the measured versus expected positions of the analyzed reflector signatures.

TABLE 2.3
SUMMARY OF THE POINT TARGET ANALYSIS
ON ALL CORNER REFLECTORS AT MEMMINGEN

	Average	Standard deviation
Range resolution [cm]	16.90	0.38
Azimuth resolution [cm]	9.29	0.21
Range PSLR [dB]	-15.94	1.06
Azimuth PSLR [dB]	-25.02	1.80
Range position error [cm]	0.16	3.25
Azimuth position error [cm]	1.72	3.59

Statistic based on 32 measurements.

TABLE 2.4
SUMMARY OF THE POINT TARGET ANALYSIS
ON ALL CORNER REFLECTORS AT FELDBERG

	Average	Standard deviation
Range resolution [cm]	16.91	0.35
Azimuth resolution [cm]	9.66	0.54
Range PSLR [dB]	-14.86	1.78
Azimuth PSLR [dB]	-25.05	2.47
Range position error [cm]	0.79	4.37
Azimuth position error [cm]	3.83	18.58

Statistic based on 52 measurements.

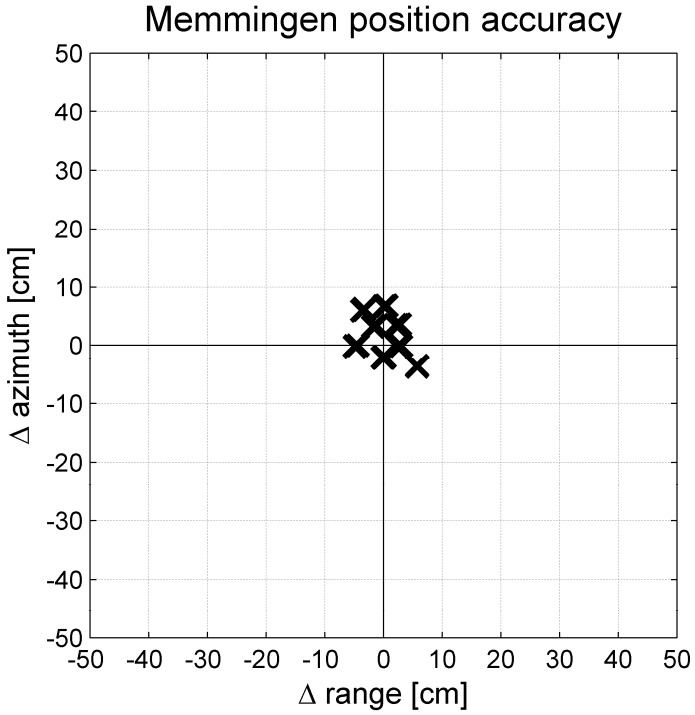

Fig. 2.4 Location errors between the measured and expected positions of the corner reflector signatures at Memmingen.

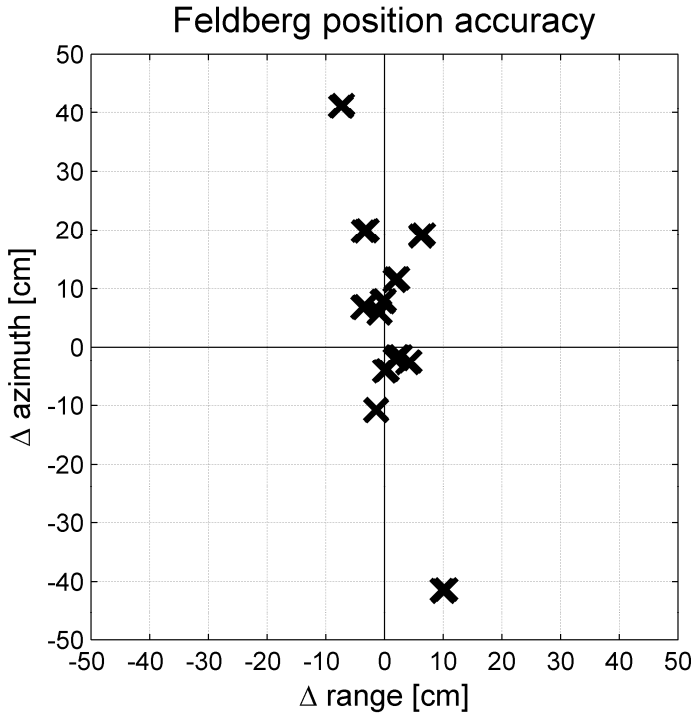

Fig. 2.5 Location errors between the measured and expected positions of the corner reflector signatures at Feldberg.

The experimental -3 dB resolution is close to the theoretical value in both the range (2.20) and azimuth (2.21) directions

$$R_r = \frac{c}{2B_w} = 0.1665 \text{ [m]} \tag{2.20}$$

where c is the speed of light and B_w is the radar bandwidth

$$R_a \cong \frac{\lambda}{2\theta_a} \cong 0.082 \text{ [m]} \tag{2.21}$$

where λ is the wavelength and θ_a is the radar azimuth beam width.

The tie point-free geolocation accuracy lies in the same order of magnitude as the resolution, meeting the expectations given MEMPHIS experimental and portable design. This is possible due to the high quality of the DGPS and INS data, the lever arm measurements, the accurate sampling window start time, the estimation of the speed of light in the air, the Extended Omega-K algorithm and the motion compensation steps.

Nevertheless, the data quality occasionally suffered from intense range sidelobes close to bright targets (extending twice the chirp length) as seen at the bottom-right of Fig. 2.3(a); their origin is not yet precisely known.

2.4.2 Correction of depression angle-dependent phase errors

First results of the interferometric processing showed error patterns in the range direction similar for each dataset. Their analysis showed a depression angle dependency. These might have been corrected using antenna phase patterns, but no such measurements were made on MEMPHIS antennas.

Fig. 2.6 Geocoded SAR images at Memmingen whose interferometric data were used for the depression angle-dependent phase correction. The flight directions were 60° (both north and south of the runway), 150°, 240° (both north and south of the runway), and 330°. Aerial imagery © Bayerische Vermessungsverwaltung 2009.

Therefore, we used the data themselves to correct these errors as follows: six acquisitions were made over Memmingen at four different headings (with 90° angle between them), with overlapping illuminated areas as shown in Fig. 2.6. We analyzed the calculated height of the overlapping regions to build a depression angle-dependent phase correction function. The intersecting regions were compared using two independent acquisitions acquired at a 90° crossing angle. Thus the range height behavior, containing the depression angle-dependent errors of one *test* acquisition was compared to the azimuth height behavior (less susceptible to correlated error trends) of a second *reference* acquisition.

For each pair of acquisitions, a depression angle-dependent phase correction curve was calculated as follows:

1) The map coordinates and height of each pixel of the *test* interferogram were calculated (without regridding).
2) The same process as in the previous step was carried out with the *reference* interferogram, including a regridding to build a *reference* DEM.
3) For each range line of the *test* acquisition, the corresponding height of the *reference* DEM was subtracted; the mean height difference was subsequently subtracted to remove any constant error.
4) The depression angle was calculated for each pixel of the *test* acquisition. The height differences h_{diff} were transformed into phase correction values using the local ambiguity heights with: $\varphi_{\mathrm{corr}} = -h_{\mathrm{diff}} \cdot \frac{2\pi}{h_{2\pi}}$.
5) The phase correction values were aggregated onto a regular depression angle vector through a convolutional gridding similar to the one described at the end of Section 2.3.2.3.

In total, this led to 16 curves; the mean was computed at each depression angle step. Finally, a low-pass filter was applied to the mean curve. This curve was validated by comparing it to a similar one generated using an ALS surface model as reference rather than the crossing SAR data takes (see Fig. 2.7). This method would work even better using a featureless test area, as Memmingen buildings and forests can hinder the comparison between perpendicular acquisitions.

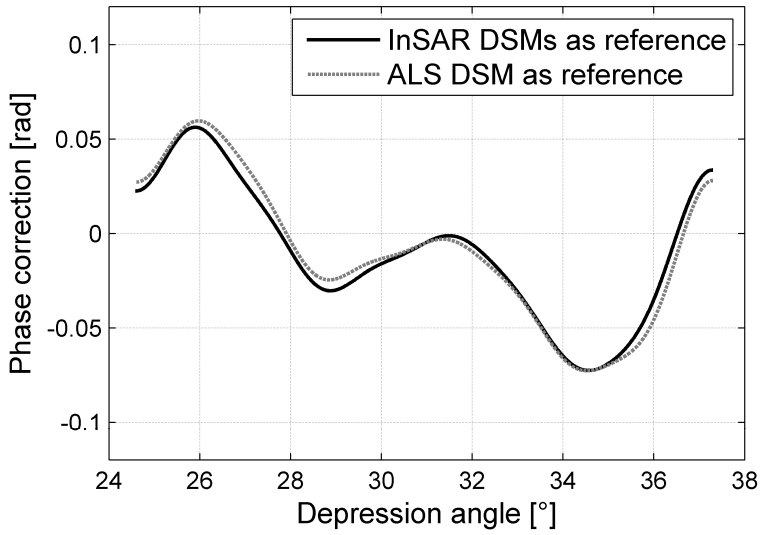

Fig. 2.7 Computed depression angle-dependent phase correction to apply on the interferometric data (largest baseline). Mean phase correction computed through the analysis of the crossing InSAR acquisitions compared to values resulting from use of the ALS DSM as reference.

TABLE 2.5
NUMBER OF LOOKS TESTED IN THE INTERFEROMETRIC PROCESSING

Range looks	Azimuth looks	Range pixel spacing [m]	Azimuth pixel spacing [m]
1	4	0.167	0.207
2	8	0.333	0.414
3	12	0.500	0.621
4	16	0.666	0.828
5	20	0.833	1.035
6	24	0.999	1.242
10	40	1.665	2.070

The azimuth pixel spacing corresponds to the average over the 6 tested datasets at Memmingen.

2.4.3 Interferometric phase noise

The effect of the interferometric phase noise was characterized using flat reference surfaces at Memmingen (i.e., as flat as available). ALS data of these surfaces were first analyzed for providing a comparison base to the InSAR data. We used six datasets, their test surfaces ranging from near to far range. Each analyzed surface was approximately the size of a football field (~75 × 60 m).

Interferograms from these six data takes were processed with the multilooking factors shown in Table 2.5. Three products were built from the result of the multibaseline phase unwrapping: one unfiltered, the others after applying 3×3 and 5×5 median filters. The standard deviation from the mean derived altitude was then analyzed. The results are shown in Fig. 2.8.

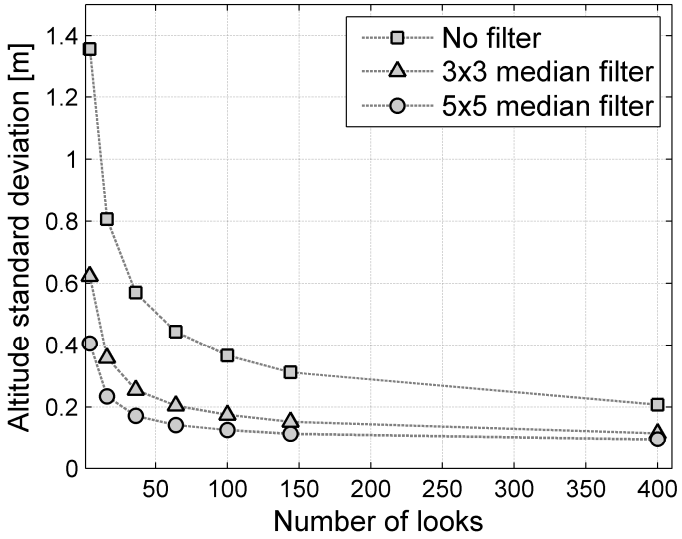

Fig. 2.8 Analysis of interferometric phase noise: a 60×75 m flat area was selected on six different data acquisitions from Memmingen. The standard deviation around the mean altitude of the reconstructed height for the various processing methods is shown in the plot, averaged over the six datasets. The equivalent mean standard deviation of the reference ALS model was 0.072 m.

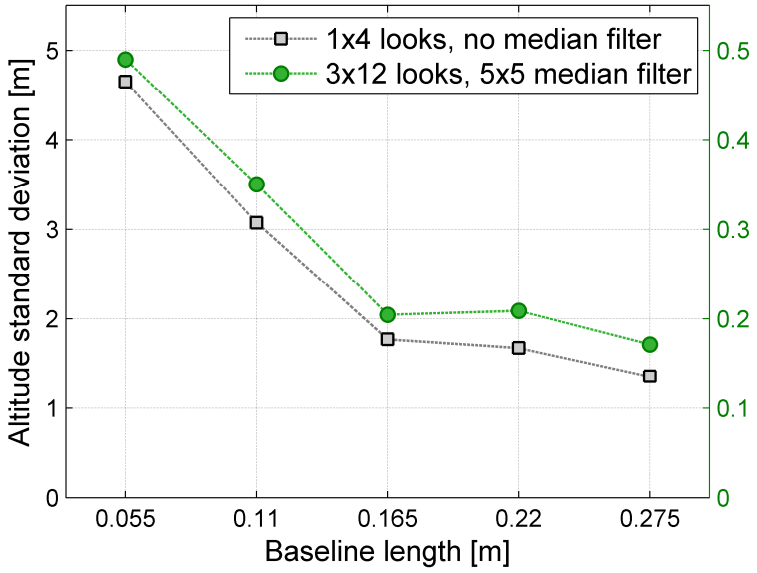

Fig. 2.9 Analysis of interferometric phase noise depending on the baseline length. The same areas as reported in Fig. 2.8 were used. Two sets of processing parameters were used: 1×4 looks and no median filter (standard deviation scale on the left) as well as the operational parameters using 3×12 looks and a 5×5 median filter (standard deviation scale on the right).

The median filter provides about the same noise reduction as an average filter of similar size, but does a better job at preserving edges (Arce, 2005). From this analysis, 3 looks in range and 12 looks in azimuth were used followed by a 5×5 median filter before generation of the digital surface model.

The effect of the baseline length was also analyzed using the same flat reference surfaces. Two cases were investigated: 1) using 1 look in range and 4 looks in azimuth without a filter, and 2) using 3 looks in range and 12 looks in azimuth with a 5×5 median filter, i.e., the operational setup. Fig. 2.9 summarizes the results.

TABLE 2.6
COMPARISON BETWEEN ALS MODELS HEIGHT AND DGPS MEASUREMENTS

	Memmingen	Feldberg
Mean [cm]	6.07	5.10
Standard deviation [cm]	8.22	8.35
Mean absolute difference [cm]	6.10	8.21

Statistics of the difference between ALS model height and DGPS measurements ($H_{ALS} - H_{DGPS}$). 8 DGPS measurements at Memmingen and 7 at Feldberg were used.

2.4.4 Digital surface model

The generated InSAR digital surface models from Memmingen and Feldberg area were analyzed to assess the system and algorithm accuracies, with focus on the grassland areas. For this we compared the InSAR DSMs to reference ALS terrain models. A comparison with ALS surface models would introduce further issues complicating the accuracy assessment: the forest/tree height retrieved with both techniques is not directly comparable due to different acquisition years and seasons and different vegetation penetration properties. Different inherent sensor properties, especially along steep edges of buildings and trees, would also introduce validation errors.

Using the height difference between the InSAR DSMs and the ALS terrain models we were able to filter out the higher vegetation and built areas from the InSAR DSMs, without the need of precise GIS data. The data were filtered using min/max threshold values. The threshold values were calculated iteratively using a $\pm 3\,\sigma$ window centered at the mean position. In each iteration, the values outside the window were discarded and a new window was calculated until the threshold values converged.

The expected accuracy of the ALS models was better than 10 cm for the flat areas (Joerg et al., 2012), with larger errors possible on slopes, depending on the illumination direction, flight altitude, point density, DTM reconstruction method, surface roughness, and penetration through vegetation. The ALS data were acquired in November 2003 and April 2004 at Feldberg and in February 2007 at Memmingen: some areas therefore saw changes, and some fields with grown vegetation in one source were compared with their respective bare soil height in the other. Combined campaigns with ALS and InSAR measurements would be needed for an improved intercomparison. The accuracy of the used ALS models was controlled using the small set of DGPS measurements we surveyed for the InSAR campaign (see Table 2.6).

Examples are shown in a series of figures. Fig. 2.10 shows the generated DSM from the acquisition M1 over the Memmingen airport, Fig. 2.11 shows its difference with a reference ALS DTM, and Fig. 2.12 shows the result after the filter for vegetation and buildings was applied. We clearly see that a substantial part of the height difference is caused by the different vegetation heights. The DSM produced from the dataset F3 over Feldberg and its difference with an ALS terrain model are presented in Fig. 2.13. The depression angle-dependent phase errors could only be partially corrected; due to the topography, we have much steeper depression angles at near range than over Memmingen, going up to 42°, which could not be remedied with the correction function.

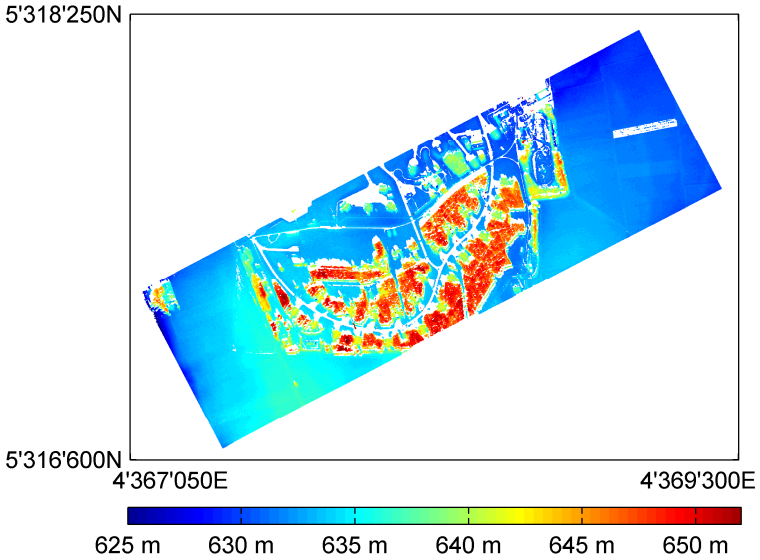

Fig. 2.10 DSM obtained from the acquisition at Memmingen shown in Fig. 2.3. White areas in the middle of the strip are areas in shadow or with low coherence. Coordinate system: German Gauss-Krüger strip 4, elevation over DHHN92 (*Deutsches Haupthöhennetz 1992* – German mean height reference system 1992) reference.

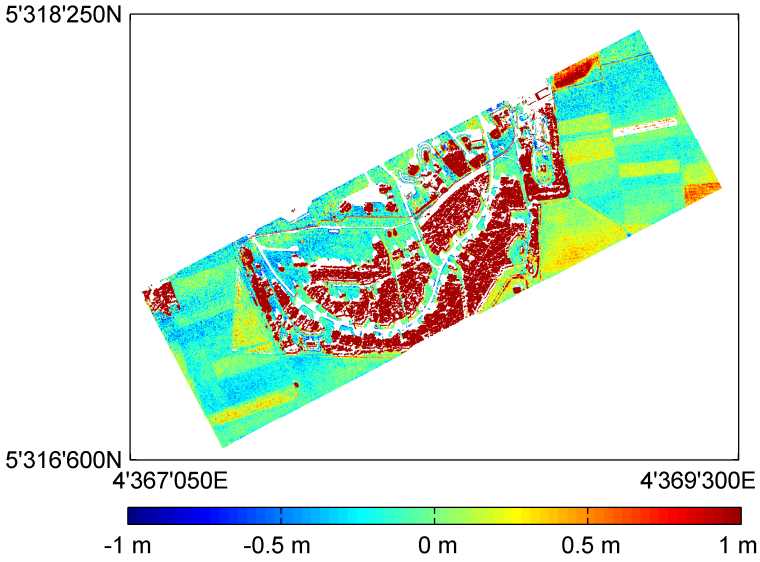

Fig. 2.11 Difference between the DSM shown in Fig. 2.10 and the reference ALS terrain model.

Table 2.7 and Table 2.8 summarize the results obtained for all acquisitions at Memmingen and Feldberg. Eight of the ten generated DSMs showed low systematic offsets when compared to the ALS models of −0.103 to 0.086 m, and a standard deviation ranging from 0.193 m to 0.342 m. Two acquisitions (F1 and F4) showed larger systematic offsets of −0.108 and 0.164 m and larger standard deviations of 0.597 and 0.571 m. These acquisitions were particularly difficult to focus, due to very rapidly changing Doppler centroid values; their processing required a block processing method with a variable Doppler centroid. Nevertheless, some ghosts remained in parts of acquisition F1, certainly also influencing the phase. They also contained larger deviations (up to 5 m) from the linearized track than the others. As not all histograms follow a normal distribution, Table 2.7 and Table 2.8 list the mean absolute height difference.

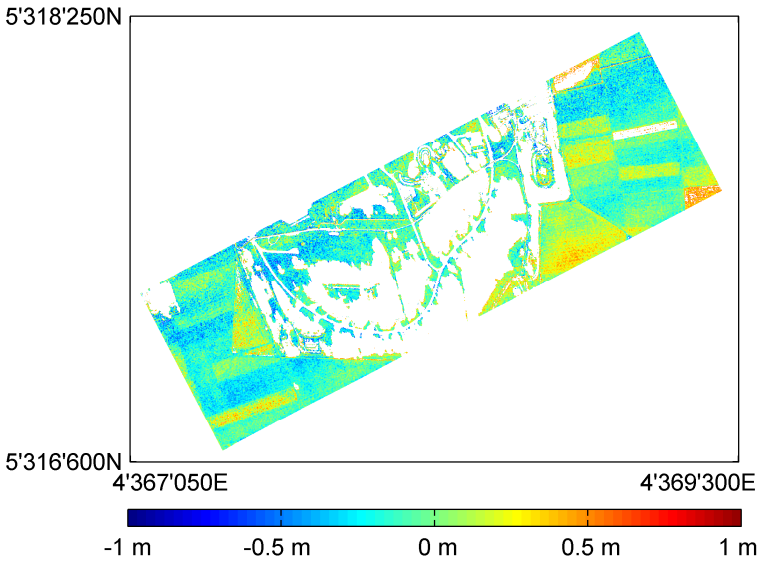

Fig. 2.12 Difference between the DSM shown in Fig. 2.10 and the reference ALS terrain model after filtering out the vegetation and buildings.

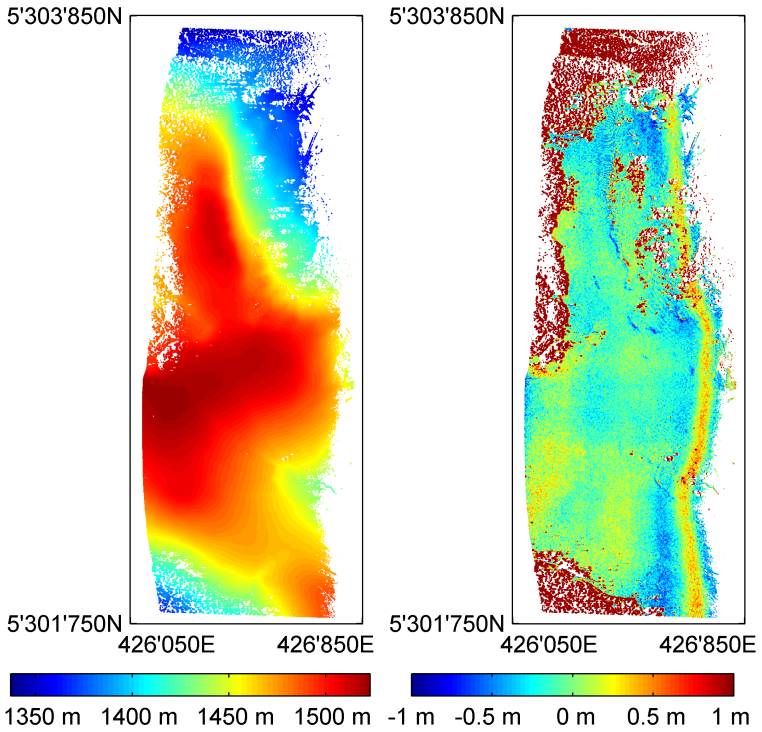

Fig. 2.13 On the left side, DSM obtained from the acquisition at Feldberg shown in Fig. 2.3. On the right side, difference between the DSM and the reference ALS terrain model. Coordinate system: UTM32, elevation over UTM ellipsoid.

TABLE 2.7
RESULTS OF INSAR DSM GENERATION AT MEMMINGEN

Characteristics	Histogram ($h_{InSAR} - h_{ALS}$)
Track: M1 Covered area: 1.170 km^2 Min ground elevation: 622.83 m Max ground elevation: 641.82 m Mean height difference: -0.060 m Standard deviation: 0.222 m Mean absolute difference: 0.184 m	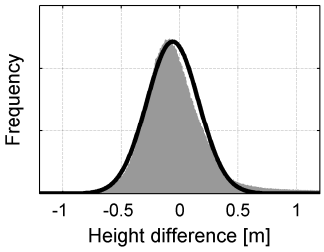
Track: M2 Covered area: 1.281 km^2 Min ground elevation: 603.36 m Max ground elevation: 641.76 m Mean height difference: 0.086 m Standard deviation: 0.342 m Mean absolute difference: 0.284 m	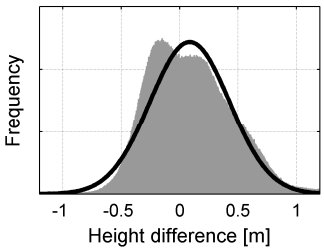
Track: M3 Covered area: 1.145 km^2 Min ground elevation: 624.96 m Max ground elevation: 641.30 m Mean height difference: 0.049 m Standard deviation: 0.193 m Mean absolute difference: 0.155 m	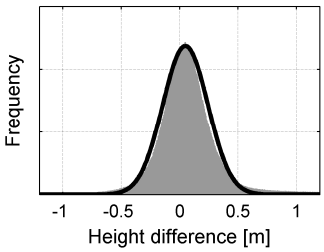
Track: M4 Covered area: 1.069 km^2 Min ground elevation: 624.96 m Max ground elevation: 641.83 m Mean height difference: 0.049 m Standard deviation: 0.224 m Mean absolute difference: 0.178 m	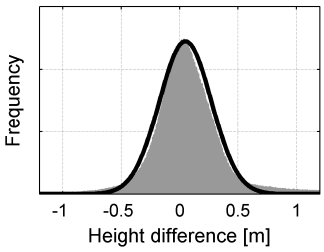
Track: M5 Covered area: 1.157 km^2 Min ground elevation: 608.98 m Max ground elevation: 634.90 m Mean height difference: -0.079 m Standard deviation: 0.283 m Mean absolute difference: 0.229 m	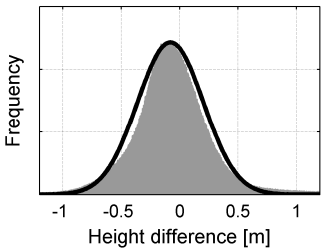
Track: M6 Covered area: 1.044 km^2 Min ground elevation: 602.80 m Max ground elevation: 634.91 m Mean height difference: -0.103 m Standard deviation: 0.225 m Mean absolute difference: 0.196 m	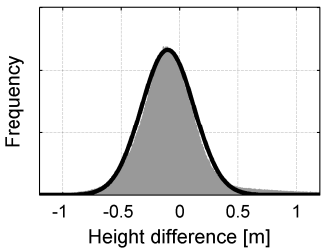

The ground elevations were calculated from the ALS ground model (over DHHN92 reference).

TABLE 2.8
RESULTS OF INSAR DSM GENERATION AT FELDBERG

Characteristics	Histogram ($h_{InSAR} - h_{ALS}$)
Track: F1 (var. Doppler centroid necessary) Covered area: 1.648 km^2 Min ground elevation: 1351.10 m Max ground elevation: 1544.48 m Mean height difference: -0.108 m Standard deviation: 0.597 m Mean absolute difference: 0.497 m	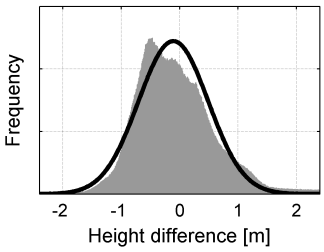
Track: F2 Covered area: 1.821 km^2 Min ground elevation: 1093.87 m Max ground elevation: 1544.46 m Mean height difference: 0.076 m Standard deviation: 0.265 m Mean absolute difference: 0.216 m	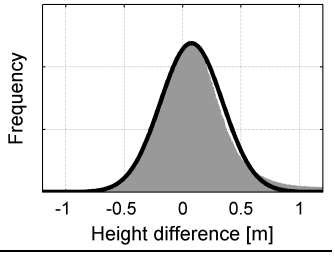
Track: F3 Covered area: 1.064 km^2 Min ground elevation: 1320.79 m Max ground elevation: 1522.74 m Mean height difference: -0.059 m Standard deviation: 0.228 m Mean absolute difference: 0.186 m	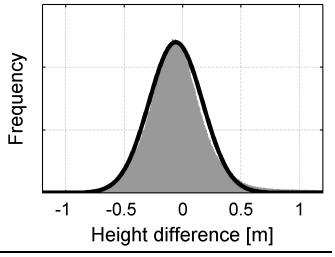
Track: F4 (var. Doppler centroid necessary) Covered area: 1.056 km^2 Min ground elevation: 1274.70 m Max ground elevation: 1519.38 m Mean height difference: 0.164 m Standard deviation: 0.571 m Mean absolute difference: 0.499 m	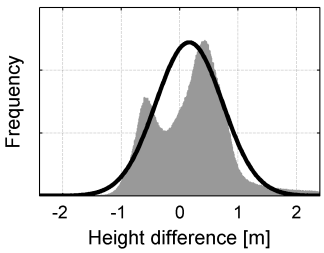

The ground elevations were calculated from the ALS ground model (over UTM ellipsoid)

2.5 Discussion

In the following, we discuss possible error sources, highlight the quality of the achieved results and conclude with an outlook to potential future improvements.

2.5.1 Error analysis

Several possible error sources were identified in the following categories: the antenna phase center positions, non-ideal motion compensation, the phase to height conversion model, and the coregistration of the SAR data from each antenna. This section describes the source of these errors and an estimation of their size, when possible.

2.5.1.1 Antennas phase center position

Errors in the relative position of the antennas phase centers can lead to errors in the reconstructed height. The antenna horns were machined separately using a CNC milling machine and assembled next as a rigid block. The baseline lengths were therefore physically constant. The accuracy of a CNC milling machine ranges from better than 10 µm up to ~100 µm (Raksiri &

Parnichkun, 2004), depending on the machine, type of error, and applied corrections. We assume possible horn shape errors at the lower end of the error interval and baseline length errors at its higher end. The antennas were manually tilted in operating position, with a maximal estimated error of 2°. The attitude measurements and in particular the roll angles have an absolute accuracy better than 0.005° when combined with DGPS data (iMAR, 2010).

The machining errors (and/or some non-ideal electromagnetic behavior) might induce variations in the position of the phase centers along the illumination direction, depending on the antenna beam elevation. A Δx = 10 µm relative displacement in the illumination direction at mid-range would correspond to $\frac{\Delta x}{\lambda} \cdot h_{2\pi} \cong 0.05$ m height error.

TABLE 2.9
MEMPHIS PARAMETERS USED FOR THE ERROR ANALYSIS

Baseline [m]	0.275		
Baseline tilt angle [°]	30		
Altitude a.g.l. [m]	770		
	Near range	Mid range	Far range
Slant range [m]	1249	1547	1845
Depression angle [°]	51.94	60.15	65.33
Ambiguity height [m]	30.85	41.68	52.31

Errors related to an inaccurate measurement of the baseline or to a wrongly tilted antenna are partially compensated by using a tie point to calculate φ_{const}. An estimation of the possible error can be obtained by assuming a flat surface and an accurate mid-range reconstructed height thanks to the use of a tie point, then computing a real world δ_{j} at extreme near and far range and conducting a comparison with and without an included error. δ_{j} can be calculated as $\delta_{\text{j}} = B \cdot \sin(\theta_{\text{j}} - \alpha)$ with θ_{j} the off-nadir angle at sample j. The values based on the measurements over Memmingen airport shown in Table 2.9 were used for the error estimation. This analysis does not treat motion compensation issues.

1) An error of 100 µm in the baseline length would result in a height error of $\frac{\delta_{\text{j, error}} - \delta_{\text{j}}}{\lambda} \cdot h_{2\pi}$, specifically, 0.051 m at near range and -0.057 m at far range.
2) Alternatively, we can compute the maximum baseline error permissible to keep the height error lower than 0.5 m along the whole range swath. The baseline error would have to be less than 880 µm.
3) A wrongly tilted antenna would also lead to height errors at near and far range. The error can be computed as $\frac{(\delta_{\text{j, error}} - \delta_{\text{j}}) - (\delta_{\text{mid range, error}} - \delta_{\text{mid range}})}{\lambda} \cdot h_{2\pi}$. Here, the worst case scenario is a 2° error, which results in a maximum error at near range of -0.43 m. With an antenna wrongly tilted in the other direction, the corresponding error becomes 0.26 m at near range and 0.35 m at far range.

Fig. 2.14 shows estimated and measured height differences obtained using a wrong baseline length (0.27588 m instead of 0.275 m), and wrongly tilted antennas ($+2°$ and $-2°$ error relative to the nominal angle). The estimated and measured curves are very similar, their differences may come from the topography and Earth curvature in the real acquisition, leading to slightly different depression angles.

In summary, the critical issues are the similarity of the antenna horn shapes, their electromagnetic behavior, and the accuracy of the antenna tilting. The accuracy of the measurement of the baseline *length* is a lesser concern.

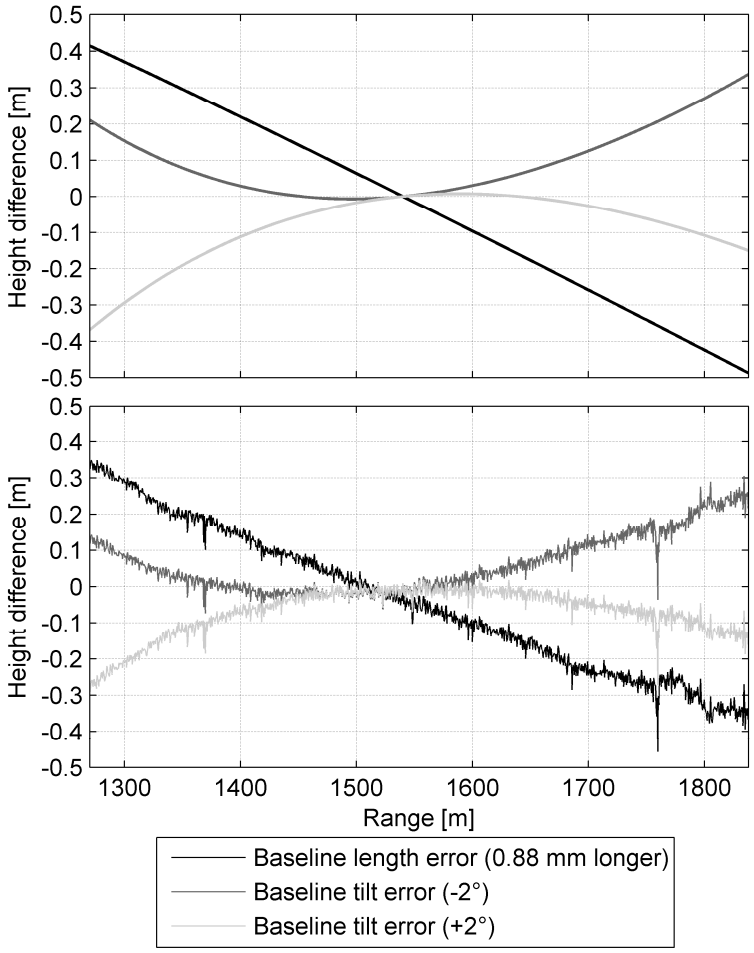

Fig. 2.14 Height difference caused by an erroneous baseline. The top chart contains the estimated error. The bottom chart shows the height difference for a real acquisition (M1). The height difference between the result obtained with the erroneous baseline and the original result is calculated pixel-wise and then averaged along the azimuth direction.

2.5.1.2 Motion compensation

The motion compensation achieves a correction in range corresponding to a determined height, which may differ from the real one. Two different heights imply different range vectors; the projection (used in the motion compensation) of the vector linking the real and linearized tracks onto both range vectors results in two different lengths, their difference leads to a positioning as well as a height error on the generated DSM.

This error can be approximated as

$$\begin{aligned}\Delta r_{\mathrm{j,\,ground\,range}} &\cong \left[d_{\mathrm{j},\perp}\cdot\sin\left(\theta_{\mathrm{j,\,real}}-\theta_{\mathrm{j,\,moco}}\right)-d_{\mathrm{j},\parallel}\right.\\ &\quad\left.\cdot\left(1-\cos\left(\theta_{\mathrm{j,\,real}}-\theta_{\mathrm{j,\,moco}}\right)\right)\right]\cdot\sin\theta_{\mathrm{j,\,real}}\\ \Delta r_{\mathrm{j,\,height}} &\cong \left[d_{\mathrm{j},\perp}\cdot\sin\left(\theta_{\mathrm{j,\,real}}-\theta_{\mathrm{j,\,moco}}\right)-d_{\mathrm{j},\parallel}\right.\\ &\quad\left.\cdot\left(1-\cos\left(\theta_{\mathrm{j,\,real}}-\theta_{\mathrm{j,\,moco}}\right)\right)\right]\cdot\cos\theta_{\mathrm{j,\,real}}\end{aligned} \tag{2.22}$$

where $\Delta r_{\mathrm{j,\,ground\,range}}$ is the positioning error in the ground range direction, $\Delta r_{\mathrm{j,\,height}}$ is the height error, $d_{\mathrm{j},\perp}$ and $d_{\mathrm{j},\parallel}=\Delta r_{\mathrm{j}}$ are the position difference between the real and linearized positions, perpendicular and parallel to the line of sight used in the motion compensation, respectively.

$\theta_{\mathrm{j,\,real}}$ is the real off-nadir angle and $\theta_{\mathrm{j,\,moco}}$ is the off-nadir angle used in the motion compensation.

In the processed data, we observed deviations between the real and linearized track usually below 2 m with worst cases up to 5 m. Using the parameters from Table 2.9, with a DEM height error of 30 m (corresponding to a tree or building) and a worst observed case $d_{\mathrm{j},\perp} = 5$ m ($d_{\mathrm{j},\parallel}$ has a very low impact), at mid-range errors of $\Delta r_{\mathrm{j,\,ground\ range}} \cong 0.098$ m and $\Delta r_{\mathrm{j,\,height}} \cong 0.053$ m result.

2.5.1.3 Phase to height conversion model

The phase to height conversion model uses an approximated baseline calculated as the position difference between the linearized tracks. This approximation delivers exact results only given perfect motion compensation, i.e., when the height used for the motion compensation is accurate and/or with a real baseline vector matching the approximated baseline vector. Since MEMPHIS is a single-pass interferometric system, the only important parameter affecting the baseline vector is the airplane real attitude compared to the linearized attitude, i.e., mainly the roll angle difference. The error introduced through the used model and the approximated baseline thus mainly depends on the roll angle difference between the real and linearized tracks, the baseline length, and the difference between the real depression angle and the one used in the motion compensation.

This error can be approximated with the expression

$$\frac{\sqrt{2 \cdot B^2(1-\cos\Delta\alpha_{\mathrm{roll}})} \cdot \left[\cos(\theta_{\mathrm{j,\,real}} - \alpha) - \cos(\theta_{\mathrm{j,\,moco}} - \alpha)\right]}{\lambda} \cdot h_{2\pi} \tag{2.23}$$

where $\Delta\alpha_{\mathrm{roll}}$ is the angular difference between the real roll angle and the one calculated from the linearized tracks. In the processed data, we observed $\Delta\alpha_{\mathrm{roll}}$ values up to 2°. Again, using the values from Table 2.9, this roll error combined with a 30-m DEM error leads to height inaccuracies ranging from 0.13 m at near range to -0.11 m at far range.

2.5.1.4 Coregistration

No coregistration step was implemented. The expected misregistration error can nonetheless be theoretically computed using the values in Table 2.9 for a flat surface. We get a theoretical maximal misregistration of $\frac{\delta_{\mathrm{j}}}{2} = 0.0193$ m at near range (the factor 2 is due to MEMPHIS being a common-transmitter system). Different delays may also occur within each of the receiving feeds. We analyzed the position difference of the reflector signatures in the channels effectively used for the final DSM reconstruction (from the receiving horns forming the 0.275 m baseline). The results are shown in Table 2.10. The largest observed misregistrations were 0.021 m and 0.013 m in range and azimuth respectively, respectively ~1/24 and ~1/46 of the cell sizes used in the DSM reconstruction (considering the 3 looks in range and 12 looks in azimuth, see Table 2.5). Both the calculated and measured misregistrations were low enough to ensure a very limited decorrelation.

Interferometric processing of squinted SAR data was investigated in (Bara et al., 2000). The interferometric phase may become biased in the presence of squint, mainly due to the range spectrum shift caused collaterally by azimuth focusing. Then, even very small misregistrations between the SAR images can cause large height errors. To reduce these possible phase errors, the spectrum shift caused by the azimuth focusing was compensated using expression (2.7). The low squints observed in the presented campaigns and the low relative misregistration should effectively restrict the sensitivity to these errors.

TABLE 2.10
MEASURED MISREGISTRATION OF CORNER REFLECTORS

	Range	Azimuth
Mean [m]	-0.0088	-0.0054
Standard deviation [m]	0.0062	0.0037
Min observed value [m]	-0.0210	-0.0134
Max observed values [m]	0.0009	0.0004

The misregistration was computed between the signatures of the reflectors on pairs of images corresponding to the longest baseline.

2.5.2 Conclusion

We described a processing chain starting from MEMPHIS SAR raw data up to the generation of DSMs. We reviewed the Extended Omega-K algorithm, showed a way to use MEMPHIS multibaseline data to simplify phase unwrapping, and proposed an adaptation to a phase-to-height algorithm. The results of an acquisition campaign with 10 data takes were investigated.

The signatures of corner reflectors were analyzed; the measured resolution was ~0.17 m in range and ~0.1 m in azimuth, very close to the theoretical resolution of 0.1665 m in range and 0.082 m in azimuth. The geolocation accuracy was compared to DGPS measurements, showing errors typically below 0.1 m in both the range and azimuth directions in Memmingen; in Feldberg they were also typically below 0.1 m in range, and for 3 of the 4 acquisitions below 0.2 m in azimuth.

The first results of the interferometric processing showed the presence of depression angle-dependent phase errors. We were able to derive a correcting function using the crossing pattern of data takes acquired over Memmingen. The resulting function successfully removed the error trends in the Memmingen data. At Feldberg, the data at near range were acquired with steeper depression angles than at Memmingen. Therefore, it was not possible to fully correct these data with the correction function derived from the Memmingen data takes and some phase errors remained. A combination of the errors studied in Section 2.5.1.1 could at least partially explain the source of these depression angle phase errors.

The effects of the interferometric phase noise were analyzed using a set of multilook factors and median filter sizes on flat areas. The measured noise ranged from ~1.4 m standard deviation with 1 range look and 4 azimuth looks (0.167 × 0.207 m) *without* a median filter to ~0.1 m with 10 range looks and 40 azimuth looks (1.67 × 2.07 m) *with* a 5×5 median filter.

From the analysis of the phase noise, a configuration with 3 range looks and 12 azimuth looks combined with a 5×5 median filter was chosen. The produced DSMs agreed very well with reference ALS data; for most of the datasets, the results showed a very low systematic difference typically below 0.1 m and a standard deviation of 0.2–0.3 m.

2.5.3 Outlook

Future plans include investigations of the intense range sidelobes by testing different approaches for the range compression (Blunt & Gerlach, 2006) and/or the stepped-frequency bandwidth reconstruction (Schimpf et al., 2003). Possible hardware issues such as a saturation of components will be discussed with the sensor operator.

Coarse resolution DEMs were used in the motion compensation step. An iterative approach could also have been used whereby a DSM is first produced using a flat surface, followed by a refocusing step using the smoothed generated DSM to make a higher quality product. A topography- and aperture-dependent based motion compensation would probably further improve the results (Prats et al., 2007): we would be able to use higher resolution DEMs and thus reduce the errors investigated in Sections 2.5.1.2 and 2.5.1.3.

Phase error trends in azimuth may be due to slightly inaccurate navigation data. Multisquint approaches can be used to correct such errors (Prats & Mallorqui, 2003; Prats et al., 2004), especially when large azimuth beam widths are available. Our data show small error trends in azimuth exclusively over rather large distances. These error trends would be extremely difficult to correct with a multisquint approach, due to the sensor's narrow azimuth beam width. We barely see high frequency errors in the azimuth direction, indicating a high relative accuracy of the navigation data.

A better way to ensure use of the full information of the multibaseline data would be through a maximum likelihood (ML) algorithm, as presented in (Lombardo & Lombardini, 1997; Lombardini & Griffiths, 2001). The approach presented in Section 2.3.2.2 was selected to counteract the depression angle-dependent phase errors that can be different for each antenna combination. A careful calibration of each antenna phase pattern would be needed before applying a ML algorithm.

Several alternative or further steps could be carried out. From the results presented above, one could imagine combining the various illumination directions to reduce the overall error and improve the coverage in shadowed areas. One could also fill the holes using diffusion-based interpolation methods or replace the median filter of the unwrapped interferogram with an adaptive filtering technique.

However additional processing steps should be evaluated carefully, as the accuracy achieved in the generated surface models is already very high.

Acknowledgments

The authors would particularly like to thank C. Ackermann from the TU Munich for lending the INS hardware and for his invaluable technical assistance.

3 ANALYSIS OF A MAXIMUM LIKELIHOOD PHASE ESTIMATION METHOD FOR AIRBORNE MULTI-BASELINE SAR INTERFEROMETRY

This chapter has been published as: Magnard, C., Frioud, M., Small, D., Brehm, T., & Meier, E. (2016). Analysis of a maximum likelihood phase estimation method for airborne multibaseline SAR interferometry. *IEEE Journal of Selected Topics in Applied Earth Observations and Remote Sensing*, *9*(3), 1072-1085.

For clarity, the paper has been reformatted and the references are listed at the end of the thesis; otherwise, the contents are the same as in the journal article.

Contributions of first author and co-authors: CM, EM designed the study. CM, MF, DS developed the methodology. CM, TB collected the data. CM performed the analysis. CM, MF, DS, EM wrote the paper.

Abstract

It has been shown using simulated data that phase estimation of cross-track multibaseline synthetic aperture radar (SAR) interferometric data was most efficiently achieved through a maximum likelihood (ML) method. In this paper, we apply and assess the ML approach on real data, acquired with an experimental Ka-band multibaseline system. Compared to simulated data, dealing with real data implies that several calibration steps be carried out to ensure that the data fit the model. A processing chain was, therefore, designed, including steps responsible for compensating for imperfections observed in the data, such as beam elevation angle dependent phase errors or phase errors caused by imperfect motion compensation. The performance of the ML phase estimation was evaluated by comparing it to results based on a coarse-to-fine algorithm (C2F), where information from the shorter baselines was used only to unwrap the phase from the longest available baseline. For this purpose, flat areas with high coherence and homogeneous texture were selected in the acquired data. The results show that with only four looks, the noise level was marginally better with the C2F approach and contained fewer outliers. However, with more looks, the ML method consistently delivered better results: noise variance with the C2F approach was slightly but steadily larger than the variance obtained with ML method.

3.1 Introduction

Cross-track synthetic aperture radar (SAR) interferometry (InSAR) typically uses two receiving antennas forming a single baseline (Zebker & Goldstein, 1986). The length of this baseline must be chosen as a tradeoff. Interferograms generated using short baselines are easy to unwrap but have high sensitivity to a constant phase noise level. Interferograms from longer baselines are more difficult to unwrap, but have a lower sensitivity to the noise level (Rosen et al., 2000), i.e., a better height resolution. Multibaseline interferometric SAR systems aim to overcome these limitations by using several baselines of diverse lengths. The data from shorter baselines help unwrap interferograms based on longer baselines, and the lower relative noise level from the longer baselines is maintained in the composite solution.

Numerous methods have been developed for processing multibaseline InSAR data. The coarse-to-fine (C2F) phase unwrapping method (Essen et al., 2007; Magnard et al., 2014) uses data from the shorter baselines to unwrap the interferogram based on the longest baseline. This method keeps the unwrapped phase information from the longest baseline, discarding information from the other baselines. The maximum likelihood (ML) method (Lombardo & Lombardini, 1997) calculates a most-likely phase from arrays of focused SAR data [single look complex (SLC) data] according to a model. This allows use of all the data and should, therefore, improve the noise level and reliability. Several other methods such as least squares or weighted least squares can also be used to calculate the unwrapped phase; they were compared in (Lombardini & Griffiths, 2001), showing their advantages and shortcomings. In (Ferretti et al., 1999), a wavelet-domain weighted average was proposed to generate digital elevation models (DEMs) from multibaseline InSAR data. Multibaseline ML phase estimation was extended to handle multi-aspect data in (Schmitt & Stilla, 2014c). Results from single- and multiple-pass multibaseline InSAR acquisitions with the PAMIR sensor (Brenner & Roessing, 2008) were presented in (Brenner et al., 2010). A single-pass multibaseline tomography concept was demonstrated in (Schmitt & Stilla, 2014b) using millimeterwave experimental multifrequency polarimetric high-resolution interferometric system (MEMPHIS) data (Schimpf et al., 2002).

Phase estimation based on multibaseline interferometric SAR data was investigated using actual or simulated spaceborne systems (Fornaro et al., 2005; Fornaro et al., 2006): issues such as baseline estimation accuracy, atmospheric effects, temporal decorrelation, or the ratio between the actual and critical baselines (Bamler & Hartl, 1998) being highly relevant. Properties of airborne single-pass multibaseline data were also investigated using simulated data (Lombardo & Lombardini, 1997; Corsini et al., 1999). Actual airborne single-pass multibaseline systems such as MEMPHIS, PAMIR or OrbiSAR (Perna et al., 2008; Esposito et al., 2013) have additional concerns: issues such as dissimilar receiver properties leading to different antenna phase patterns, non-perfectly aligned phase centers, and inaccuracies in the motion compensation can decrease the phase estimation accuracy. On the other hand, these airborne single-pass systems use baselines order of magnitudes shorter than the critical baseline, atmospheric effects are similar for all receivers, and temporal decorrelation is not present as all baselines are acquired in a single pass.

The main research question within this paper is: does ML phase estimation of real airborne single-pass data effectively deliver better results, i.e., with a lower noise level, than those obtained from the longest baseline of the same system? If the answer is positive, which kind of processing is required to reach these results?

Terrain slopes facing the illumination direction cause a spatial decorrelation of the interferometric data. The extent of total spatial decorrelation rises with the baseline length (Lee & Liu, 2001). The longest baselines may not be the best choice on foreslopes. There the ML phase estimation is clearly superior to only using the longest baseline, since it weighs the contributions of the receivers based on its adaptive covariance matrix that takes the decorrelation into account. Hence this paper focuses on the least favorable scenario for ML phase estimation compared to

only using the longest baseline: it analyzes data acquired over flat grassland areas, where the longest baseline does not show increased spatial decorrelation.

To answer the research questions, data acquired with the MEMPHIS experimental Ka-band multibaseline system were used. A processing method developed for these data was already presented in (Magnard et al., 2014). For the phase unwrapping step, a C2F method was applied, which is very flexible but known to be suboptimal, since only part of the available information is kept in the final result. This paper introduces additional calibration steps that are required to apply ML phase estimation. It briefly describes the ML phase estimation and both processing chains from SLC data to a digital surface model (DSM). The results obtained with the ML method on flat verification areas with high coherence and homogeneous texture are then compared to those generated with the C2F method. Small but consistent improvements in reducing the noise level are shown, except when only few looks were employed (4 looks). In this case, more outliers were generated with the ML method, and the noise level was almost identical for both methods.

3.2 System characteristics

MEMPHIS is an experimental SAR system developed and operated by Fraunhofer/FHR (Wachtberg, Germany), usually installed onboard a C–160 Transall airplane (Schimpf et al., 2002). Table 3.1 summarizes the main system characteristics.

The data presented in this paper were acquired with the Ka-band multibaseline interferometric antennas. They use one transmit and four receive horns arranged vertically, enabling cross-track interferometry. The various available baselines and corresponding ambiguity heights for a standard setup are shown in Table 3.2.

TABLE 3.1
MEMPHIS SAR SYSTEM PARAMETERS

Carrier frequencies	35 GHz (Ka-band) and 94 GHz (W-band)
Bandwidth	900 MHz (stepped-frequency)
PRF	1500 Hz
Typical airplane velocity	77 m/s
Airplane altitude	300 – 1000 m
Antenna tilt angle	20° – 35°
Theoretical rg. resolution	0.167 m
Theoretical az. resolution	0.082 m in Ka-band, 0.061 m in W-band

TABLE 3.2
AVAILABLE BASELINES AND CORRESPONDING TYPICAL AMBIGUITY HEIGHTS FOR THE KA-BAND ANTENNA

Receiving Horns	Baseline [m]	Ambiguity Height [m] *
R_1, R_2	$B_1 = 0.055$	208.41
R_2, R_3 or R_3, R_4	$B_2 = 0.11$	104.21
R_1, R_3	$B_3 = 0.165$	69.47
R_2, R_4	$B_4 = 0.22$	52.1
R_1, R_4	$B_5 = 0.275$	41.68

* At mid-range (1547 m), sensor altitude: 770 m, antenna tilt angle: 30°

The SAR system was complemented by a differential GPS (DGPS) system working at 20 Hz and a precise inertial measurement unit (IMU or inertial navigation system/INS) working at 500 Hz. A three-axis accelerometer was installed directly on the SAR antenna assembly. Additional detailed system characteristics can be found in (Magnard et al., 2014).

3.3 Method

The method is presented in two steps. First the raw data focusing is reviewed briefly, followed by descriptions of additional calibrations of the antenna position and beam orientation. The interferometric chain is presented in the second step with its two variants using: 1) C2F phase unwrapping and 2) ML phase estimation. The latter is described in more detail, including a constant phase offset removal required in a calibration step. Corrections for interferometric phase errors, including elevation-dependent phase errors and errors related to imperfect motion compensation are outlined.

3.3.1 Raw data focusing

A detailed description of the raw data focusing can be found in (Magnard et al., 2014). Range focusing of all chirp parts is performed using matched filtering with chirp replicas. A stepped-frequency processing combines the 8 distinct 200 MHz bandwidths from the chirp parts into a single 900 MHz bandwidth (outlined in (Wilkinson et al., 1998; Lord, 2000)), and the azimuth focusing is achieved with an Extended Omega-K algorithm (Reigber et al., 2006). Calibration steps were added to the processing chain to increase the overall accuracy. The raw data focusing results in the four focused SAR images (SLCs) that are used as input for the interferometric processing chain (see Fig. 3.1).

3.3.1.1 Antenna tilt angle measurement

The MEMPHIS SAR antenna assembly is mechanically set to a fixed tilt angle at the beginning of a flight segment. The tilt angle is roughly known from a scale drawn on the assembly. To improve the accuracy of the antenna tilt angle measurement, the data from the accelerometer was compared to the IMU data: the accelerometer coordinate system was rotated such that the lateral and vertical components of the acceleration vectors measured by both systems were the same, with the rotation angle equaling the tilt angle. Additional details and calibration results are provided in the Appendix (Section 3.6.1).

3.3.1.2 Heading and pitch corrections

The azimuth and elevation axes of the SAR antenna beam are typically not perfectly aligned with the axes of the airplane reference frame. These discrepancies can be depicted as heading and pitch angular offsets to the platform attitude measured with the INS.

The sensor heading and pitch measurements were corrected as follows: for each acquisition, a large regular set of windows was selected throughout the illuminated area. For each window center, the Doppler centroid (DC) was calculated from the navigation data and estimated from the SAR data using a sign-Doppler estimator (Madsen, 1989). The pitch and heading offsets resulting in the smallest standard deviation between both DC estimation methods were selected through iterative computation.

Details of this estimation method as well as an overview of the results are reported in the Appendix (Section 3.6.2).

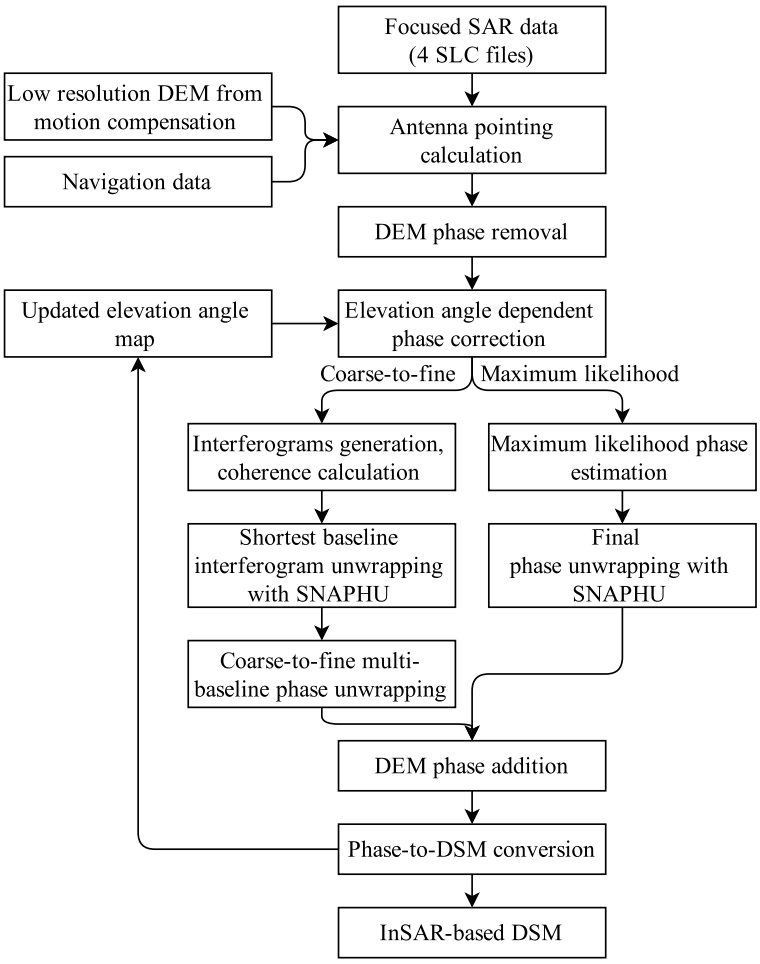

Fig. 3.1 Block diagram of the interferometric processing chains for both C2F and ML methods.

3.3.2 Interferometric processing chain

The interferometric processing chain is shown as a block diagram in Fig. 3.1. It was adapted from the processing chain presented in (Magnard et al., 2014) to be compatible with ML phase estimation. In that publication, a depression angle dependent phase correction was used to correct systematic error patterns in the range direction, i.e., depending on the beam elevation. However, the correction function neglected consideration of the platform attitude changes. Another error source reported in (Magnard et al., 2014) was the combination of platform attitude variations with scatterers above or below the height model used in the motion compensation. This leads to phase errors and thus height and geolocation errors after phase-to-height conversion. Implementing corrections for both issues requires a very accurate antenna pointing map (using the beam center approximation in the azimuth direction). Integration of the previously described precise antenna tilt angle measurements and heading and pitch corrections helps to improve the antenna pointing map accuracy.

ML phase estimation requires that the beam elevation angle phase correction be performed on each slave SLC dataset. Due to the low flight altitude and close range distance, the elevation angle of backscattered points within the antenna beam is strongly dependent on the terrain elevation and the height of the imaged objects. Thus an iterative process is needed: the first elevation angle-dependent phase correction is performed using a low resolution DEM (e.g., that employed for the motion compensation). A subsequent loop uses the results from the first iteration. The C2F ap-

proach could avoid this iterative process by performing the elevation angle-dependent phase correction within the *phase-to-DSM conversion*. It was implemented here as an iterative algorithm to ensure the most accurate cross-comparison of the final results.

The interferometric processing chain shown in Fig. 3.1 can be summarized as follows.

1) The InSAR processing method starts from the four previously generated SLCs.
2) The antenna pointing is estimated using the meta-data of the focused SAR data, the navigation data and a coarse resolution DEM (Section 3.3.2.1).
3) The phase corresponding to the coarse resolution DEM is subtracted from each SLC to expedite the phase unwrapping.
4) An elevation angle-dependent phase correction is carried out using the antenna elevation phase patterns and the antenna pointing map (Section 3.3.2.2).
5) The unwrapped phase is calculated using C2F or ML phase estimation methods (Sections 3.3.2.3 and 3.3.2.4).
6) The phase corresponding to the coarse DEM is added back.
7) The data are converted into a point cloud in Cartesian coordinates and transformed/resampled into a DSM in local map coordinates. The conversion from phase values to Cartesian coordinates uses at least one tie point, usually a reflector signature whose position was precisely measured using DGPS. The conversion algorithm was detailed in (Magnard et al., 2014); it now includes the motion compensation induced phase error correction proposed in Section 3.3.2.5. The results are used to compute an improved elevation angle map.
8) An iterative process is required to ensure that accurate values are available for the elevation angle phase correction.

3.3.2.1 Antenna pointing estimation

For each sample in the range-compressed data, an antenna pointing vector is calculated. Using the original, non-linearized navigation data (position, velocity and attitude information), we compute the intersection between 1) a plane perpendicular to the sensor roll axis passing through the sensor position and 2) the DEM used in the motion compensation. The range distance corresponding to the current sample and the beam look orientation (right or left) constrain the intersection to a single point. The resulting Cartesian coordinates are then backward geocoded (Meier et al., 1993) using the linearized flight track calculated in the motion compensation. This process yields their range and azimuth position in the focused SAR image. The relationship is finally inverted: a look up table is generated with the range/azimuth coordinates of the focused SAR image as input and the azimuth receive time and beam elevation as outputs. The antenna beam should move continuously in the forward direction (or more generally in the same direction); a direction change of the antenna beam caused by a rapid heading variation results in ambiguities (same area "illuminated" twice) that cannot be accounted for when inverted.

3.3.2.2 Elevation angle-dependent phase correction

The depression angle-dependent phase correction was modified from (Magnard et al., 2014) into an elevation-angle dependent phase correction, i.e., the calculated phase correction now relates on the relative elevation position in the radar beam, 0° being the beam center. The ML phase estimation requires that this correction be applied for each receiver separately. As the elevation antenna phase pattern can only be calculated for interferometric data, the data from the *master* receiver were left uncorrected. The phase patterns calculated from this *master* receiver combined with the 3 *slave* receivers were used to correct the phase of the *slave* receivers.

For each sample, the phase of the four channels was corrected as follows:

$$\begin{cases} \varphi_{\mathrm{A,\,j}}{}' = \varphi_{\mathrm{A,\,j}} \\ \varphi_{\mathrm{B,\,j}}{}' = \varphi_{\mathrm{B,\,j}} + \varphi_{\mathrm{corr,\,AB}}(\beta_{\mathrm{j}}) \\ \varphi_{\mathrm{C,\,j}}{}' = \varphi_{\mathrm{C,\,j}} + \varphi_{\mathrm{corr,\,AC}}(\beta_{\mathrm{j}}) \\ \varphi_{\mathrm{D,\,j}}{}' = \varphi_{\mathrm{D,\,j}} + \varphi_{\mathrm{corr,\,AD}}(\beta_{\mathrm{j}}) \end{cases} \tag{3.1}$$

with $\varphi_{\mathrm{X,\,j}}$ the uncorrected phase of channel X at pixel j, $\varphi_{\mathrm{X,\,j}}{}'$ the corrected phase and $\varphi_{\mathrm{corr,\,XY}}(\beta_{\mathrm{j}})$ the phase correction calculated for the channel X and Y combination for the interferogram generation using channels X and Y. All phase corrections were calculated depending on the elevation β_{j}.

3.3.2.3 C2F phase unwrapping

The coarse-to-fine approach is detailed in (Magnard et al., 2014). As illustrated in Fig. 3.1, it begins with calculation of the interferograms computed from SLC pairs. The interferogram generated from the shortest baseline/largest ambiguity height is first unwrapped with the SNAPHU algorithm (Chen, 2001). The interferograms with longer baselines are then sequentially unwrapped using information from the previously unwrapped interferograms.

3.3.2.4 ML phase estimation

The maximum likelihood phase estimation uses the model presented in (Lombardo & Lombardini, 1997). It is based on the assumption that all phase centers are perfectly aligned. The interferometric phase from pairs of MEMPHIS SAR data shows constant phase offsets, which contradict this alignment assumption. Whether or not they are caused by misalignments of phase centers, or by the elevation angle-dependent phase correction, or other reasons, these have to be corrected first.

Phase calibration is achieved as follows: the interferometric phase $\varphi_{\mathrm{shortest,\,j}}$ from the shortest baseline $\mathrm{B_{shortest}} = \mathrm{B_1}$ is used as a reference (see Table 3.2); the phase $\varphi_{\mathrm{long,\,j}}$ from a longer baseline $\mathrm{B_{long}} = \mathrm{B_3}$ or $\mathrm{B_{long}} = \mathrm{B_5}$ is corrected by subtracting a constant phase offset $\varphi_{\mathrm{offset,\,long}}$. This offset is calculated in two steps. The first step calculates the offset $\varphi_{\mathrm{offset,\,long,\,j}}$ for each interferogram cell j with

$$\varphi_{\mathrm{offset,\,long,\,j}} = 2\pi \cdot \left(F_{\mathrm{long,\,j}} - \lfloor F_{\mathrm{long,\,j}} \rfloor\right)$$
$$\text{with } F_{\mathrm{long,\,j}} = \frac{\mathrm{B_{long}}/\mathrm{B_{shortest}} \cdot \varphi_{\mathrm{shortest,\,j}} - \varphi_{\mathrm{long,\,j}}}{2\pi} \tag{3.2}$$

Cells with very low coherence (< 0.3) are discarded. A histogram is calculated, and the position of the histogram's maximum value is used as a first estimate of $\varphi_{\mathrm{offset,\,long}}$.

A solution space interval is selected as $\left[\varphi_{\mathrm{offset,\,long}} - \frac{\pi}{2}, \varphi_{\mathrm{offset,\,long}} + \frac{\pi}{2}\right]$ to avoid ambiguities. The final phase offset is calculated as the weighted average of cell-level phase offsets $\varphi_{\mathrm{offset,\,long,\,j}}$ within this interval, using the coherence as a weighting factor.

This phase calibration process assumes the phase from the shortest baseline to be unwrapped and/or the longer baselines being integer multiples of the shortest baseline.

The ML phase estimation is then achieved as follows: for each of the N looks $i = 1, \ldots, N$, the four complex values of the pixels from the four coregistered SLC, corresponding to the same area on the ground, are arranged in the vector

$$\mathbf{P}^{(i)} = \begin{bmatrix} P_1^{(i)} & P_2^{(i)} & P_3^{(i)} & P_4^{(i)} \end{bmatrix}^{\mathrm{T}} \tag{3.3}$$

From (Rodriguez & Martin, 1992), the vector $\mathbf{P}^{(i)}$ can be characterized as complex Gaussian random vector with zero mean value and covariance matrix $\mathbf{C} = E\left[\mathbf{P}^{(i)}\mathbf{P}^{\mathrm{H}(i)}\right]$ with $\mathbf{P}^{\mathrm{H}(i)}$ the Hermitian of $\mathbf{P}^{(i)}$. The covariance matrix can be rewritten (Lombardo & Lombardini, 1997) as $\mathbf{C} = \mathbf{\Phi\Gamma\Phi}^{*}$ with

$$\mathbf{\Gamma} = \begin{bmatrix} 1 & \rho_{1,2} & \rho_{1,3} & \rho_{1,4} \\ \rho_{2,1} & 1 & \rho_{2,3} & \rho_{2,4} \\ \rho_{3,1} & \rho_{3,2} & 1 & \rho_{3,4} \\ \rho_{4,1} & \rho_{4,2} & \rho_{4,3} & 1 \end{bmatrix}$$

and

$$\mathbf{\Phi}(\varphi) = \begin{bmatrix} 1 & 0 & 0 & 0 \\ 0 & e^{j\varphi\frac{B_2}{B_4}} & 0 & 0 \\ 0 & 0 & e^{j\varphi\frac{B_3}{B_4}} & 0 \\ 0 & 0 & 0 & e^{j\varphi} \end{bmatrix} \tag{3.4}$$

The correlation coefficients $\rho_{l,m}$ with $l, m = 1, \dots, 4, l \neq m$, are estimated from the data as

$$\hat{\rho}_{l,m} = \frac{\left|\sum_{i=1}^{N} P_l^{*(i)} P_m^{(i)}\right|}{\sqrt{\sum_{i=1}^{N}\left|P_l^{(i)}\right|^2 \sum_{i=1}^{N}\left|P_m^{(i)}\right|^2}} \tag{3.5}$$

The joint probability density function of the *N*-independent complex Gaussian vectors $\mathbf{P}^{(i)}$ conditioned to the interferometric phase value φ is

$$f\left(\mathbf{P}^{(1)}, \mathbf{P}^{(2)}, \dots, \mathbf{P}^{(N)}\middle|\varphi\right) = \prod_{i=1}^{N} f\left(\mathbf{P}^{(i)}\middle|\varphi\right) = \prod_{i=1}^{N} \frac{1}{\pi^K|\mathbf{C}|}\exp\left(-\mathbf{P}^{\mathrm{H}(i)}\mathbf{C}^{-1}\mathbf{P}^{(i)}\right) \tag{3.6}$$

with $|\mathbf{C}|$ the determinant of the covariance matrix and $K = 4$ in our case.

The interferometric phase is then estimated as the position of the maximum of the logarithmic likelihood function

$$L(\varphi) = -\sum_{i=1}^{N} \mathbf{P}^{\mathrm{H}(i)}\mathbf{\Phi}(\varphi)\mathbf{\Gamma}^{-1}\mathbf{\Phi}^{*}(\varphi)\mathbf{P}^{(i)} \tag{3.7}$$

with $\mathbf{\Gamma}^{-1}$ the inverse matrix of the correlation matrix $\mathbf{\Gamma}$.

The position of the maximum is searched within the wrapped interval in two steps: the first step delivers a rough estimation from a limited number of samples to find the global maximum. This global maximum is best defined in case of high coherence, so the grid size is inversely proportional to the coherence value. The second step begins with the first estimation and iteratively converges to a maximum position using the slope of the ML curve. The slope is calculated at two positions on each side of the current estimate; the position of the maximum is then estimated using the assumption that the slope of the curve varies linearly in the vicinity of the maximum. The optimization stops when the phase difference between current and previous estimations falls below a threshold value.

The ambiguity height after ML phase estimation corresponds to the least common multiple of all ambiguity heights, expressed as integer multiples of a reference ambiguity height; in the case of MEMPHIS Ka-band antenna, the resulting ambiguity height is that of the shortest available baseline, since all baseline lengths are multiples of the shortest baseline. As shown in Fig. 3.1, a final phase unwrapping step with SNAPHU algorithm may be performed to remove any residual wrapping, as necessary.

3.3.2.5 Motion compensation-induced phase error correction

The phase-to-height conversion model uses an approximated baseline calculated as the position difference between the linearized tracks. This approximation would deliver exact results only given perfect motion compensation, i.e., if the height used for the motion compensation were accurate or if the true baseline vector matched the approximated baseline vector. For a single-pass interferometric system, the only important parameter affecting the baseline vector is the platform actual attitude compared to the "linearized" attitude, i.e., mainly the roll angle variation. The error introduced through the used phase-to-height model and the approximated baseline thus mainly depends on 1) the difference between the real and "linearized" baseline vector combined with 2) the difference between the real off-nadir angle and the value used in the motion compensation. This error was identified in (Magnard et al., 2014) as a potential error source when using the interferometric height estimation method.

An approximate correction was implemented to partially improve the height accuracy, especially for targets with heights significantly different from the reference DEM used in the motion compensation (such as buildings or trees), as well as flights with high attitude variations. For each pixel of the focused SAR data, the correction was achieved by replacing an estimation of the phase correction originally performed in the motion compensation with a phase correction estimated using the coordinates of the pixel calculated through the interferometric processing. A detailed description of the correction method is available in the Appendix (Section 3.6.3).

3.4 Results

The results are based on 6 Ka-band datasets (M1-M6) acquired in May 2011 over Memmingen, Bavaria, Germany. The test site was close to an airport in a mostly flat area. Table 3.3 summarizes the geometrical characteristics of these acquisitions. Fig. 3.2 shows the geocoded amplitude images from all six acquisitions as a mosaic. Four trihedral corner reflectors were deployed and their positions determined using DGPS. They were illuminated from four directions and used as tie points for the phase-to-DSM conversion. The acquisitions are the same as those presented in (Magnard et al., 2014).

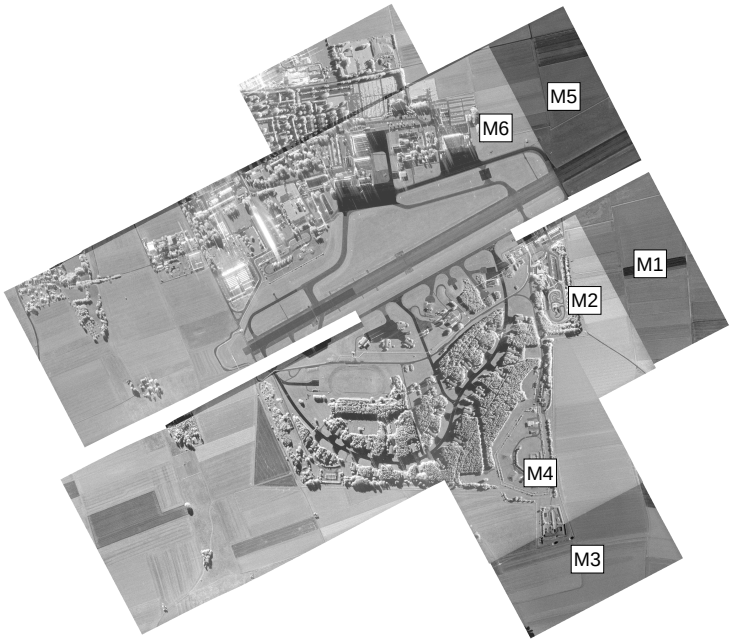

Fig. 3.2 Overview of acquisitions M1 – M6 at Memmingen: to enhance the visibility of all acquisitions, two different radiometric scaling factors were employed for the geocoded amplitude images.

TABLE 3.3
MEMMINGEN ACQUISITION CHARACTERISTICS

Acquisition	M1	M2	M3	M4	M5	M6
Mean sensor altitude [m]	770					
Near range distance [m]	1250					
Range swath width [m]	600					
Acquisition length [km]	2.08	2.2	2.12	2.06	2.2	2.07
Heading [°]	60	240	150	330	60	240
Illumination direction [°]	330	150	60	240	330	150

The antenna tilt angle measurement, antenna beam pointing calibration (pitch and heading adjustment) and motion compensation-induced phase correction were crucial steps for improving the results presented in (Magnard et al., 2014) and for allowing ML phase estimation. These activities are shortly presented in the Appendix, as they are not the main focus of this paper.

In the following, the effect of the elevation angle-dependent phase correction is shown. Then an example of the ML phase estimation for a single point is given. Next, the results collected on a set of flat homogeneous surfaces with high coherence are analyzed: we compare the measured noise level and the distribution of outliers between both ML and C2F methods. Finally, the statistical significance of the noise levels is tested.

3.4.2 Elevation angle-dependent phase correction

The elevation angle-dependent phase correction functions were calculated from the data for all receiver combinations. Fig. 3.3 shows the calculated correction curves $\varphi_{\mathrm{corr,\,AB}}$, $\varphi_{\mathrm{corr,\,AC}}$ and $\varphi_{\mathrm{corr,\,AD}}$ that were used for the ML method. Fig. 3.4 illustrates the effect of the elevation angle-dependent phase correction for acquisition M1 (C2F phase unwrapping method). In that case, the phase corrections resulted in height rectifications ranging from -0.4 m to $+0.5$ m. The wave-like deviations in range direction are clearly visible on the uncorrected image, with a predominant overshooting in near range (yellow–red) and an undershooting in far range (blue).

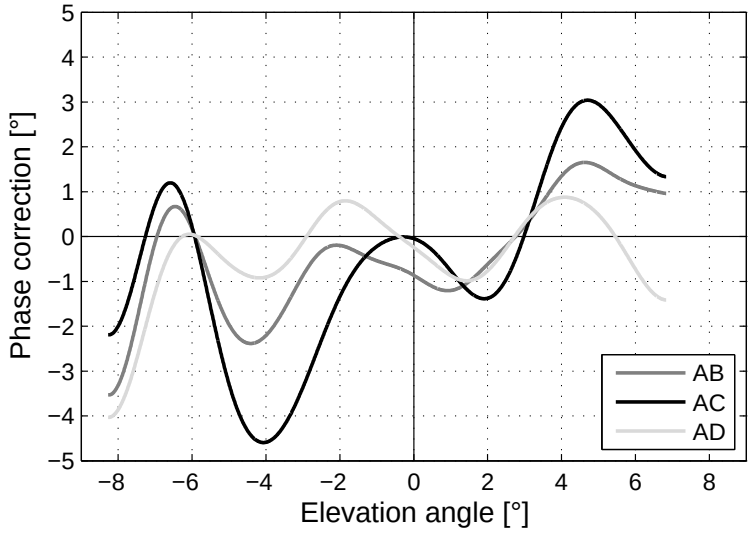

Fig. 3.3 Relative elevation angle-dependent phase correction curves for channels B, C and D. 0° corresponds to the beam center. Negative elevation angle values are below the beam center, while positive values are above the beam center.

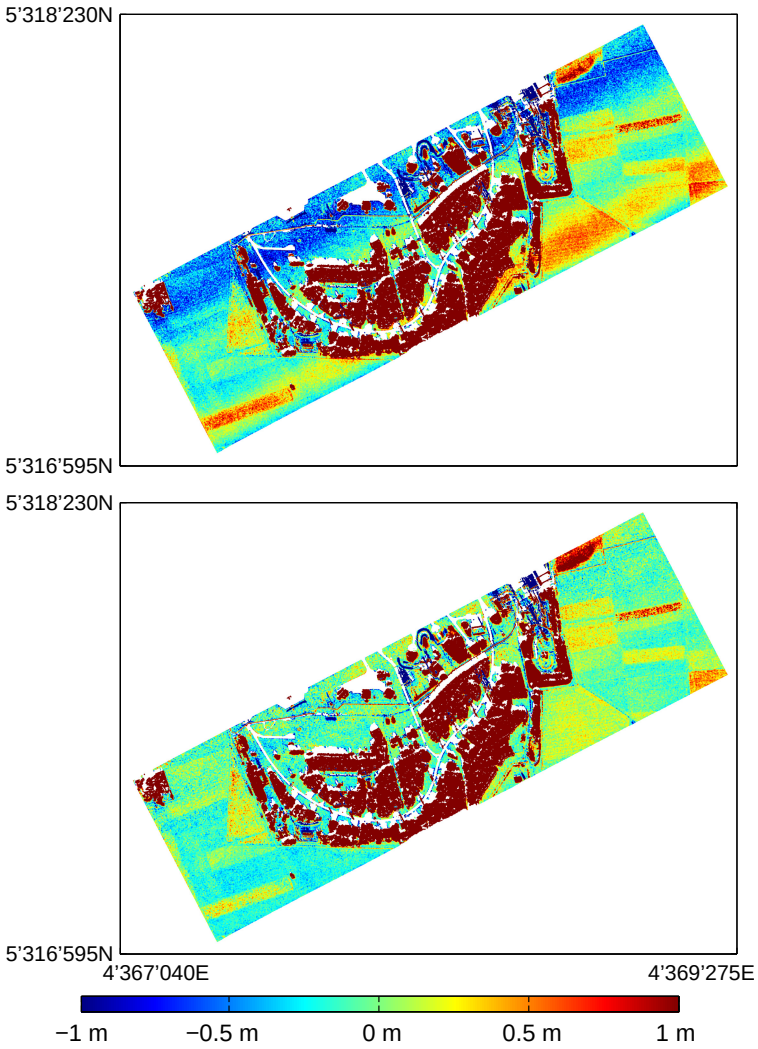

Fig. 3.4 Height difference between the InSAR DSM calculated from acquisition M1 and an ALS DTM, without (top) and with (bottom) elevation angle-dependent phase correction (C2F method). White areas are areas with low coherence. Coordinate system: German Gauss-Krüger strip 4, elevation over DHHN92 (Deutsches Haupthöhennetz 1992—German mean height reference system 1992) reference.

3.4.3 ML phase estimation

An example of ML phase estimation for one sample is shown in Fig. 3.5. The gray curve is the result of estimation without calibration of the phase, i.e., without correction of the constant phase offsets $\varphi_{\text{offset, long}}$ with respect to the longer baselines. A less-careful maximum estimation might result in a local maximum instead of the global maximum. The black curve is the same cell after correction of the constant phase offsets and shows a more pronounced maximum. Note that most cases show much lower secondary local maxima, this one was chosen as a "worst" case to better show the utility of the correction of the constant phase offset. The maximum is also shifted; this phase shift is typically constant over the whole dataset. Since the absolute phase is determined with the help of one or several tie points, it does not have any influence on the final result.

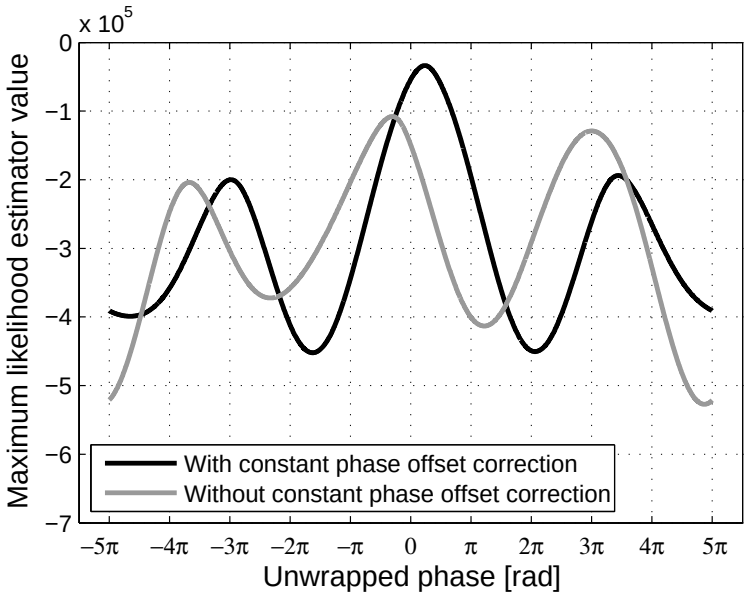

Fig. 3.5 Logarithmic likelihood function for a single point. The gray curve was calculated without correction of constant phase offsets, the black curve with correction.

TABLE 3.4
NUMBER OF LOOKS TESTED IN THE INTERFEROMETRIC PROCESSING

Range looks	Azimuth looks	Range pixel spacing [m]	Azimuth pixel spacing [m]
1	4	0.167	0.207
2	8	0.333	0.414
3	12	0.500	0.621
4	16	0.666	0.828
5	20	0.833	1.035
6	24	0.999	1.242
10	40	1.665	2.070

The azimuth pixel spacing corresponds to the average over the six tested datasets at Memmingen.

3.4.4 Noise Level and outliers comparison

The noise level was compared between results from C2F and ML processing chains. For this, the acquisitions M1–M6 were processed with both chains, using different numbers of looks (boxcar windows) as shown in Table 3.4. In order to best compare both methods, no further filtering was used (such as removing low coherence pixels or using median filters for noise reduction). The comparison between both methods was achieved over flat verification areas found in the surveyed zone where the data showed high interferometric coherence. The flatness of these areas was validated by checking the height standard deviation against ALS reference data. The selected areas had homogeneous textures, hence local stationarity can be assumed, i.e., all pixels used for the estimation of one interferometric phase value belong to the same statistical distribution. The exact same areas in range/azimuth coordinates were selected for both methods. They were the size of football fields and located in a diverse set of range positions. Fig. 3.6 shows an acquisition and the area selected for the study of the interferometric noise. Fig. 3.7 shows the height and coherence of this area of interest.

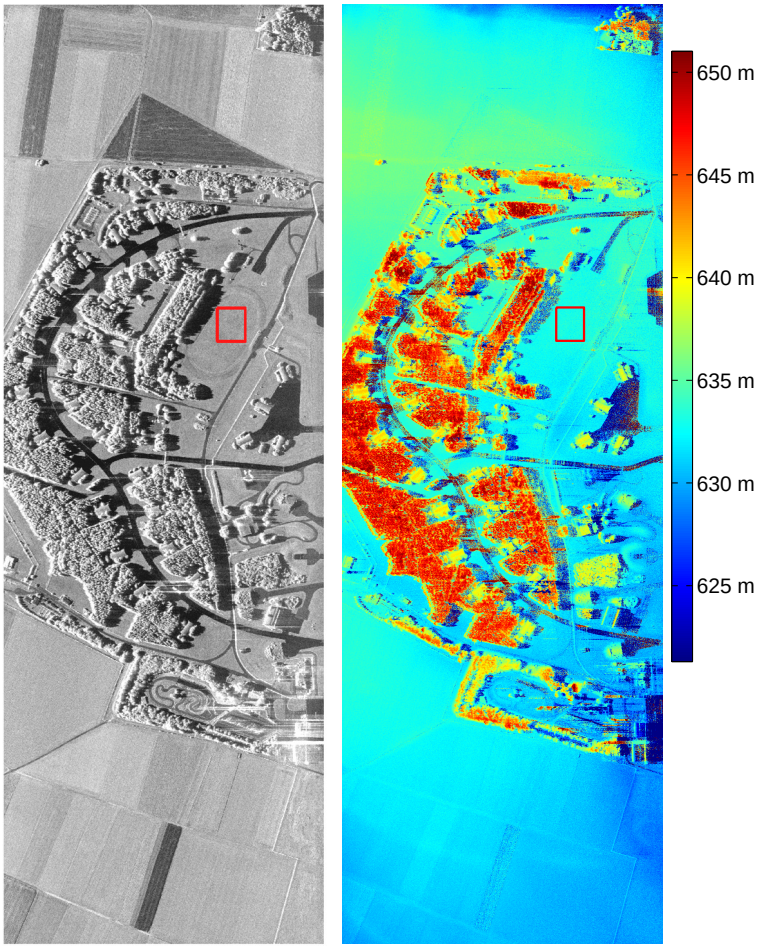

Fig. 3.6 Left: amplitude image of acquisition M1 at Memmingen, Germany. Right: height calculated through the ML InSAR processing. Azimuth and slant range extent of acquisition: 2.1 × 0.6 km. The red rectangle shows the flat area studied in this acquisition.

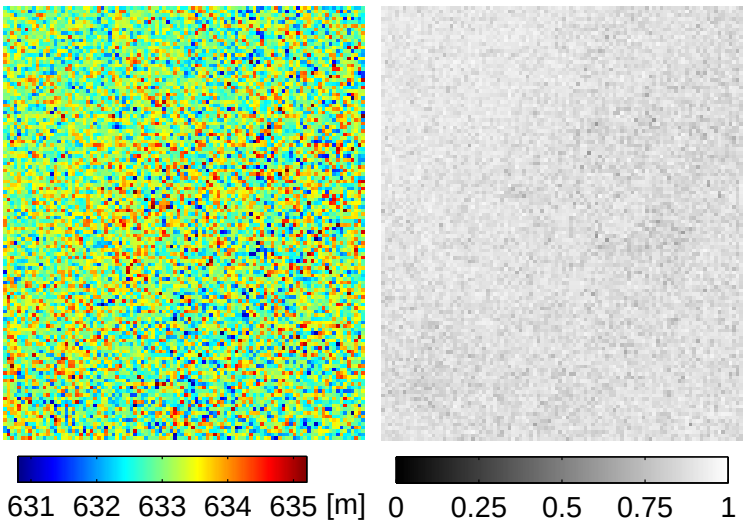

Fig. 3.7 Left: height of the selected area on acquisition M1 (rectangle shown in Fig. 3.6). Right: corresponding coherence map. In this case 3 range and 12 azimuth looks were used.

The height standard deviation directly depends on the range position, related to the local ambiguity height $h_{2\pi}$. Aggregating height standard deviations of areas located at different range distances would be misleading. Thus the analysis was made on phase values. A first statistical analysis was made directly using the unwrapped phase (before DEM phase addition and phase-to-DSM conversion, see Fig. 3.1). The histograms showed strongly non-Gaussian shapes, especially when a high number of looks was used. A potential explanation is that the flat Earth removal was not accurate enough, leaving trends in the phase behavior. The solution was found to convert the resulting elevation values back into phase values.

The conversion was made as follows: the mean elevation was first subtracted from the height map; this height difference $\mathrm{h}_{\mathrm{diff,\,i}}$ was then converted into a phase difference $\varphi_{\mathrm{diff,\,i}}$ through $\varphi_{\mathrm{diff,\,i}} = \mathrm{h}_{\mathrm{diff,\,i}} \cdot \frac{2\pi}{h_{2\pi,\,\mathrm{center}}}$ with $h_{2\pi,\,\mathrm{center}}$ the ambiguity height in the center of each verification area. The ambiguity height is calculated as follows (Rosen et al., 2000):

$$h_{2\pi} = \frac{\lambda r \sin\theta}{pB\cos(\theta - \alpha)} \tag{3.8}$$

with λ the wavelength, r the range distance, θ the off-nadir angle, $p = 1$ for a common transmitter, B the baseline length and α the baseline inclination. While it remains an approximation, this height-to-phase conversion allowed for removal of the range dependency and aggregation of the data from all six datasets.

The data departed significantly from a normal distribution: as many outliers were present, especially when only four looks were used, a calculated standard deviation resulted that is unrepresentative of the histogram of the distribution. In order to achieve a meaningful characterization, a Gaussian fit was calculated as follows. The data were filtered using min/max threshold values. The threshold values were calculated iteratively using a ±3 σ window centered at the mean position. In each iteration, the values outside the window were discarded and a new window was calculated until the threshold values converged. Fig. 3.8 shows the histogram of the distribution for 1 range and 4 azimuth looks and the Gaussian curves representing normal distributions for the non-filtered and filtered standard deviations (ML method).

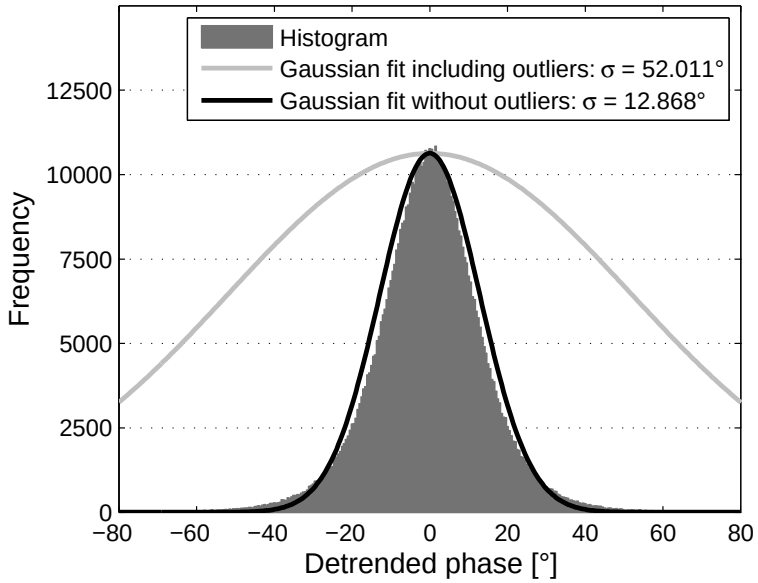

Fig. 3.8 Distribution of the detrended phase for one range and four azimuth looks, using the ML method. All six selected rectangular areas were combined to produce the figure, totaling 648000 samples. 2.56 % of the samples (16607 samples) were detected as outliers. The histogram used a 0.5° bin width.

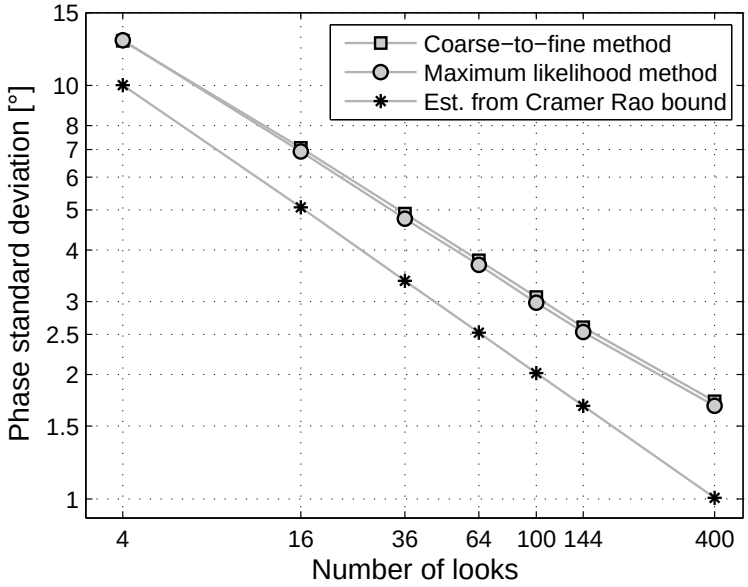

Fig. 3.9 Noise comparison between C2F and ML methods using the aggregated data from all six selected rectangular areas. The phase standard deviation is plotted against the number of looks in a log–log scale. The figure shows the standard deviation estimated via Cramer-Rao bound.

TABLE 3.5
MAXIMUM LIKELIHOOD VS COARSE-TO-FINE SIGNIFICANCE ANALYSIS

Looks	$F = \frac{\sigma^2_{C2F}}{\sigma^2_{ML}}$	H_0	p-value	Confidence interval
4	0.9932	rejected	$6.65 \cdot 10^{-3}$	(0.9883; 0.9981)
16	1.0418	rejected	$2.06 \cdot 10^{-16}$	(1.0317; 1.0521)
36	1.0595	rejected	$1.05 \cdot 10^{-14}$	(1.0441; 1.0752)
64	1.0521	rejected	$3.46 \cdot 10^{-7}$	(1.0317; 1.0728)
100	1.0655	rejected	$3.50 \cdot 10^{-7}$	(1.0398; 1.0918)
144	1.0544	rejected	$3.99 \cdot 10^{-4}$	(1.0239; 1.0857)
400	1.0511	rejected	$4.53 \cdot 10^{-2}$	(1.0010; 1.1037)

The noise level using both maximum likelihood and coarse-to-fine methods is presented in Fig. 3.9 for all tested numbers of looks on a log–log scale. The expected noise level from Cramer-Rao bound is also plotted on the figure. The Cramer-Rao bound (Rodriguez & Martin, 1992) provides a lower bound on the phase noise level, and is dependent on the observed coherence γ as follows:

$$\sigma_{\varphi,\,\text{Cramer-Rao}} = \frac{1}{\sqrt{2N_L}} \frac{\sqrt{1-\gamma^2}}{\gamma} \tag{3.9}$$

with $\sigma_{\varphi,\,\text{Cramer-Rao}}$ the estimated phase standard deviation and N_L the number of looks. The coherence of the interferograms with the longest baseline, averaged over all verification areas, was used to calculate Cramer-Rao bound shown in Fig. 3.9. This coherence value varied between 0.89 and 0.90, depending on the number of looks.

A significance analysis was driven on these results using an F-test. A 5% significance level was used, i.e., the null-hypothesis H_0 being that the variance σ^2_{c2f} using the C2F method and the variance σ^2_{ML} using the ML method are the same is rejected if the probability that both variances are the same is lower than 5%. Table 3.5 summarizes the statistical results.

The proportion of outliers and their magnitude were calculated (see Fig. 3.10). Note that in the case of a normal distribution, 0.3% of the samples should be outside a ±3 σ window. This is clearly not the case for low numbers of looks. Fig. 3.11 shows the distribution of outliers for both methods: in the case of the C2F method, the maximum error in highly coherent, continuous surfaces should not be higher than $\pm\pi$ from the algorithm itself, while in the case of the ML phase estimation, the worst cases reach $\pm 5\pi$. Fig. 3.12 plots the coherence for both regular data and outliers, depending on the number of looks: the coherence was generally significantly lower for the outliers, as expected.

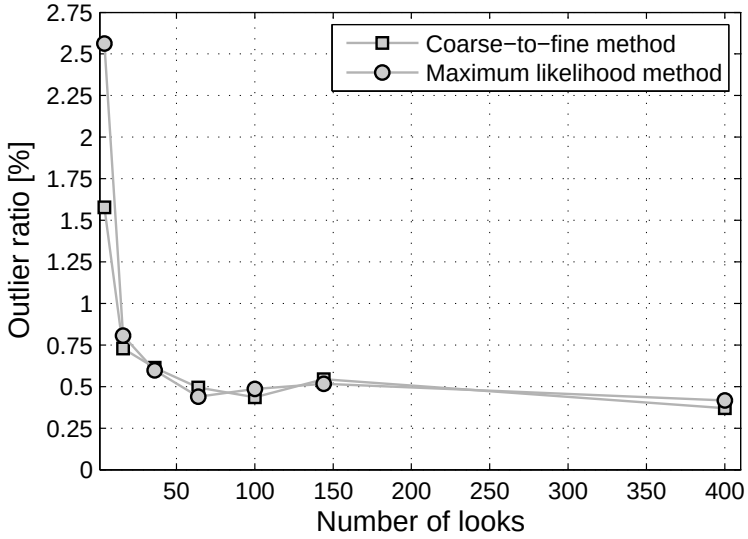

Fig. 3.10 Ratio of outliers relative to the number of looks for both ML and C2F methods.

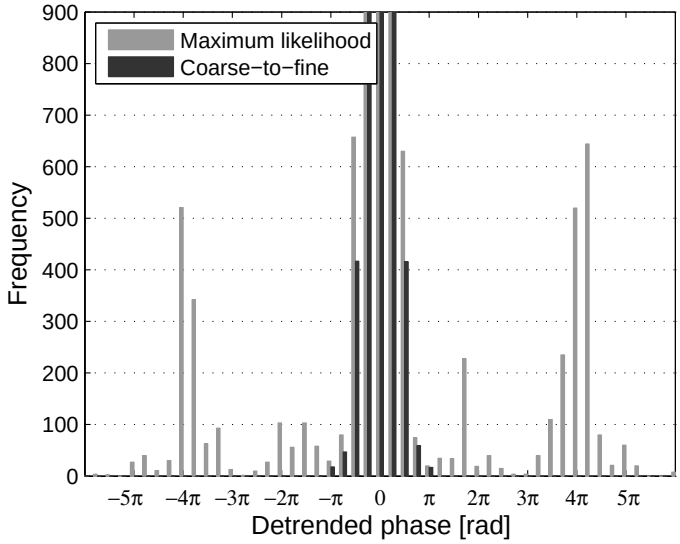

Fig. 3.11 Outliers distribution for one range and four azimuth looks, using both ML (same data as in Fig. 3.8) and C2F methods. The histogram uses $\boldsymbol{\pi/4}$ radian bin width and is scaled to highlight the outliers.

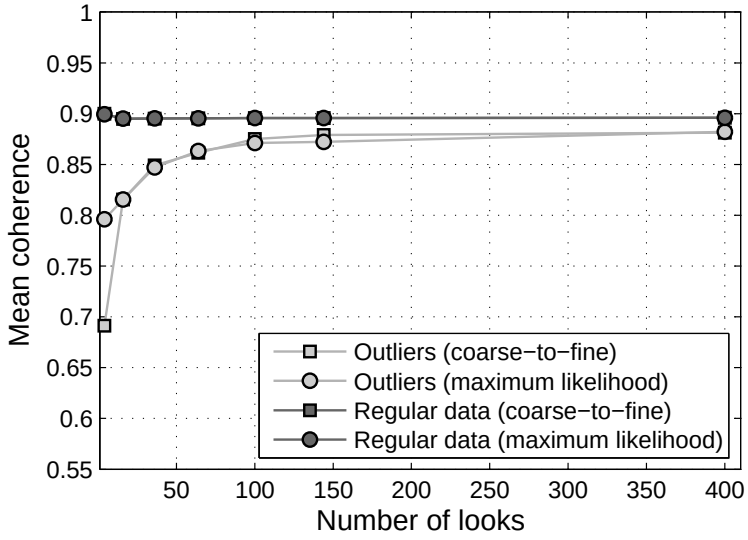

Fig. 3.12 Coherence of regular data and outliers relative to the number of looks for both ML and C2F methods.

3.5 Discussion

3.5.1 Comments on the data calibration

The first attempts to use ML method delivered poor and misleading results compared to the C2F method shown in (Magnard et al., 2014), with high outlier proportion and with varying elevation angle-dependent phase errors. MEMPHIS data did not match well enough the assumptions made in the model behind the ML phase estimation. Carefully designed calibration steps were required to bring the data closer to the model. These calibration steps included elevation angle-dependent phase correction for the three slave receivers extended from the depression angle-dependent phase correction presented in (Magnard et al., 2014) as well as a constant phase offset applied to two of the four SLC data.

The calibration steps were enhanced by an improved estimation of the antenna tilt angle and a refined estimation of the beam orientation. The antenna tilt angle was accurately determined using an accelerometer fixed to the antenna assembly. The results were noisy but stable when averaging over a full acquisition duration. Results from acquisitions with the same antenna position were very stable, with less than 0.03° difference between the tilt angle calculated during a single acquisition and the overall average (see Table 3.7 in the Appendix, Section 3.6.1). The pitch and heading angles of the sensor were tuned using a steepest-descent algorithm until the DC estimated from the SAR and navigation data best matched each other. The calculated pitch and heading offsets were again very stable across all acquisitions (less than 0.04° and 0.02° difference for the heading and pitch angles compared to the overall average, respectively, see Table 3.8 in the Appendix, Section 3.6.2). Moreover, these calibration steps also led to improved motion compensation and thus lower phase errors.

A motion compensation-induced phase error correction was also added. It corrected errors that appear when the real sensor attitude (roll angle in particular) is different from the linearized attitude and the terrain elevation used in the motion compensation is different from the real one. In the case of the data presented in this paper, the roll angle variation was very small for all acquisitions ($\leq 1.1°$); moreover the noise was studied in flat areas where the elevation used in the motion compensation (we used a smoothed SRTM-DEM elevation (Farr et al., 2007)) can be assumed as close to the real elevation. This correction, therefore, only had a tiny influence on the final results presented here (< 1 cm, see Fig. 3.14 in the Appendix, Section 3.6.3). Tests on other data not

presented here with larger roll angle variations (~6°) and taller objects (> 40 m) resulted in corrections of up to ~30 cm. Note that other uncorrected error sources linked to the processing method were analyzed in (Magnard et al., 2014).

Both implemented corrections for the beam elevation angle-dependent phase error and motion compensation-induced phase error are effective in this case due to MEMPHIS short azimuth beam width (3°, corresponding to ~80 m at mid-range). A more generic correction of such errors would require an iterative processing of the SAR data: once a DEM had been calculated, it would be used to refocus the SAR data with more accurate motion compensation. This requires an aperture-dependent motion compensation (Prats et al., 2007) (the motion compensation used here is a range-and-topography-dependent method using beam center approximation).

The calibration steps introduced in the article are summarized in Table 3.6 which lists the purpose of each, and, when available, their magnitude.

TABLE 3.6
SUMMARY OF THE CALIBRATION STEPS

Calibration step	Description
Antenna tilt angle measurement	• Correction up to 1.5° w.r.t. nominal value • Purpose: - Motion compensation in az. focusing - Antenna pointing calculation - Baseline vector calculation
Heading and pitch corrections	• Offset magnitude up to 1° • Purpose: - Motion compensation in az. focusing - DC calculation in az. focusing - Antenna pointing calculation - Baseline vector calculation
Antenna pointing calculation	• Purpose: - DEM phase removal - Elevation angle-dependent phase correction - Motion compensation-induced phase error correction
Elevation angle-dependent phase correction	• Purpose: - Correction of systematic phase errors in the range direction - Improved ML phase estimation • Height rectifications between -0.4 and $+0.5$ m
Motion compensation-induced phase error correction	• Purpose: - Correction of phase errors caused by inaccurate motion compensation • Height rectifications typically < 1cm, up to ~30 cm in worst cases (tall objects, large attitude changes)
Phase calibration in ML estimation	• Purpose: - Constant phase offset removal - Improved ML phase estimation

3.5.2 Comments on the noise level and outliers comparison

The results show that with only four looks, the noise level was marginally higher with the ML approach than with the C2F method, with more outliers. However, with more looks, the ML method consistently delivered a lower noise: noise variance using the C2F approach was steadily ~1.05 times the variance obtained with ML method, with a similar number of outliers for both methods. The difference between the results from both methods was validated with a significance analysis. The null-hypothesis that the results from both methods had the same variance was re-

jected for all look numbers, meaning that the differences between the results were all found statistically significant at a 5% level, even the very small difference when using four looks; the least significant result was the one obtained using 400 looks, due to the limited amount of samples.

Regarding the absolute results, the measured noise ranged from a standard deviation $\sigma(N_L = 4) \cong 12.85°$ with 4 looks to $\sigma(N_L = 400) \cong 1.68°$ with 400 looks. These values correspond to ~1.5 m and ~0.195 m at mid-range. Estimation of the expected noise using the Cramer-Rao bound was consistently lower than the measured one. The standard deviation of the actual phase noise was typically 1.25–1.7 times the standard deviation estimated using Cramer-Rao bound. This relative factor depended on the number of looks, growing larger when more looks were used, while the absolute difference decreased with the number of looks. With 400 looks, the difference between the measured noise and the estimation with Cramer-Rao bound was ~0.68°, corresponding to 0.079 m at mid-range. This difference might primarily correspond to the remaining topography (the selected areas were not perfectly flat); the standard deviation of ALS data used as reference was ~0.072 m for the same selected areas. Note that in contrast to the results shown in (Magnard et al., 2014), no coherence threshold was used this time.

These results were obtained on flat areas showing high coherence; flat areas with slightly reduced coherence (e.g., on the runway) led to the same results, which is a small improvement with the ML method compared to the C2F method. Again, the estimation of the phase noise standard deviation using Cramer-Rao bound was lower than the measured phase noise, similar to the results obtained in the verification areas. No flat areas were found with moderate coherence (~0.5): MEMPHIS interferometric data only deliver either high coherence (> 0.7) or very low coherence (close to 0) in shadowed areas or areas showing specular reflection.

Outliers were discarded from the data to compute the phase standard deviation. As shown in Fig. 3.10, these outliers were observed mainly when using 4 looks, they were significantly reduced with 16 looks and almost disappeared with 36 looks, i.e., they neared the number of outliers expected in a normal distribution (0.3% of the samples outside ± 3 σ). Per the algorithms design, these outliers can be much larger with ML than C2F method. Using 4 looks, they severely hampered the results with the ML method. The coherence of the outliers was compared to the coherence of regular data; it was significantly lower, especially with a low number of looks.

3.5.3 Conclusion and outlook

While the calibration steps might be different with other systems, in the case of a single-pass multibaseline system, the interferometric phase between all slave receivers and the master receiver should be first carefully studied, before using ML phase estimation. Single-pass multibaseline interferometric SAR systems use many antennas that may have slightly different behaviors. In particular, for experimental systems, this may come from slightly different receiving antenna shapes, inconsistent electrical characteristics of components, or phase center misalignment.

Regarding the noise comparison, a larger difference in favor of ML had been hoped for from personal communications and literature surveys (Lombardo & Lombardini, 1997; Lombardini & Griffiths, 2001), where improvements from the multibaseline ML method over single baseline results were demonstrated in particular for large baseline/critical baseline ratios. Ka-band results reported here using relatively short baselines are consistent with what was reported in (Lombardini & Griffiths, 2001) for small baseline/critical baseline ratios (Fig. 2-9 in (Lombardini & Griffiths, 2001)). An additional factor might explain the modest improvement: the signal from all four receivers was not exactly the same; in fact the signal-noise ratio characteristics of the four channels varied considerably, probably linked to different electrical characteristics in the receivers (such as amplifiers, A/D conversion). Thus the combined interferometric phase from all four receivers might only be marginally better than the interferometric phase from the receivers form-

ing the longest baseline, if these two channels are qualitatively better than one or both other channels. Improved channel characterization and the use of an adapted covariance matrix might help, but in the end antennas with the closest possible characteristics would be the best solution.

A limited number of outliers degraded the results, especially when using a low number of looks. Their coherence was also shown to be lower than the coherence of regular data. From these considerations, these outliers can be removed using a coherence threshold, median or other filters. Other possibilities include coherence weighting within a regridding step or adaptive filtering depending on the coherence.

The Cramer-Rao bound delivers an estimation of the best achievable phase noise given a coherence value and a number of looks. The measured phase noise was larger than this estimation, probably due to real world parameters such as vegetation height variations, residual topography, and system and processing imperfections. The Cramer-Rao bound and the study carried out here can be used to estimate the phase noise for all individual points from an acquisition. Having an estimation of the noise level for each point of the point cloud in Cartesian coordinates can be useful for any subsequent step, e.g., the regridding step in the DSM generation.

The analysis presented here was limited to flat and homogeneous areas where the use of boxcar windows is ideal, with data following the local stationarity assumption; for areas with irregular scattering mechanisms and rough topography, as observed for example in urban areas, the local stationarity assumption using simple boxcar windows no longer holds true. In that case, better results can be obtained using an adaptive sample selection that ensures the samples used in the ML estimation follow the stationarity assumption (Vasile et al., 2006). In (Schmitt & Stilla, 2014a), a similar process leads to the estimation of an adaptive covariance matrix.

The ML phase estimator used here provides a single phase estimation for each point target. For decorrelating targets with multiple scattering mechanisms that occur, e.g., in layover areas, tomographic SAR methods are able to resolve up to K-1 scatterers, where K is the number of receivers. Since MEMPHIS only has four receiving antennas, up to three scatterers could be theoretically resolved. An ML-based SAR tomography approach was introduced in (Schmitt & Stilla, 2014b) and tested with MEMPHIS data. Other tomography methods such as Capon (Capon, 1969) or MUSIC (Schmidt, 1986) beamforming could also be considered; these were demonstrated in (Frey & Meier, 2011) using airborne multiple-pass multibaseline SAR data.

ML phase estimation was shown to perform slightly better than C2F method in the scenario least favorable for ML, i.e., using data acquired on flat grassland areas where spatial decorrelation does not drastically increase with the baseline length. This implies that we can expect ML to perform universally better than C2F method. Therefore, through the study conducted here, ML phase estimation was shown to be well adapted to an experimental single-pass, multibaseline airborne SAR interferometric system, after careful SAR data focusing and all necessary calibration steps.

Acknowledgments

The authors would particularly like to thank Christian Ackermann from the TU Munich for lending the INS hardware and for his invaluable technical assistance. The authors would also like to thank the anonymous reviewers for their very helpful comments.

3.6 Appendix

3.6.1 Antenna tilt angle measurement

The raw, non-calibrated, accelerometer data were first transformed into [m/s^2] values, yielding $\left[a_{\text{acc},\,x}, a_{\text{acc},\,y\prime}, a_{\text{acc},\,z\prime}\right]^T$. The acceleration data from the IMU $\left[a_{\text{IMU},\,x}, a_{\text{IMU},\,y}, a_{\text{IMU},\,z}\right]^T$ do not include gravity g, which must be added to allow intercomparison between the two data sources. For simplicity, only the right and down components are treated, i.e., as though both IMU and accelerometer sensors were mounted along parallel axes in the longitudinal direction (x), which was the case. The following relationship between the acceleration measured by the IMU $\begin{pmatrix} a_{\text{IMU},\,y} \\ a_{\text{IMU},\,z} \end{pmatrix}$ and that measured by the accelerometer $\begin{pmatrix} a_{\text{acc},\,y\prime} \\ a_{\text{acc},\,z\prime} \end{pmatrix}$ holds

$$\begin{pmatrix} a_{\text{IMU},\,y} \\ a_{\text{IMU},\,z} \end{pmatrix} + g \cdot \cos\theta \cdot \begin{pmatrix} \sin\varphi \\ \cos\varphi \end{pmatrix} = \mathrm{s} \cdot \begin{pmatrix} \cos\eta & -\sin\eta \\ \sin\eta & \cos\eta \end{pmatrix} \begin{pmatrix} a_{\text{acc},\,y\prime} \\ a_{\text{acc},\,z\prime} \end{pmatrix} \tag{3.10}$$

with θ the pitch angle, φ the roll angle and η the antenna tilt angle. (x, y, z) corresponds to the (forward, right, down) reference body frame. (x, y', z') is the body frame rotated about the longitudinal axis by the angle η. s is a correcting scaling factor correction linking the acceleration measured by the accelerometer $\|\vec{a}_{\text{acc}}\|$ with the one measured by the IMU $\|\vec{a}_{\text{IMU}}\|$. It is calculated as follows:

$$\begin{gathered} \mathrm{s} = \frac{\sqrt{\mathrm{M}^2 + \mathrm{N}^2}}{\sqrt{a_{\text{acc},\,y\prime}^2 + a_{\text{acc},\,z\prime}^2}} \\ \text{with } \mathrm{M} = a_{\text{IMU},\,y} + g \cdot \cos\theta \cdot \sin\varphi \\ \text{and } \mathrm{N} = a_{\text{IMU},\,z} + g \cdot \cos\theta \cdot \cos\varphi \end{gathered} \tag{3.11}$$

The antenna tilt angle can be calculated from equations (3.10) and (3.11)

$$\cos\eta = \frac{\mathrm{M} \cdot a_{\text{acc},\,y\prime} + \mathrm{N} \cdot a_{\text{acc},\,z\prime}}{\mathrm{s} \cdot \left(a_{\text{acc},\,y\prime}^2 + a_{\text{acc},\,z\prime}^2\right)} \tag{3.12}$$

The angle η is calculated for each sample. The average over many acquisitions with the same setup is used as an estimate of the antenna tilt angle.

For the six acquisitions presented in this paper, the combined mean tilt angle was 30.6527°, with 0.1456° standard deviation; when considering the six acquisitions separately, the measured tilt angle was very stable. The values are listed in Table 3.7.

TABLE 3.7
MEASURED ANTENNA TILT ANGLE

	Mean [°]	Standard dev. [°]
M1	30.6278	0.1398
M2	30.6512	0.1255
M3	30.6351	0.1568
M4	30.6717	0.1678
M5	30.6675	0.1293
M6	30.6607	0.1458
Combined data	30.6527	0.1456

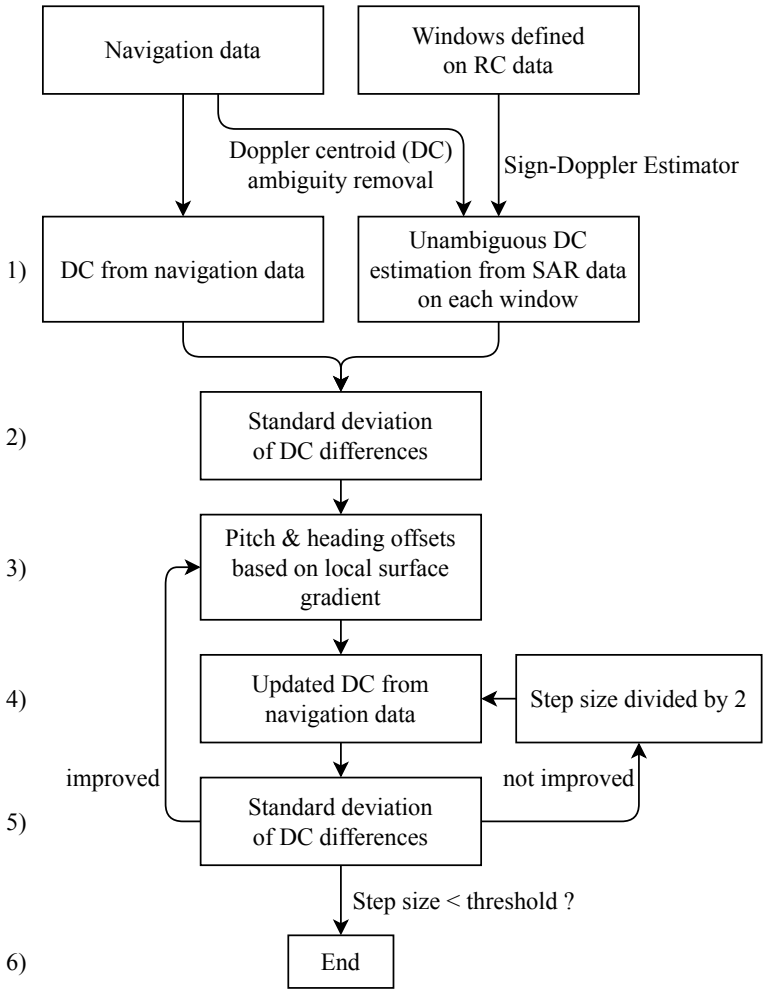

Fig. 3.13 Flowchart of the heading and pitch offsets calculation.

3.6.2 Heading and pitch correction: optimizing method

A steepest descent method was used to estimate the true heading and pitch offsets. This iterative method works as follows: a 3D-representation is used, with the heading offset as the x-axis, the pitch offset as the y-axis and the mean DC frequency difference as the z-axis. The optimizing problem consists of finding the minimum of this surface. An overview of the following steps is given in Fig. 3.13.

1) For each window, initial DC frequencies are calculated using both the navigation data and the sign-Doppler estimator (with potential ambiguities resolved using the DC calculated from the navigation data).
2) The standard deviation of the DC differences is calculated.
3) Three heading/pitch coordinates around the current coordinate allow calculation of the local surface gradient. The normed up-pointing perpendicular vector to this plane is calculated. The x and y components of this vector point in the direction of improved heading/pitch offsets. They are multiplied by a step size (initially 0.1°).
4) The new DC frequencies are calculated from the modified navigation data.
5) The standard deviation of the new DC differences is calculated. If it is worse than the previous value, the step size multiplying the vector calculated in (3) is divided by 2 and step

(4) is repeated. Once a lower standard deviation of DC differences is found, the algorithm returns to (3).

6) The process stops when the step size reaches a minimum threshold value.

The windows with DC differences outside three standard deviations of the mean DC difference are discarded. This ensures that inaccurate DC estimations in low SNR windows are avoided.

Once five successful iterations are achieved, linear fits are calculated after step (5) on the heading/pitch offsets history (not shown on the flowchart to not impair readability). Extrapolated heading/pitch offsets are tested to see if they result in a lower standard deviation of DC differences. If so, further regression-based extrapolation is carried out, otherwise the process returns to step (3). This process reduces the number of iterations required due to zigzagging effects.

The optimized values calculated for the Memmingen acquisitions are shown in Table 3.8. They show stable offset values, validating the method. The offset values effectively used were the average values, as the antenna assembly was not displaced between the six acquisitions.

TABLE 3.8
ESTIMATED HEADING AND PITCH OFFSETS

	Heading offset [°]	Pitch offset [°]
M1	0.9646	0.3891
M2	0.9171	0.4234
M3	0.9268	0.4104
M4	0.9208	0.4187
M5	0.9041	0.4133
M6	0.9342	0.3929
Average	0.9279	0.4080

3.6.3 Motion compensation-induced phase error correction

The motion compensation induced phase errors were compensated using a beam center approximation: for each pixel j, the approximation of the phase shift $\varphi_{\text{moco, j}}$ due to the roll angle applied in the motion compensation was subtracted and replaced by the approximation of the phase shift $\varphi_{\text{hgt-fine, j, k}}$ that should have been applied if the "accurate" pixel height had been used. The correction used an iterative process, where the "accurate" pixel height of iteration k was the InSAR-based height calculated in the previous iteration k-1. The iterations ended when the phase correction no longer varied (using a threshold criterion). The phase correction was performed using the following expression:

$$\begin{aligned}\varphi_{\text{correction, j, k}} &= \varphi_{\text{hgt-fine, j, k}} - \varphi_{\text{moco, j}} = \frac{2\pi p}{\lambda}\left(\Delta r_{\text{hgt-fine, j, k}} - \Delta r_{\text{moco, j}}\right) \\ &\cong \frac{2\pi p}{\lambda}\left[\left(\frac{\vec{r}_{\text{hgt-fine, j, k-1}} \cdot \vec{B}_{\text{real, j}}}{\left\|\vec{r}_{\text{hgt-fine, j, k-1}}\right\|} - \frac{\vec{r}_{\text{hgt-fine, j, k-1}} \cdot \vec{B}_{\text{lin, j}}}{\left\|\vec{r}_{\text{hgt-fine, j, k-1}}\right\|}\right)\right. \\ &\left. - \left(\frac{\vec{r}_{\text{SLC, j}} \cdot \vec{B}_{\text{real, j}}}{\left\|\vec{r}_{\text{SLC, j}}\right\|} - \frac{\vec{r}_{\text{SLC, j}} \cdot \vec{B}_{\text{lin, j}}}{\left\|\vec{r}_{\text{SLC, j}}\right\|}\right)\right]\end{aligned} \tag{3.13}$$

$\Delta r_{\text{hgt-fine, j, k}}$ and $\Delta r_{\text{moco, j}}$ are the range distance differences corresponding to the phase shifts $\varphi_{\text{hgt-fine, j, k}}$ and $\varphi_{\text{moco, j}}$. $\vec{B}_{\text{real, j}}$ is the real baseline corresponding to pixel j; its azimuth time position is calculated by mapping the antenna pointing (Section 3.3.2.1). $\vec{B}_{\text{lin, j}}$ is the baseline calculated from the linearized navigation data. $\vec{r}_{\text{SLC, j}}$ is the vector from the linearized sensor position to the Cartesian coordinates of the current pixel, calculated by geocoding the pixel using the same

DEM used in the motion compensation. $\vec{r}_{\text{hgt-fine, j, k-1}}$ is the vector from the linearized sensor position to the Cartesian coordinates of the pixel calculated from the InSAR data in the previous iteration k-1.

The roll variation in the 2011 acquisitions at Memmingen was minimal (the maximum variation was 1.1° in one of the acquisitions); only very small corrections were, therefore, applied, located mainly in forested and built-up areas, i.e., features above the DEM used in the motion compensation. Fig. 3.14 shows the roll angle variation and the altitude difference with and without the correction for acquisition M4.

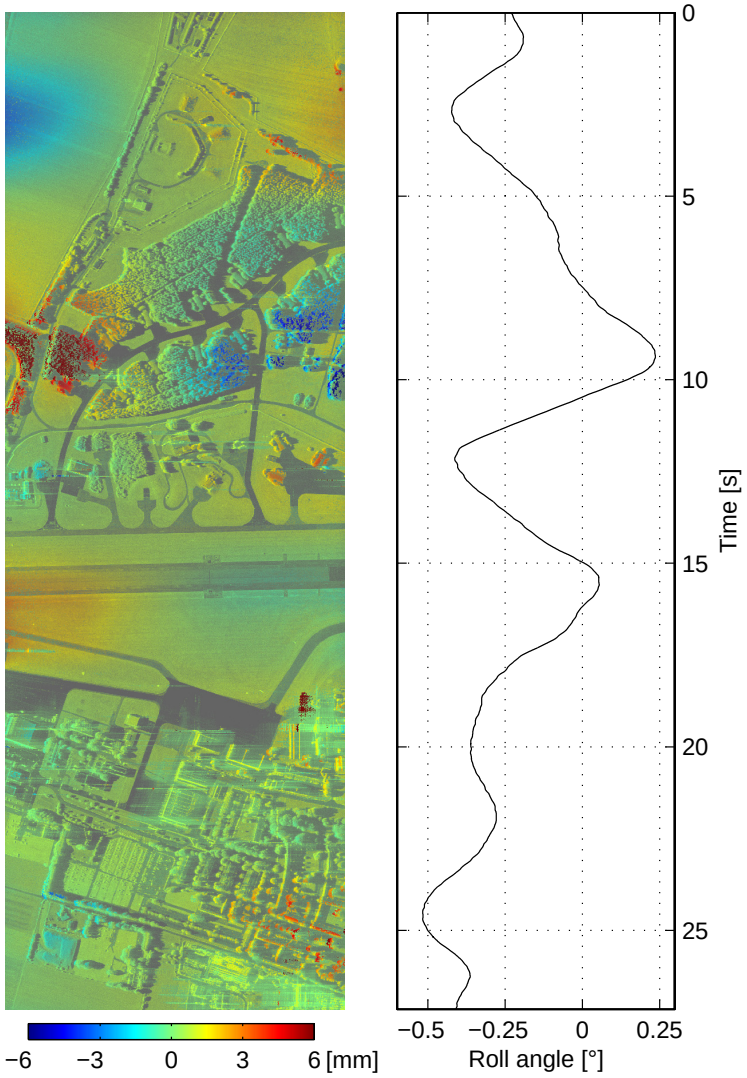

Fig. 3.14 Left: the effect of the correction of the motion compensation induced phase error on M4 height map. The height difference between the corrected and uncorrected data is overlaid here on the SAR amplitude image. Right: the roll angle is plotted vs. azimuth time.

4 SINGLE TREE IDENTIFICATION USING AIRBORNE MULTIBASELINE SAR INTERFEROMETRY DATA

This chapter has been submitted as: Magnard C., Morsdorf F., Small D., Stilla U., Schaepman M.E. & Meier E. (2016). Single tree identification using airborne multibaseline SAR interferometry data. *Remote Sensing of Environment*.

For clarity, the paper has been reformatted and the references are listed at the end of the thesis; otherwise, the contents are the same as in the submitted journal article.

Contributions of first author and co-authors: CM, US, MES, EM designed the study. CM, FM, DS developed the methodology. CM collected the data. CM performed the analysis. CM, FM, DS, US, MES, EM wrote the paper.

Abstract

Remote sensing data allow large scale observation of forested ecosystems. Forests assessment requires information about individual trees. Multibaseline SAR interferometry (InSAR) is able to generate dense point clouds of forest canopies, similar to airborne laser scanning (ALS). Such a point cloud was generated using data from the MEMPHIS system using millimeter wave. This point cloud was segmented using a normalized cuts technique to detect individual trees and derive their positions, heights, and crown diameters. To evaluate the InSAR point cloud properties and limitations, it was compared to products derived from ALS and stereo-photogrammetry. All point clouds showed similar geolocation accuracies with 0.2 – 0.3 m relative shifts. A much more limited penetration into the canopy was observed for both the Ka-band InSAR and photogrammetry-derived point clouds as compared to ALS. Canopy height models agreed very well with each other, with the InSAR height ~1 m lower than those derived from the other point clouds. The detected trees and their estimated physical and structural parameters were validated by comparing them to reference forestry data. A detection rate of ~90% was achieved for larger trees, corresponding to half of the reference trees. The smaller trees were detected with a success rate of ~50%. The tree height was slightly underestimated, with a R^2 value of 0.63. The estimated crown diameter agreed on an average sense, however with a relatively low R^2 value of 0.19. Very high success rates (> 90%) were obtained when matching the trees detected from the InSAR-data with those detected from the ALS- and photogrammetry-data. There, InSAR tree heights were in the mean 1–1.5 m lower, with high R^2 values ranging between 0.8 and 0.9. Our results demonstrate the use of millimeter wave SAR interferometry data as an alternative to ALS- and photogrammetry-based data for forest monitoring.

4.1 Introduction

The most obvious scale to assess forested ecosystems is that of the single tree level, hence many field inventories use information measured for individual trees (e.g. diameter at breast height, DBH). But field observations are costly and are thus limited to sampling designs, potentially misrepresenting important ecosystem properties (Duncanson et al., 2015). With high resolution remote sensing data becoming available, single tree detection in forests is receiving more attention. It was not until the development of airborne laser scanning (ALS) that 3D segmentation of single-trees became practical (Hyyppä et al., 2001). It is now a well-researched topic (Kaartinen et al., 2012), where forest parameters such as tree position, tree height, stem and crown diameter are estimated from segmented point clouds (Morsdorf et al., 2004; Reitberger et al., 2009). Airborne photogrammetry instruments are also able to provide very dense point clouds of forests, especially with the recent advent of UAVs (Puliti et al., 2015). In both ALS and stereophotogrammetry cases, the data collection is limited by weather conditions; photogrammetry requires abundant natural light and its results are considerably influenced by the seasonal leaf-off and leaf-on conditions; use of light UAVs is restricted by wind speed and autonomy. These factors strongly limit the time frames when these techniques can be employed. Interferometric SAR (InSAR) is less susceptible to weather conditions and can acquire data at night. Its sensitivity to leaf-off and leaf-on conditions is mitigated by the significant scattering occurring at the branches level (Karam et al., 1992). In addition, a successful airborne InSAR system for forest monitoring could lead to the design of a spaceborne equivalent system, with the advantages of worldwide coverage, larger swath widths, and potentially short revisit times.

SAR interferometry is a able to provide topography measurements (Rosen et al., 2000). InSAR data acquired with the shuttle radar topography mission (SRTM) provided a widely used SRTM digital elevation model (DEM) (Farr et al., 2007); higher resolution global DEM acquired by TerraSAR-X and TANDEM-X duo will soon become available (Krieger et al., 2007). Airborne SAR interferometry allows more flexibility in the choice of baselines, wavelengths, resolution, and illumination directions. Single pass interferometry using two or more receivers has the additional advantage of a constant baseline and avoids the issue of temporal decorrelation. Single pass interferometric systems that range from the very long P-band wavelength with its vegetation penetration (Hensley et al., 2001) down to surface scattering millimeter waves have been demonstrated (Magnard et al., 2014).

Forest observation and characteristics extraction is not a new application to SAR data (Le Toan et al., 1992). However, applications have until now typically consisted of parameter extraction at larger-than-single tree scales using (a) backscatter values for biomass estimation (Sandberg et al., 2011), (b) polarimetric InSAR for forest canopy height and biomass estimation (Mette et al., 2004) or (c) forest canopy height estimation through combination of X-band InSAR data with a terrain height reference calculated using a longer wavelength such as L-band or from an ALS terrain model (Balzter et al., 2007; Praks et al., 2012). Biomass estimation is typically achieved using allometric equations and model inversion; the forest canopy height obtained using X-band or longer wavelengths is not a direct measurement, but typically requires correction factors based on the forest and acquisition parameters (Praks et al., 2012).

Generating high density point clouds of forests, with the aim of extracting single trees, requires an InSAR sensor with appropriate properties: high range, azimuth and vertical resolution, sharp focusing under most wind conditions and predominant surface scattering. A Ka-band multibaseline InSAR sensor with short synthetic aperture such as the Millimeterwave Experimental Multifrequency Polarimetric High-resolution Interferometric System (MEMPHIS) (Schimpf et al., 2002) fulfills these requirements. Its azimuth beamwidth of ~3° and short range distance (typically between 1 km and 2 km) result in a short synthetic aperture of ~1 second, corresponding to a flight distance of ~80 m, which limits defocusing caused by tree movements due to wind. Its Ka-band wavelength enables high resolution in azimuth (0.082 m) despite the narrow beamwidth.

The 900 MHz bandwidth results in a range resolution of 0.165 m. This combination supports high vertical resolution with short baselines. The 8.5 mm wavelength ensures a limited penetration into the vegetation. Finally the multibaseline arrangement of the receiving antennas takes advantage of the simple phase unwrapping for the shortest baseline (0.055 m) with the lower sensitivity to phase noise from the longest baseline (0.275 m) (Rosen et al., 2000).

Consequently, as the technological requirements to generate high density point clouds using SAR interferometry are high, single tree detection based on the segmentation of those point clouds is a recent topic, it was first studied in (Schmitt et al., 2013) and further developed in (Schmitt et al., 2015), using data acquired with the MEMPHIS system. These two studies used a tomographic approach (Schmitt & Stilla, 2014b) to generate the point cloud, which was then segmented using a mean shift algorithm (Comaniciu & Meer, 2002). The validation was achieved using data acquired over sparsely planted broad-leaved trees in an urban park context.

We discuss the following questions: i) how does the point cloud of a temperate coniferous forest generated from multi-aspect, multibaseline InSAR data compare to equivalent products derived from full-waveform ALS data and stereo-photogrammetry, ii) how do tree parameters estimated from the segmented point cloud compare to reference forestry data and to tree parameters estimated from ALS and stereo-photogrammetry techniques and iii) what are the limitations of this technique?

4.2 System and data characteristics

4.2.1 Site characteristics and field data

The study was performed at *Vordemwald*, Aargau, Switzerland (47°16'27'' N, 7°53'14'' E). The area was selected due to the availability of a "Long term forest ecosystem research programme" (LWF) of the Swiss Federal Institute for Forest, Snow and Landscape Research (WSL) (Cherubini & Innes, 2000). The LWF plot spans ~300 m × 60 m (see Fig. 4.1). It covers a managed forest where conifers are predominant (80% of the 985 standing trees). Tree position, tree species, social status (on a scale ranging from 2 = dominant tree to 5 = understory tree), diameter at breast height (DBH) for each standing tree. In addition, tree heights were available for two subplots (~25% of the whole area), and crown diameters were available for most trees. The database is updated every 5 years; in our case the 2010 and 2015 updates were used. Since the InSAR data acquisitions took place in the middle of that period, therefore the DBH and tree height values were computed as the mean of the 2010 and 2015 measurements. In the following sections, these forestry data are referred to as "LWF" data.

The validation of the point cloud segmentation and forest parameters extraction in Section 4.4.2 requires a matching between extracted trees and trees from the reference LWF data. For this, a tree height is needed, which was only available for a small fraction of the trees (216 of 985 trees). An extrapolated tree height was therefore calculated for all 769 remaining standing trees using allometry (fitted polynomial), based on the DBH information ($R^2 = 0.724$, data not shown).

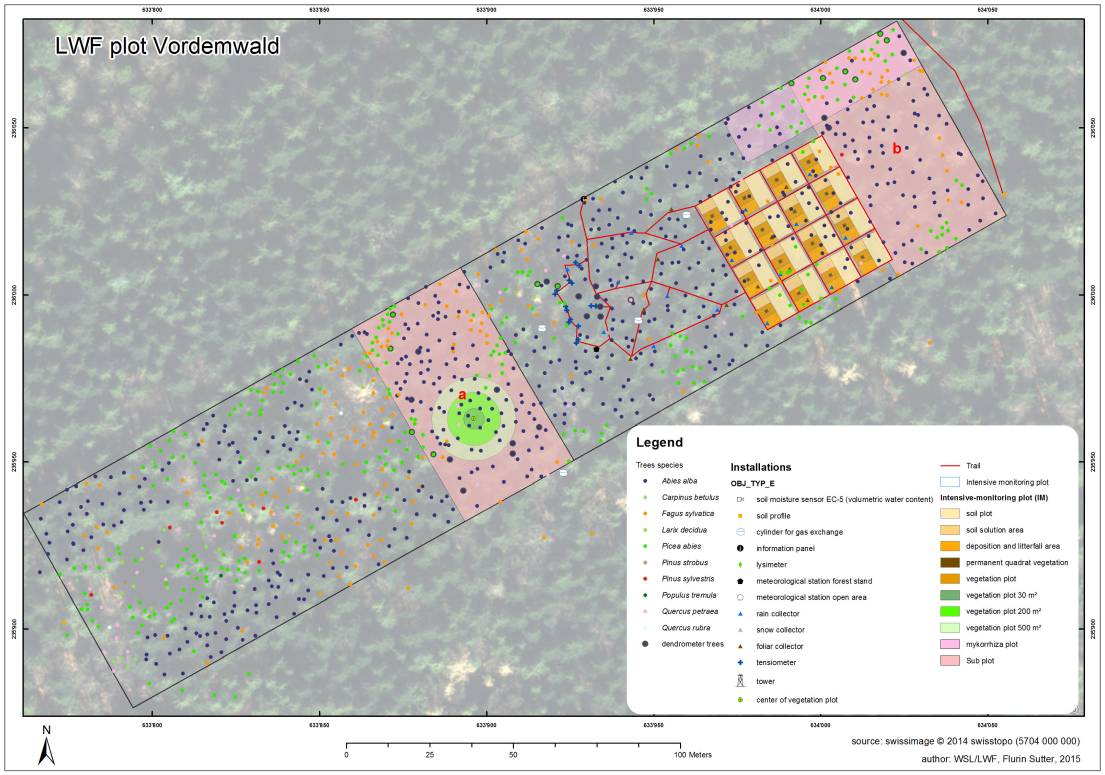

Fig. 4.1 Overview of the LWF area at Vordemwald, Aargau, Switzerland. Coordinate system: LV03 (CH1903). swissimage © 2014 swisstopo (5704 000 000).

4.2.2 InSAR system and data

The MEMPHIS system is an experimental SAR system developed and operated by Fraunhofer/FHR (Wachtberg, Germany), usually installed onboard a C-160 Transall aircraft (Schimpf et al., 2002). Table 4.1 summarizes the main system characteristics.

TABLE 4.1
MEMPHIS SAR SYSTEM PARAMETERS

Carrier frequencies	35 GHz (Ka-band) and 94 GHz (W-band)
Bandwidth	900 MHz (stepped-frequency)
PRF	1500 Hz
Typical airplane velocity	77 m/s
Airplane altitude	300 – 1000 m
Antenna tilt angle	20° – 35°
Theoretical rg. resolution	0.167 m
Theoretical az. resolution	0.082 m in Ka-band, 0.061 m in W-band

Data presented in this paper were acquired with the Ka-band multibaseline interferometric antennas. They use one transmit and 4 receive horns arranged vertically, enabling cross-track interferometry. The available baselines and corresponding ambiguity heights for the setup used during the experiment are shown in Table 4.2.

TABLE 4.2
AVAILABLE BASELINES AND CORRESPONDING TYPICAL AMBIGUITY HEIGHTS FOR THE KA-BAND ANTENNAS

Receiving Horns	Baseline [m]	Ambiguity Height [m] *
R_1, R_2	$B_1 = 0.055$	210.20
R_2, R_3 or R_3, R_4	$B_2 = 0.11$	105.10
R_1, R_3	$B_3 = 0.165$	70.07
R_2, R_4	$B_4 = 0.22$	52.55
R_1, R_4	$B_5 = 0.275$	42.04

* At mid-range (1547 m), sensor altitude: 750 m, antenna tilt angle: 30°

The SAR system was complemented by a differential GPS (DGPS) system operating at 20 Hz and an inertial measurement unit (IMU) operating at 500 Hz. A three-axis accelerometer was installed directly on the SAR antenna assembly. Additional detailed system characteristics can be found in (Magnard et al., 2014).

The InSAR data were acquired November 8, 2012, and consist of 8 datasets collected along 4 flight lines, i.e. each flight line was repeated twice for higher point density and as potential backup in case of a failed acquisition. The area could only be illuminated from the South and East directions due to flight safety reasons. The characteristics of the acquisitions are summarized in Table 4.3; Fig. 4.2 shows an overview of the aggregated point cloud generated using methods described later in Section 4.3.1. The area later investigated in Section 4.4.1 for point cloud characterization is represented in green; the LWF test site is depicted in gray. Four corner reflectors were placed in grasslands around the test area, so that at least one reflector was illuminated in each data take. Their positions were measured using DGPS to ensure an accurate geometry as well as to calibrate the phase-to-height calculation. The acquisitions took place at a transition time, with deciduous trees at various states of their autumn foliage, from green to yellow to red leaves, and with some of them having already lost their leaves.

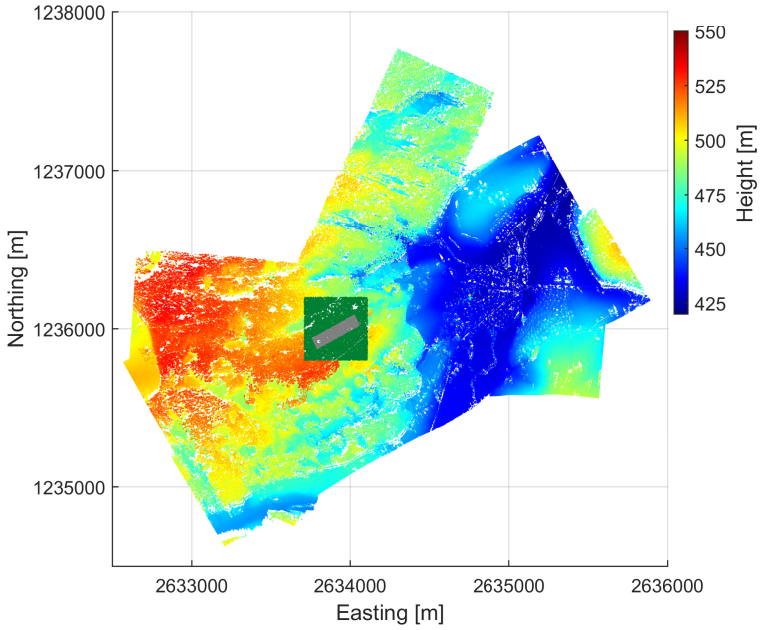

Fig. 4.2 Overview of the InSAR point cloud at Vordemwald, Aargau, Switzerland. It was generated using the method described in Section 4.3.1. The green square shows the area investigated in Section 4.4.1. The gray area marks the location of the LWF reference information. Coordinate system: LV95 (CH1903+).

TABLE 4.3
VORDEMWALD ACQUISITION CHARACTERISTICS

Acquisition number	1/2	3/4	5/6	7/8
Mean sensor altitude* [m]		750		
Near range distance [m]		1250		
Range swath width [m]		600		
Acquisition length [km]	3.03/2.77	2.85/3.01	2.96/3.12	3.13/2.06
Heading [°]	95	60	25	60
Illumination direction [°]	5	330	295	330

*above mean test site terrain height

4.2.3 ALS data

Full waveform ALS data were acquired in 2014 covering the whole canton of Aargau (Leiterer et al., 2015). Both leaf-off (March/April, 2014) and leaf-on (June/July, 2014) data were collected, using a *Riegl* LMS-Q680i scanner. Flight altitudes of 600 and 700 m above average terrain height were used in spring and summer respectively, resulting in 0.3 and 0.35 m footprints. Point densities of 21.7 and 19.3 pts/m^2 were measured for the leaf-off and leaf-on cases, respectively.

4.2.4 UAV-based stereo-photogrammetry data

Finally, stereo-photogrammetry data were acquired in 2015 using the *senseFly eBee* UAV (senseFly, 2014), again in both leaf-off (March 18, 2015) and leaf-on (August 26, 2015) conditions. High resolution point clouds (50 and 39.5 pts/m^2) and orthophotos were generated from these data. Four signalized ground control points were deployed in the test area. Their positions were measured using DGPS, to achieve accurate point cloud coordinates. In the following, we refer to these data as "photogrammetric" data for simplification.

4.3 Methods

4.3.1 SAR data processing

4.3.1.1 Focusing SAR data

The interferometric SAR data were processed starting from raw data, resulting in single look complex (SLC) images (Magnard et al., 2014). Fig. 4.3 summarizes the focusing process.

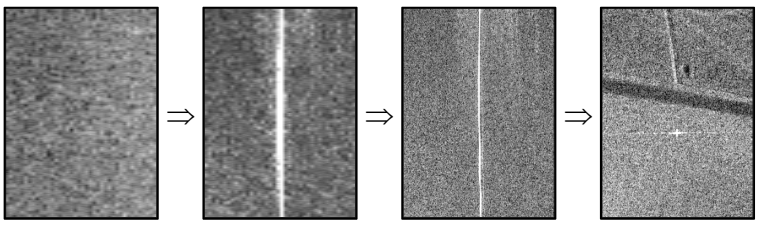

Fig. 4.3 Main steps of the SAR data focusing process: (a) range compression of individual radar pulses, (b) stepped-frequency processing, (c) azimuth compression. The illustrations are amplitude images and show a corner reflector and its surroundings. The horizontal and vertical axes correspond to range and azimuth directions, respectively.

The data focusing started with the raw data preparation / calibration, which includes (1) integration of DGPS and IMU data, (2) measurement of the antenna tilt angle by combining the accelerometer and IMU data, (3) preparation of a coarse DEM, typically consisting of the selection of the appropriate area in the SRTM DEM, and smoothing it with an average filter. The raw data consisted of 4 channels corresponding to each receiving antenna; for each channel, 8 x 200 MHz

chirps were sampled with 100 MHz offsets between the carrier frequencies of each chirp (i.e. with 50% overlapping frequencies).

The individual, 200 MHz, raw data pulses were range compressed using a conventional matched filtering technique (Fig. 4.3a) (Levanon & Mozeson, 2004). Chirp replica measured at the beginning of each flight campaign are used for the range compression.

The stepped-frequency processing based on (Lord, 2000) combined the 8 sets of 200 MHz range compressed data sets into a single 900 MHz range compressed image (Fig. 4.3b).

The azimuth focusing (Fig. 4.3c) was achieved using the Extended Omega-K algorithm (Reigber et al., 2006). It includes range and topography-dependent motion compensation using beam-center approximation. The beam-center approximation was valid due to MEMPHIS's narrow beam width. Radiometric corrections using antenna patterns were included within the azimuth focusing. It resulted in 4 SLC images in zero-Doppler geometry, i.e. as if the data had been acquired along a perfectly straight flight path, with a radar beam exactly perpendicular to the flight direction.

4.3.1.2 Point cloud generation

The interferometric processing was achieved using the methods described in (Magnard et al., 2014; Magnard et al., 2016a) and is summarized in Fig. 4.4. It used an iterative process: phase corrections needed to be applied relative to the beam elevation, using antenna phase patterns; accurate beam elevations at each range – azimuth position required an antenna pointing estimation depending on the sensor position and attitude as well as the 3D coordinates of the backscattering element. These coordinates can be estimated using an external DEM as approximation, however an accurate correction requires more precision. The previously calculated coordinates were thus iteratively used for improved beam elevation-dependent phase correction.

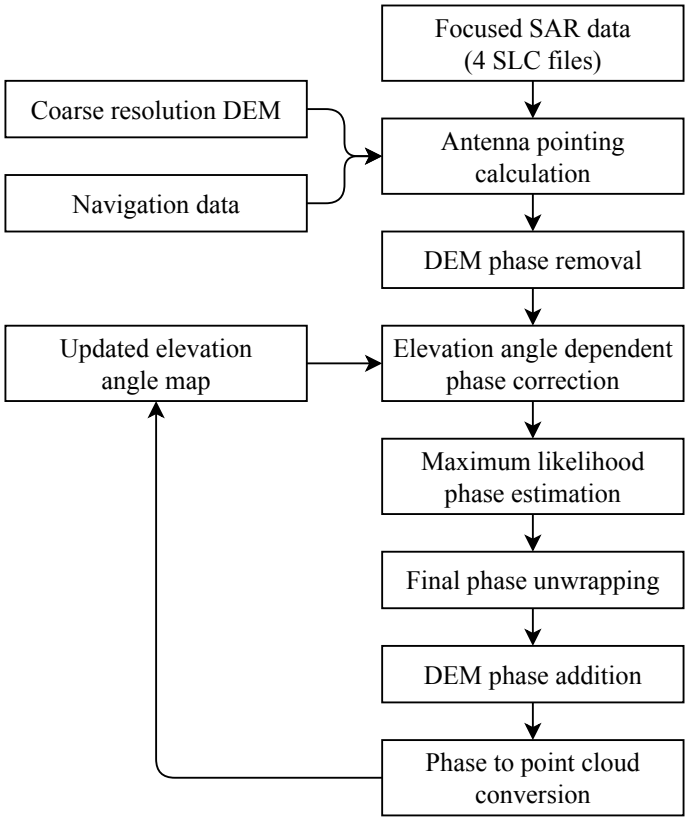

Fig. 4.4 Block diagram of the interferometric processing chain.

1) The interferometric processing started with the antenna pointing estimation, based on a coarse external DEM and the navigation data, resulting in an estimate of the Cartesian coordinates and the elevation relative to the antenna beam for each range – azimuth pixel.
2) Using the antenna pointing information, the interferometric phase related to the coarse external DEM/sensor attitude was removed from the slave SLCs. This step replaced the well-known flat Earth removal with the advantage of reduced wrapping in regions with large topography variations.
3) The beam elevation angle-dependent phase correction was carried out. An elevation angle map was estimated first for each range – azimuth cell, using the antenna pointing information. In the next iteration(s), the elevation angle map was updated based on results from the previous iteration. The phase correction was carried out based on antenna phase patterns.
4) The maximum likelihood (ML) phase estimation was achieved. Based on (Lombardo & Lombardini, 1997), it used the four coregistered SLCs simultaneously to compute partially unwrapped interferometric phase values.
5) For the MEMPHIS system, the resulting ambiguity height was the same as that of the shortest baseline (0.055 m). If necessary, a final phase unwrapping step was performed using the SNAPHU algorithm (Chen, 2001).
6) The final step was the conversion from phase values to 3D coordinates. The phase subtracted in step 2) was added back to the interferogram. Using at least one tie point, the relative phase values of the interferogram were converted into absolute phase values. The range vector was then calculated using the range distance equation, baseline vector, and absolute phase value. The ground position was finally determined combining the linearized sensor position with the calculated range vector, and the result transformed back to the user-defined coordinate system (typically local map coordinates). When several acquisitions were available, the point clouds generated from each acquisition could be aggregated to increase the point density.

4.3.1.3 Point cloud filtering

In the absence of offsets, the vertical accuracy of an InSAR point cloud is determined by the phase noise. It can be estimated from the number of looks used and the measured coherence, using either the Cramer-Rao bound (Rodriguez & Martin, 1992) or the experimental measurements presented in (Magnard et al., 2016a). Alternatively, the number of looks and a coherence threshold can be defined from the desired vertical accuracy. We used 3 range and 12 azimuth looks, corresponding to 0.5 × 0.62 m cells; the coherence threshold was set at $\gamma = 0.75$. The coherence value was estimated for each point within the ML estimation for the longest available baseline (0.275 m). The corresponding height standard deviation calculated using the Cramer-Rao bound was $\sigma_h(\gamma = 0.75) \cong 0.7$ m at mid-range. Coherence values lower than this threshold corresponded mainly to shadowed regions and areas dominated by forward scattering.

4.3.2 Forest segmentation

The point cloud was first prepared by subtracting the terrain elevation from the height of each point. The terrain elevation of each point was interpolated from a reference DTM. In addition, since the purpose of the whole process was to detect trees, points below 3 m height were discarded.

An automatic, unsupervised forest segmentation method was developed. First, seed locations for the trees were determined by detecting local maxima in a point density map. In a second step, the point cloud was segmented using the normalized cuts method (Shi & Malik, 2000). From the resulting point clusters, the tree positions, heights and crown diameters were estimated.

4.3.2.1 Determining seeds

A common technique for detecting single trees in point clouds is to build a canopy height model and find the local maxima, with the assumption that these represent the tree tops (Hyyppä et al., 2001; Morsdorf et al., 2004). With interferometric SAR data, we have additional information provided by the coherence (see Section 4.3.1.3). In the case of forest acquisitions, points from trustworthy scatterers (with high coherence) are inherently mapped at tree locations. Applying a threshold based on the coherence values results in a high point density at tree positions and very low point density between the trees.

The following process was developed for determining a first estimation of tree positions (seeds):

1) A canopy height model (CHM) and a point density map were simultaneously generated as follows: (a) A regular grid was generated in map coordinates, covering the point cloud area (Fig. 4.5, left). (b) For each pixel of the grid, we calculated the horizontal distance between the pixel center coordinates and the points of the point clouds. Points inside a user defined radius (e.g. 1 m) were kept (Fig. 4.5, right). The vertical distribution of the selected points was checked; outliers outside ±3 standard deviations around the mean height were discarded. (c) The number of remaining points was divided by the search area to provide a point density estimation. The maximum height was kept as the pixel height used when generating the CHM.

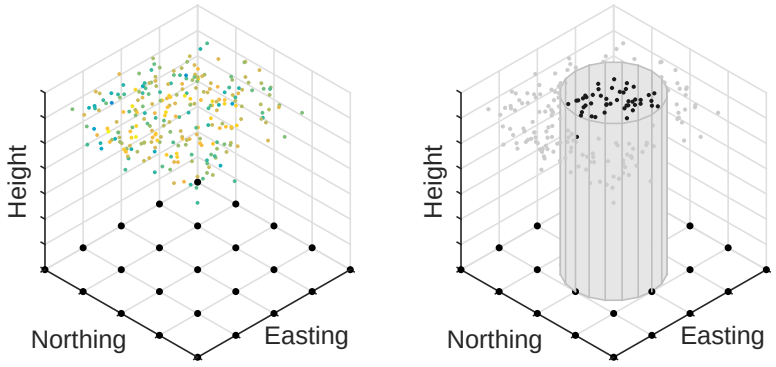

Fig. 4.5 Left: Regular grid (black dots) covering the point cloud area. Right: Points selected to calculate the canopy height and point density at one grid position.

2) A local maxima detection was applied to the generated point density map. This differed from typical ALS-data based single tree detection where local maxima detection are generally calculated on the basis of the CHM. The point density map was smoothed using a low pass Gaussian filter with the σ parameter set to 0.6 m to remove details much smaller than tree crowns. The local maxima were then searched by looking at each grid point neighborhood: if all 8-connected grid points had a lower or equal associated *point cloud density*, the current grid point was considered to be a local maximum. A minimum point cloud density threshold was used to avoid spurious tree detection.

The coordinates of the local maxima were used in the second step of the forest segmentation as one of the parameters of the similarity matrix; the number of local maxima set the number of clusters / trees to be segmented using the normalized cuts method.

4.3.2.2 Normalized cuts

The normalized cut method (Shi & Malik, 2000) segments a set of points based on a weighted graph representation of the points. Contrary to the segmentation method finding the minimum cut, which tends to favor partitioning of isolated points, the normalized cut method also introduces the total connection from a defined node (a point in our case) to all nodes in the graph. Hence,

both the dissimilarity between different groups and the similarity within groups are measured, allowing one to avoid a bias toward segmenting isolated points.

The segmentation was achieved by solving the following generalized eigenvalue problem:

$$(\mathbf{D} - \mathbf{W})y = \lambda \mathbf{D} y \tag{4.1}$$

where the $n \times n$ weighting matrix $\mathbf{W}$ represents the weights $w(i,j)$ between all n nodes of the graph G and is inherently symmetric and positive semi-definite. The $n \times n$ degree diagonal matrix $\mathbf{D}$ contains on its diagonal elements $d(i,i)$ the total connections of node i to all other nodes:

$$d(i,i) = \sum_j w(i,j) \tag{4.2}$$

The derivation of the generalized eigenvalue problem in (4.1) and how to solve it are fully described in (Shi & Malik, 2000). As in (Reitberger et al., 2009), the important point here is that the weighting matrix $\mathbf{W}$ should be well adapted to our objective and to the data properties. Any measurable data parameter can be used as a criterion for the data segmentation using normalized cuts. In our case, as we want to detect trees from a point cloud acquired over a forest, the horizontal and vertical point positions are important criteria. The first estimation carried out in the previous section determined the number of trees and estimated their positions. The horizontal distance between each point and these first estimations of the tree positions can therefore be used as a constraining parameter. The coherence tends to be very high in the center of point clusters, and lower where the point density is lower. This would imply that the coherence is higher close to the tree stem position than at the edges of the crown. Using this information in the weighting matrix would intensify the link between points close to the tree stems while allowing more freedom to the points at cluster edges.

To account for the parameters described above, the weights were defined as follows:

$$w(i,j) = e^{-X(i,j)} \cdot e^{-Z(i,j)} \cdot e^{-C(i,j)} \cdot e^{-G(i,j)} \tag{4.3}$$

with

$$X(i,j) = \left(\frac{D_{ij}^{XY}}{\sigma_{xy}}\right)^2, Z(i,j) = \left(\frac{D_{ij}^{Z}}{\sigma_z}\right)^2,$$
$$C(i,j) = \left(\frac{1 - \gamma_{ij}^{\min}}{\sigma_\gamma}\right)^2, G(i,j) = \left(\frac{G_{ij}^{\max}}{\sigma_G}\right)^2 \tag{4.4}$$

D_{ij}^{XY} is the horizontal distance between points i and j, D_{ij}^{Z} is the vertical distance between those points, $\gamma_{ij}^{\min}$ is the minimum of both coherence values attached to points i and j, $G_{ij}^{\max}$ is the maximum of both horizontal distances to a selected tree seed for points i and j. The selected tree seed is the closest tree seed to point i.

The σ_{xy}, σ_z, σ_γ and σ_G parameters control the sensitivity of the four terms of (4.3). The higher they are, the slower the loss of similarity for an increasing numerator value in (4.4). Both the coherence and distance to tree seed terms were employed as options.

The following empirical values were set: $\sigma_{xy} = 1.25$ m, $\sigma_z = 5$ m, $\sigma_\gamma = 0.15$ and $\sigma_G = 4$ m. A larger value had to be employed for the vertical distance compared to the horizontal distance to account for tree shapes in the InSAR point cloud. Scaling of the z-axis or its separate treatment are common procedures used to facilitate ALS-based tree segmentation (Morsdorf et al., 2004; Reitberger et al., 2009). The combined weights $w(i,j)$ were set to 0 if they were lower than 10^{-6}, to reduce the computational load (see Appendix 4.6.1). Taking the parameters one by one, this

would correspond to cut off values of $D_{ij}^{XY} = 4.65$ m, $D_{ij}^{Z} = 18.58$ m, $\gamma_{ij}^{\min} = 0.44$ and $G_{ij}^{\max} = 14.87$ m.

4.3.2.3 Forest parameters

The following forest parameters were estimated from the segmented point cloud: tree position, tree height, and crown diameter. Outliers could produce bias in the calculated parameters. To reduce the probability of such an outcome, for each detected tree, we discarded points (a) further than 20 m from the cluster centroid in the horizontal direction, (b) further than the 99th percentile horizontal distance to the cluster centroid, and (c) higher than the 99th percentile height. The cluster centroid was then recalculated.

The tree horizontal position was then defined as the horizontal position of the cluster centroid. The tree height was set to the highest point of the cluster. For the crown diameter δ, the 2D horizontal convex hull area S was calculated. The diameter was estimated as if the crown had a circular shape (Morsdorf et al., 2004):

$$\delta = 2\sqrt{\frac{S}{\pi}} \tag{4.5}$$

4.4 Results

4.4.1 Point cloud characterization

In the case of measurements acquired in a forest, we do not have a smooth surface but scatterings at various vegetation levels, which gives rise to the question: what are we really measuring? To better comprehend the nature of the InSAR forest point cloud, we compare it to point clouds generated from ALS and photogrammetric data.

A 400×400 m area encompassing the LWF test site (see Fig. 4.2) was chosen for this analysis. The InSAR point cloud is shown in Fig. 4.6. The measured point density for the area was 17.8 pts/m^2 and 7.9 pts/m^2 before and after applying the coherence threshold, respectively. Note that the resulting point density was not homogeneous: it was highest in areas that appear to correspond to actual trees, while the areas between the trees or in clearings were emptied out.

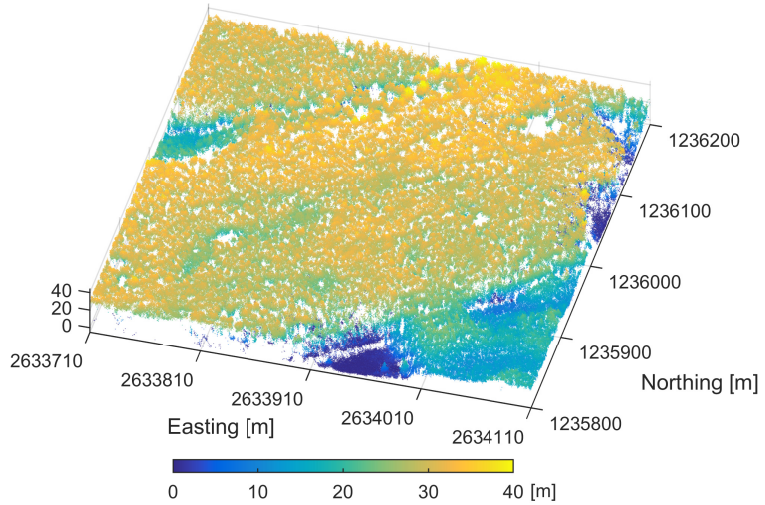

Fig. 4.6 InSAR-based point cloud of the selected 400x400 m area. Coordinate system: LV95 (CH1903+).

In order to perform a first comparison, profiles from three point clouds are plotted in Fig. 4.7. Profiles from InSAR- (in red), ALS- (leaf-off, in blue) and photogrammetry-based (leaf-off, in green) point clouds are shown. The InSAR profiles show that most of the scattering occurs in the

upper layers of the forest, except at the edges of clearings such as on the right side of the profile on top. ALS-based data show the forest structure down to the ground, photogrammetry-based data typically show the forest canopy. Directionality effects due to the radar illumination directions are clearly visible: they result in "holes" for shadowed areas. As a consequence, South or East sides of trees show higher point densities than their North and West sides.

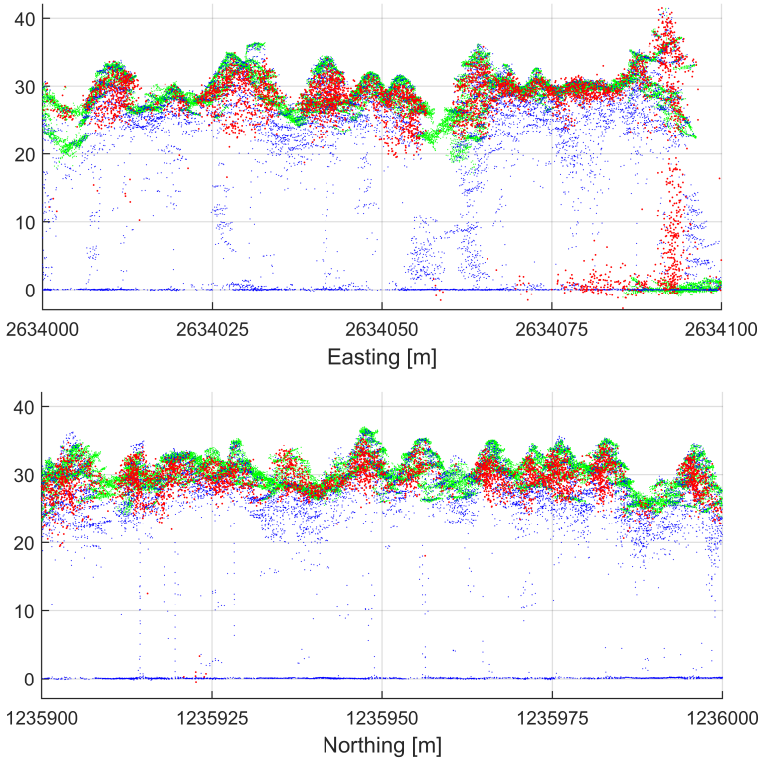

Fig. 4.7 Point cloud profiles from InSAR data (red), ALS data (leaf-off, blue) and eBee data (leaf-off, green). Top: 100 m profiles in East-West direction (Northing coordinates: 1236040-1236045). Bottom: 100 m profiles in North-South direction (Easting coordinates: 2633900-2633905). Coordinate system: LV95 (CH1903+).

In a next step, CHMs generated from the various point clouds were compared. A regular grid with 0.5 m spacing was generated; for each point, a 1 m search radius was used. The same parameters were used for the creation of all CHMs, to avoid introducing processing biases. For each coordinate of the CHMs, the height from the various data sources was compared in scatter plots, as shown in Fig. 4.8. Table 4.4 summarizes the regression results of the InSAR CHM w.r.t. the corresponding ALS- and photogrammetry-based results. Values below 3 m are shown in Fig. 4.8 but were discarded for the regression calculation and R^2 analysis to avoid risking a comparison of the terrain height with the vegetation height. The proportion of empty cells and cells below 3 m is also given in Table 4.4. Table 4.5 reports the mean, median and standard deviation of the height difference $H_{InSAR} - H_{reference}$ between the InSAR CHM and the ALS- and photogrammetry-based reference CHMs.

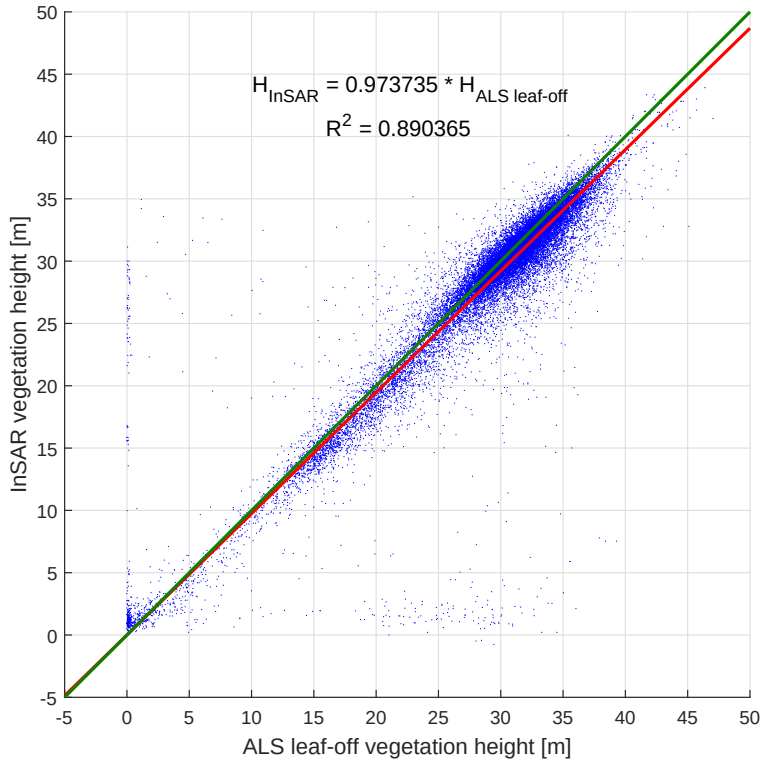

Fig. 4.8 Scatter plot of the InSAR CHM vs. the ALS (leaf-off) CHM. The green line is the identity line, the red line is the regression line.

TABLE 4.4
CHM PROPERTIES AND REGRESSION ANALYSIS

Reference (X axis)	Acquisition date	Regression slope *	R^2 *	Empty cells [%]	Cells < 3 m [%]
InSAR	08.11.2012	---	---	16.021	1.780
ALS leaf off	03-04.2014	0.974	0.890	0.016	3.545
ALS leaf on	06-07.2014	0.965	0.887	0.023	2.905
Photogrammetry leaf off	14.03.2015	0.961	0.867	0.003	4.743
Photogrammetry leaf on	26.08.2015	0.954	0.843	0.700	3.236

* InSAR CHM height values in the Y-axis

TABLE 4.5
HEIGHT DIFFERENCE $H_{INSAR} - H_{REFERENCE}$

Reference	Mean [m]	Median [m]	Std. dev. [m]
ALS leaf off	-0.748	-0.567	1.921
ALS leaf on	-1.044	-0.873	1.941
Photogrammetry leaf off	-1.104	-1.007	2.129
Photogrammetry leaf on	-1.348	-1.282	2.308

The relative geolocation accuracy was verified by computing the maximum of the cross-correlation between the InSAR CHM and the ALS- and photogrammetry-based CHMs; it was measured with a sub-pixel accuracy (Guizar-Sicairos et al., 2008). To avoid issues with empty cells, the CHMs were filled using code developed by (D'Errico, 2004). For the 400×400 m area, the InSAR CHM showed deviations w.r.t. ALS- and photogrammetry-based CHMs of 0.09 and 0.14 m to the East and 0.21 to 0.3 m to the South. Splitting the area into four 200×200 m quadrants

resulted in similar values, with a slightly larger shift (0.7 m) in one quadrant of the photogrammetric leaf-on data, where no signalized ground control points were available in the neighborhood.

4.4.2 Forest segmentation

Fig. 4.9 shows the point density map and the detected local maxima that were used as an initialization step for segmentation. Fig. 4.10 shows the color coded segmented point cloud.

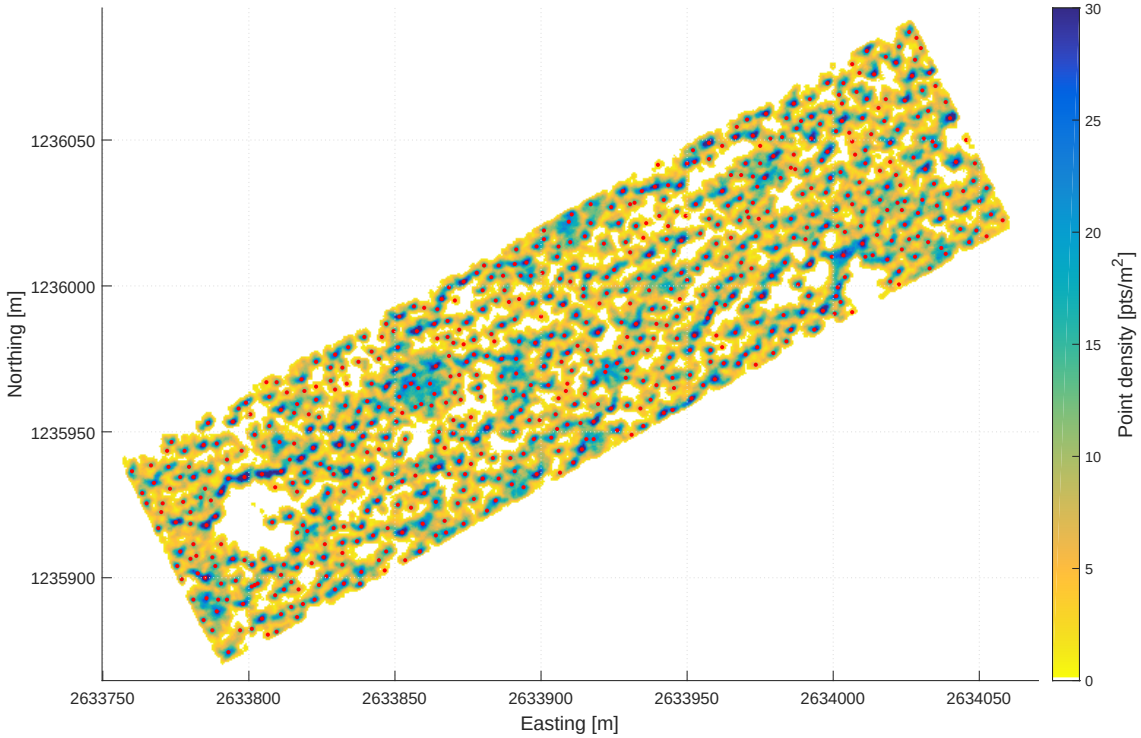

Fig. 4.9 Point density map of the thresholded InSAR point cloud for the LWF area. Detected local maxima are marked as red dots. Coordinate system: LV95 (CH1903+).

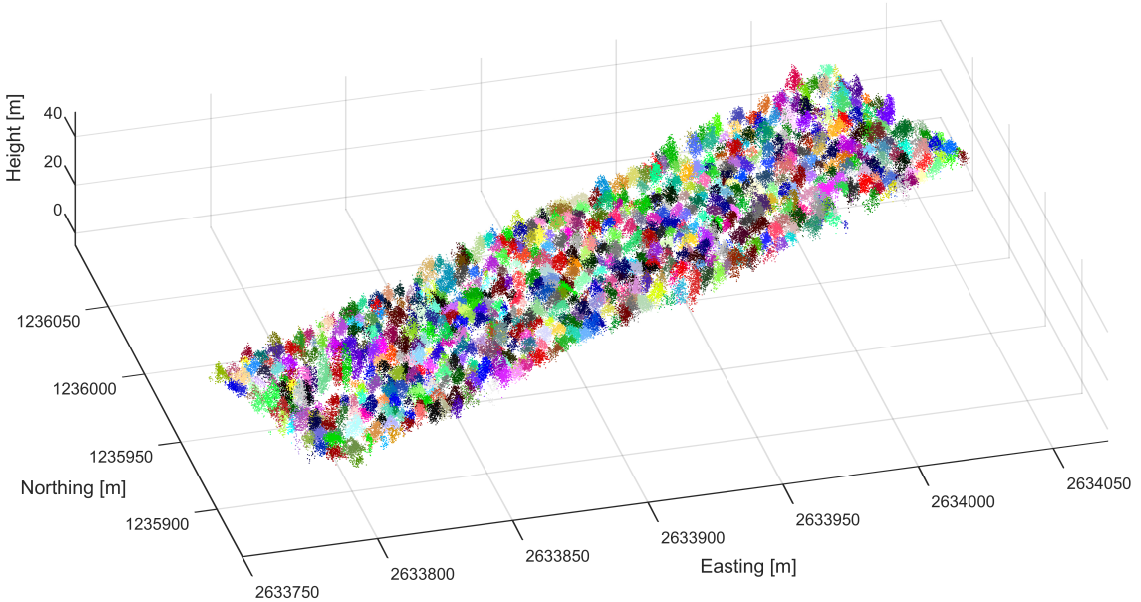

Fig. 4.10 Result of the point cloud segmentation. Coordinate system: LV95 (CH1903+).

Tree parameters were derived from the point clusters as described in Section 4.3.2.3. The detected trees ("InSAR trees") were then matched to the trees from the LWF forestry data. To fulfill this, the LWF data required a filtering: the understory trees and the trees with thin stems were discarded. This was mandatory, as the millimeter waves typically do not reach the lower levels of a forest, and keeping the very young, thin trees would most likely distort the results by producing false positives. Thus, understory trees (social status = 5) and trees with a DBH $\leq$ 0.2 m were discarded, leaving 745 out of the original 985 standing trees.

The InSAR trees were matched to those from the LWF database as follows: (a) Only InSAR/LWF tree pairs closer than 3 m horizontally from each other were considered. This process removed three reference trees. (b) Matching was achieved by searching for the minimum sum of the squared distances between the tree pairs. To account for the assumed lower accuracy of LWF tree *heights* compared to their positions, a weighting factor of 1/3 was applied to the height information. Only unique matches were accepted. (c) Trees matched with a distance larger than 3 m between each other were rejected.

The common area left 742 reference trees to be matched with 544 InSAR trees; 537 of those trees could be matched, corresponding to a detection ratio of 0.724. Fig. 4.11 shows the result of the tree matching process.

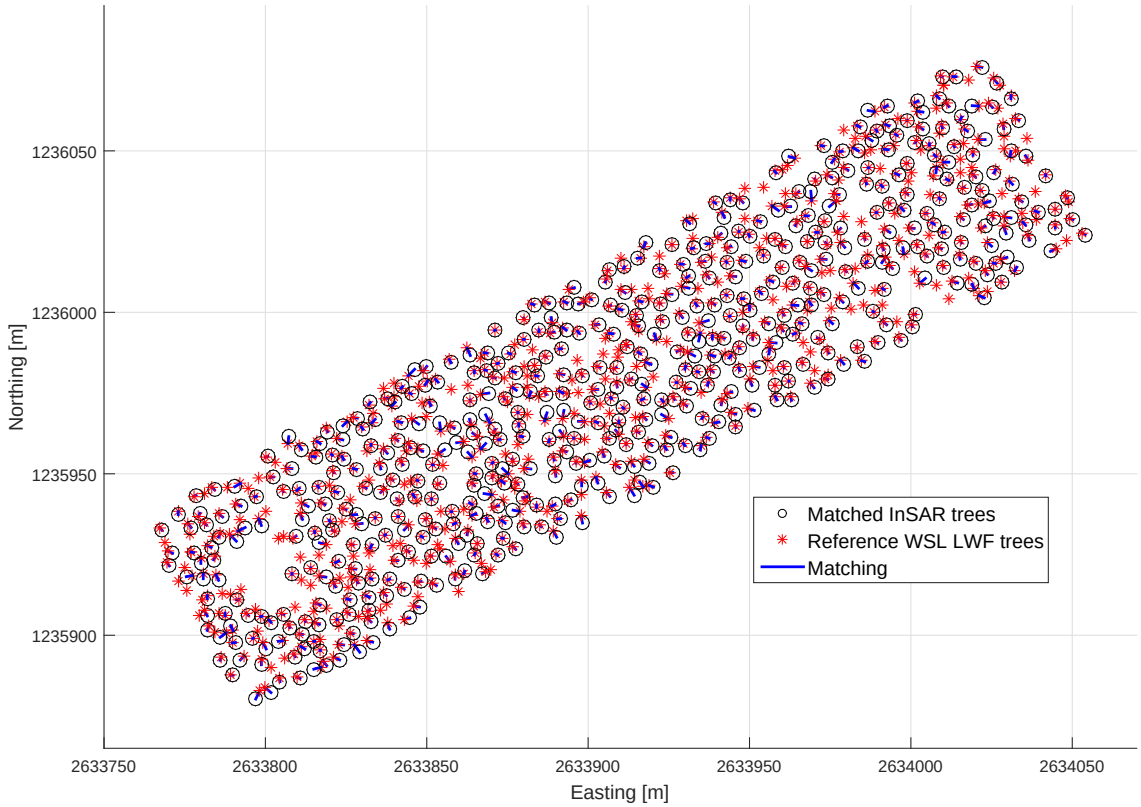

Fig. 4.11 Matching results between InSAR trees and LWF trees. Coordinate system: LV95 (CH1903+).

The detection rate was analyzed relative to tree characteristics: social status, conifer/broadleaved, and DBH. The results are summarized in Table 4.6; Fig. 4.12 shows the detected trees and success ratio with respect to tree DBH classes. Successful detection was clearly linked to the tree size: dominant trees, trees with a DBH larger than 0.39 m were detected in 91.5% of the cases, while thin (and young / low) trees were rarely detected.

Plotting the detection rate versus the tree *height* results in a figure very similar to that using the DBH: the higher the tree, the more reliable its detection. 90.3% of the 393 trees higher than 32 m were detected, while the success rate was 52.2% for the 349 trees below 32 m.

Conifers were detected with a slightly higher success rate than broad-leaved trees. Since the number of detected broad-leaved trees was rather small at 63, this difference is not conclusive. It can be noted that conifers were also larger on average (including extrapolated heights): 33.19 ± 2.65 m and 30.50 ± 3.55 m for conifers and broad-leaved trees, respectively.

TABLE 4.6
DETECTION RATES VS. TREE CATEGORIES

Category	# Trees	# Detected trees	Detection rate
All trees	742	537	0.724
Social status = 2	92	85	0.924
Social status = 3	489	387	0.791
Social status = 4	160	64	0.400
Conifers	644	474	0.736
Broad-leaved trees	98	63	0.643
DBH = [0.21, 0.27[	142	48	0.338
DBH = [0.27, 0.33[	112	60	0.536
DBH = [0.33, 0.39[	97	72	0.742
DBH = [0.39, 0.45[	73	64	0.877
DBH = [0.45, 0.51[	102	95	0.931
DBH = [0.51, 0.57[	73	68	0.932
DBH = [0.57, 0.63[	64	57	0.891
DBH = [0.63, 0.69[	46	43	0.935
DBH = [0.69, 0.75[	22	21	0.955
DBH > 0.75	9	8	0.889

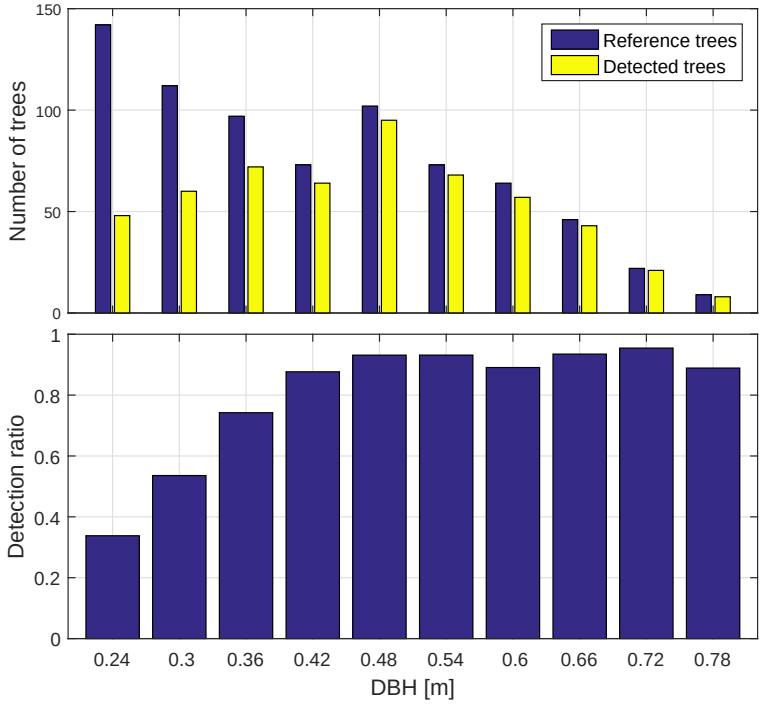

Fig. 4.12 Detected trees and success ratio with respect to tree DBH classes.

The localization, height and crown diameter calculated from the InSAR data were compared to corresponding measurements from the reference data. Only the effectively measured tree heights were used (the trees whose height had been extrapolated from the DBH were discarded). A statistical analysis of the differences between the estimated tree parameters and reference values from the LWF data is reported in Table 4.7. The Easting and Northing localization differences indicate a South-East shift of the InSAR trees. The mean tree height difference of -1.608 m shows that InSAR tree heights were noticeably lower than the value from the corresponding LWF trees. The scatter plot in Fig. 4.13 and its regression line with a slope $m_h = 0.949$ confirm the lower tree height estimation. The relatively high R^2 value of 0.627 supports the hypothesis of an accurate tree detection. The mean crown diameter difference is very close to 0; however, the scatter plot in Fig. 4.14 indicates overestimation of the lower crown diameters and underestimation of the larger ones. The slope of the regression line is $m_d = 0.923$, with a relatively low R^2 value of 0.189.

Table 4.7 also reports the estimated tree parameters for the conifers and broad-leaved trees categories. The localization of conifers has a considerably lower standard deviation, indicating more reliable detection of conifers than broad-leaved trees. The height estimation cannot be compared since only 7 detected broad-leaved trees had effectively measured heights (not extrapolated). The crown diameter was on average accurately estimated for conifers; it was slightly underestimated for broad-leaved trees, with a markedly larger standard deviation.

TABLE 4.7
ESTIMATED TREE PARAMETERS VS. LWF DATA

	Difference (InSAR - LWF)	Mean [m]	Standard deviation [m]	Samples
All detected trees	Height	-1.608	1.909	127
	Crown diameter	0.008	1.714	520
	Easting localization	0.526	0.853	537
	Northing localization	-0.337	0.824	537
Conifers	Height	-1.508	1.875	120
	Crown diameter	0.070	1.532	459
	Easting localization	0.637	0.725	474
	Northing localization	-0.414	0.742	474
Broad-leaved trees	Height	-3.321	1.797	7
	Crown diameter	-0.466	2.689	61
	Easting localization	-0.310	1.218	63
	Northing localization	0.241	1.134	63

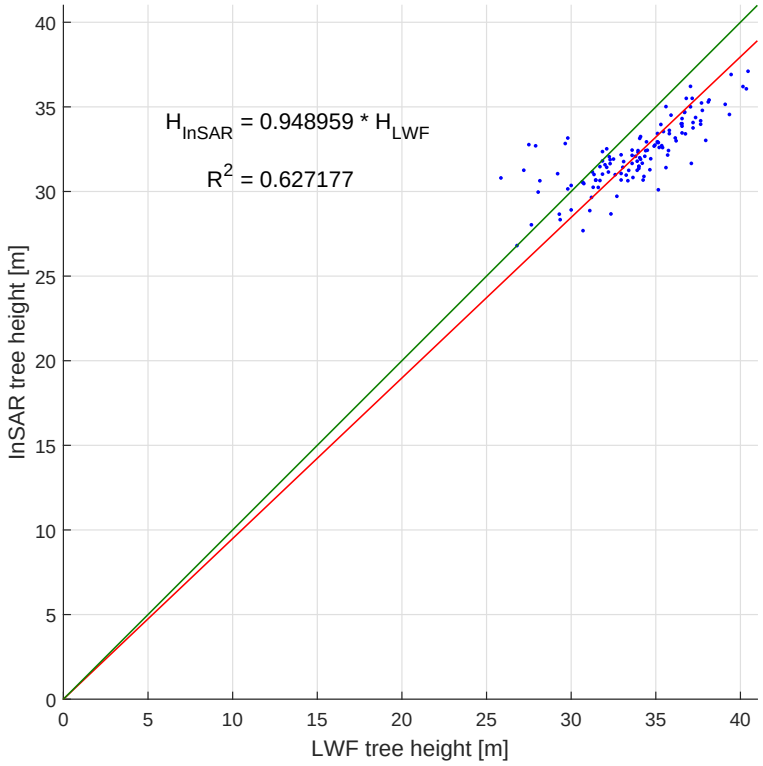

Fig. 4.13 Scatter plot of the InSAR tree heights vs. the height of the corresponding (matched) LWF trees.

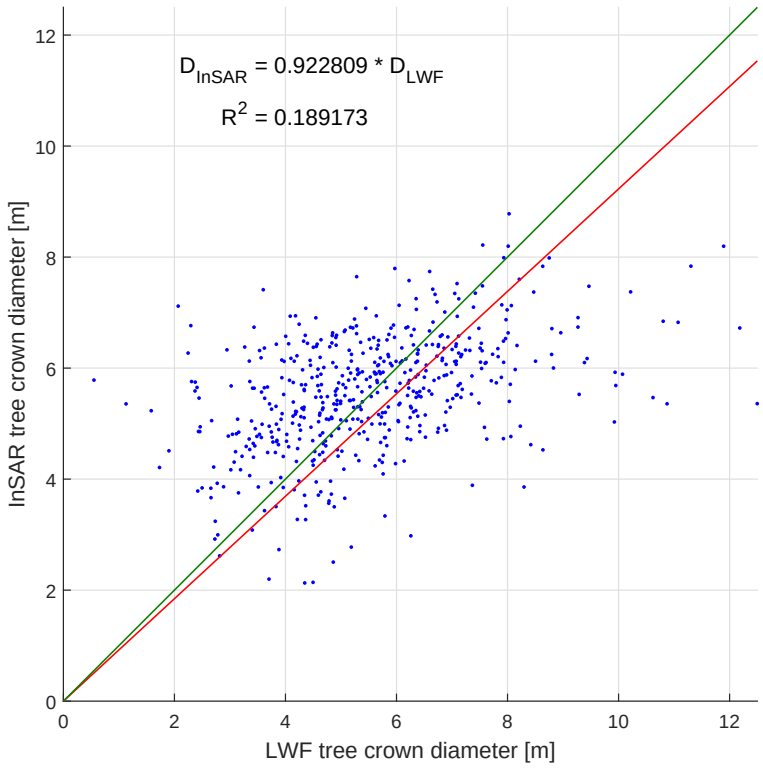

Fig. 4.14 Scatter plot of the InSAR tree crown diameters vs. the crown diameter of the corresponding (matched) LWF trees.

InSAR trees were also matched with trees detected on ALS and photogrammetric data. A direct use of the single tree detection algorithm presented in Section 4.3.2 (without use of the unavailable coherence information) fails with photogrammetric data, and gives suboptimal results with ALS data, preventing a fair direct comparison of the results. The algorithm would have to be adapted by using an appropriate parameterization of equations (4.3) and (4.4) for the ALS/photogrammetric cases. As segmentation of ALS- nor photogrammetry-based point clouds is beyond the scope of this publication, in order to achieve an elementary comparison, a simple tree detection was achieved by generating CHMs and detecting local maxima. The tree matching was then achieved in the same manner as with the LWF data, using the detected ALS and photogrammetric trees as the reference trees. A very high success rate was achieved (93 to 95%). Again, the taller the trees, the higher the success rate.

The localization and the height of the trees were compared; results are reported in Table 4.8. Again, a small but very stable South-East shift was noticeable. The InSAR tree heights were on average 1 to 1.5 m lower than the estimates from ALS and photogrammetric data. A regression analysis showed results very similar to those obtained in the regression analysis carried out on the CHMs in Section 4.4.1. The regression slopes varied between 0.954 and 0.966, with R^2 values between 0.81 and 0.887. The results are summarized in Table 4.9.

TABLE 4.8
ESTIMATED TREE PARAMETERS VS. ALS AND PHOTOGRAMMETRIC DATA

Reference	Difference (InSAR - reference)	Mean [m]	Std. dev. [m]
ALS leaf off	Height	-1.060	0.950
	Easting localization	0.407	0.565
	Northing localization	-0.383	0.551
ALS leaf on	Height	-1.257	0.959
	Easting localization	0.420	0.586
	Northing localization	-0.361	0.544
Photogrammetry leaf off	Height	-1.309	1.060
	Easting localization	0.300	0.617
	Northing localization	-0.289	0.592
Photogrammetry leaf on	Height	-1.473	1.107
	Easting localization	0.356	0.625
	Northing localization	-0.396	0.577

TABLE 4.9
TREE HEIGHTS REGRESSION ANALYSIS

Reference (X axis)	Regression slope *	R^2 *
LWF	0.949	0.627
ALS leaf off	0.966	0.887
ALS leaf on	0.960	0.869
Photogrammetry leaf off	0.959	0.873
Photogrammetry leaf on	0.954	0.810

* heights of matched InSAR trees in the Y-axis

4.5 Discussion

4.5.1 Point cloud characteristics

The InSAR-based point cloud was compared in Section 4.4.1 to equivalent products from full-waveform ALS and stereo-photogrammetry data. Observation of profiles as well as the analysis of the CHMs showed that all point clouds had an almost identical geolocation. The CHMs were very similar, confirmed by the very high R^2 values obtained when calculating regression lines, with the InSAR-based CHM having slightly lower heights. The vertical structures of the point clouds had very noticeable differences: while ALS data mapped the canopy down to the ground within gaps, InSAR showed only limited penetration inside the canopy, and the photogrammetric point cloud typically mapped only the canopy surface.

The good agreement in the geolocation and maximum height values are a testimony to well-designed measurement campaigns including tie points and verification points measured with DGPS, high quality hardware, and accurate data processing.

4.5.2 Forest segmentation and parameter extraction

For the InSAR data presented here, three characteristics combine together to produce a point cloud that could be easily segmented: (1) scattering mechanisms occur at multiple vertical levels, (2) the coherence information directly informs on the accuracy of a point's location, i.e. the confidence level with which the point can be used, (3) availability of multiple illumination directions helps to densify the point cloud.

As a consequence, the whole segmentation process took advantage of these parameters. Points with low coherence were discarded, resulting in distinct point clusters matching very well with actual trees. The horizontal point density map was used to derive a first estimation of the tree locations using a local maxima detection. This method was found to be more reliable than using the height information in the CHM, probably due to the noise level in the vegetation height information. In the second step of the forest segmentation, the normalized cut method (Shi & Malik, 2000) used the point distribution and the coherence information as weights in the similarity matrix.

The tree parameters estimated from the segmented InSAR point cloud were analyzed. The detection rate of the trees sampled in the LWF forestry data depended mainly on the tree height / DBH. Understory trees were not considered, as well as trees with a thin stem diameter. The remaining trees were detected with a success rate of ~90% for trees taller than 32 m / trees with a DBH larger than ~0.4 m. These large trees represented slightly more than half of the considered trees. Below these thresholds, the detection rate rapidly decreased together with the tree height / DBH. On average, ~50% of these remaining trees were detected. This is very likely explained by the limited penetration depth of the Ka-band radar waves. While photogrammetric data suffer from the same limitations, ALS data should provide a slightly better detection of low/understory trees, as reported in (Reitberger et al., 2009). The InSAR trees were also matched with local maxima of CHMs generated from the ALS and photogrammetric point clouds, with a very high success rate (> 90%). The InSAR tree localization was found to be shifted in the South-East direction. This consistent shift is likely to be explained by the illumination direction employed, resulting in more points on the South-Eastern side of trees, combined with the cluster centroid method used to estimate the horizontal tree positions.

A higher detection rate was achieved for conifers than for broad-leaved trees, although only by a limited and not conclusive margin. However, the estimated tree characteristics reported in Table 4.7 clearly indicate a more reliable detection of conifers than broad-leaved trees. The segmented point cloud was also visually inspected: in broad-leaved areas, the point density was more homogeneous and the canopy level did not vary as much as for areas covered by conifers, and the resulting segmentation was, therefore, less reliable. Are we detecting two trees or one tree with

two large branches or codominant stems? This is also an issue for single tree detection based on ALS point clouds.

The estimated tree height was found to be generally underestimated by ~1.6 m against the LWF data. An important issue here is that the tree height information from the LWF data is not very reliable. Still, this underestimation is also noticeable against the ALS and photogrammetric data (1 – 1.5 m). Most of this underestimation is directly related to the location of the scattering centers. The penetration depth is small for Ka-band radar waves compared to longer radar wavelengths, but it is still present. Although somewhat speculative, the decreasing regression slopes reported in Table 4.4 and Table 4.9, as well as the increasing mean height difference recorded in Table 4.8 against ALS leaf-off (spring 2014), ALS leaf-on (summer 2014), photogrammetry leaf-off (spring 2015), photogrammetry leaf-on (summer 2015), may indicate that a limited part of the underestimation is related to the tree growth. Beyond this systematic underestimation, a good agreement was measured for the tree height compared to the LWF data with a relatively high coefficient of determination of 0.627. The agreement was even higher between the InSAR tree heights and the local maxima detected in ALS- and photogrammetry-based CHMs.

The estimated crown diameter was on average virtually equal to the value reported in the forestry data. However, the standard deviation was quite large (1.714 m) and the low R^2 value of 0.189 indicated only a small correlation between the varying crown diameters. The estimation was particularly unreliable for trees with large crown diameters (broad-leaved trees), which also supports some doubts on broad-leaved trees segmentation accuracy.

Note that the local maxima used as an estimation for ALS and photogrammetric detected tree positions partly depend on the strength of the used Gaussian filter. This has a direct influence on the number of detected trees and thus on the detection rate of InSAR trees vs. ALS/photogrammetric trees. However, no significant differences were noticed in the average localization difference, neither in the average tree height difference nor in the regression slope and R^2 value when filtering strength was varied.

4.5.3 Data quality and limitations

Evaluation of the results requires extensive understanding of the specifications and limitations of the InSAR and reference data.

A first element is that the data collection campaigns were not simultaneous: although the studied forest is rather mature, trees were still growing, and a few of them were cut between the acquisition campaigns. The different vegetation states influence the results, although this element is not that important in this study given that 80% of the trees were conifers within the studied area, and even in the case of desiccated or fallen leaves, radar scattering still occurs against the sap- (water) filled tree branches. As a consequence, parts of the differences between the various measurements can be attributed to actual changes having taken place in the forest.

The tree height and crown diameter field measurements in the LWF data were collected by (1) measuring the distance between an observation point and the tree and (2) measuring the angles to the bottom and top of the tree, respectively right and left edges of the crown. The visibility and accurate determination of the tree-top position as well as the precision and accuracy of the angle readings introduce uncertainties that limit the accuracy of these measurements. The tree positions were measured with DGPS, which can be difficult to achieve at very high accuracy from within a forest.

The photogrammetry-based point cloud was not as reliable as the ALS-based result: the canopy mapped as a point cloud tended to be smoothed, possibly due to limited correlation between the source photogrammetric images. This happened most often for broad-leaved trees with leaves on. In such cases, the local maxima detection failed to detect individual trees. A few trees had

also obviously been cut between the two photogrammetric acquisition dates. These effects resulted in 6% and 11% fewer detected trees (local maxima) compared to ALS data for the photogrammetric leaf-off and leaf-on measurements, respectively. In addition, although it did not affect our results, some areas outside the LWF test site contained conifers with very low foliage density; in those cases, the photogrammetric point cloud mapped the ground level: the trees were not detected at all.

The InSAR data suffered from non-homogeneous illumination directions (see Section 4.2.2). As a result, the North-West sides of the trees were not illuminated and mostly in shadow, causing a ~0.5 m shift in the South-East direction to the position of the detected trees. This shift was noticeable in the tree localization comparison carried out w.r.t. all reference data, as reported in Table 4.7 and Table 4.8. Some areas on the North-West side of high tree groves were also not illuminated, and thus no trees were detected there. More homogeneous illumination directions, for example from four directions with 90° between each consecutive illumination direction, would deliver a higher positioning accuracy. The effect of the relatively shallow depression angle can also be seen in Table 4.4: the InSAR point cloud contained much larger unmapped areas in comparison to the two other techniques.

4.5.4 Outlook

The confidence on accurate single tree detection was lower for the broad-leaved trees than for the conifers. Additional information from SAR polarimetry would allow determining the nature of the mapped trees (Touzi et al., 2004). First experiments with dual-polarization MEMPHIS data in other test areas clearly show different polarization ratios for broad-leaved trees and conifers. This information could be fed into the normalized cuts segmentation to improve the segmentation reliability.

Generally, the experimental SAR-system MEMPHIS operated with four receiving antennas. This would allow for detection of up to three independent scatterers within each resolution cell, using SAR tomography (Capon, 1969; Schmidt, 1986; Schmitt & Stilla, 2014b). For forest point clouds, this might moderately increase the point density.

The memory requirements for the similarity matrix grow with the square of the number of points and therefore limit the area that can be segmented using the normalized cut algorithm. The implementation of a block processing method would allow handling of larger surfaces. It would have to produce the same segmentation for overlapping areas, which is a major challenge.

MEMPHIS data were used for this study, thus the InSAR processing method was developed and adapted for this particular sensor. However, a similar sensor would only require minor adaptations to the presented processing method.

A wider variety of system and acquisition parameters would also be of interest. They could involve minor changes, such as changing the depression angle to vary the shadow length and foreshortening properties, or performing acquisition campaigns using four illumination directions with 90° between each of them. A larger baseline would result in a lower sensitivity to phase noise, i.e., better vertical resolution. This could be achieved either by increasing the distance between the receiving antenna horns or by adding new receivers. To increase the coverage and fully take advantage of the SAR technique, an operational airborne system would have to be designed to use a larger elevation beam width and to fly at higher altitudes. This would require a higher peak power and/or longer pulses. An example of development in that direction is given in (Moller et al., 2011).

4.5.5 Conclusions

The study presented here validates millimeter wave multibaseline InSAR data as a reliable alternative to ALS- and photogrammetry-based data for forest monitoring. This validation was

achieved by comparing the InSAR-based results to independent forestry, ALS and stereo-photogrammetry data sources. Larger trees were accurately detected, their positions and heights were reliably measured, and an average crown diameter could be estimated. The underestimated height could probably be modelled and accurately compensated, as the only major limitation appeared to be limited penetration depth into the canopy. On the other hand, InSAR data bring in the advantages of SAR systems: the possibility to cover large areas with high resolution using a small number of acquisitions, the low dependency on weather and seasonal conditions, and the theoretical possibility of designing a spaceborne mission with similar properties.

Acknowledgments

The authors would like to acknowledge armasuisse W+T for financial and operational support, T. Brehm and the Fraunhofer/FHR team for the MEMPHIS data collection, C. Ackermann and R. Pail (TU Muenchen) for the IMU hardware, H. Torabzadeh and G. Milani of the University of Zurich, for the collection of *eBee* data, A. Gessler, C. Hug, P. Jakob and F. Sutter of WSL for providing the forestry measurements at *Vordemwald* LWF test site. This site is part of the UNECE Co-operative Programme on Assessment and Monitoring of Air Pollution Effects on Forests, ICP Forests (www.icp-forests.net). The contributions of F. Morsdorf and M.E. Schaepman are supported by the University Research Priority Program “Global Change and Biodiversity”.

4.6 Appendix

4.6.1 Data processing and implementation remarks

The article focuses on experimental MEMPHIS data and their processing. This processing, from the recorded raw data to the point cloud and the segmented forest used software almost exclusively developed in-house. As an exception, the combination of DGPS and IMU data was carried out using the *Inertial Explorer* commercial software provided by the company *Novatel*. Most of the SAR focusing and interferometric processing algorithms were implemented in the C++ programming language, taking advantage of CPU parallel computing. The remaining most computationally demanding algorithms (stepped-frequency processing and ML phase estimation) were implemented in CUDA for fast GPU parallel computing. The high level processing such as CHM generation, local maxima detection, normalized cuts segmentation and results analysis was performed on Matlab. For the normalized cuts point cloud segmentation, we used the Matlab code provided in (Cour et al., 2004) under a GNU General Public License. In that code, the computation of the similarity matrix was adapted to our needs.

The similarity matrix is a 2D symmetric matrix, with as many rows and columns as the number of points in the point cloud. The dimension of this matrix causes major computing difficulties. For our data, we made use of the fact that most values in the matrix were very low to reduce the load: the low values ($< 10^{-6}$) were set to 0 and the matrix converted to a Matlab sparse matrix. This proved to be sufficient for the InSAR point cloud covering the LWF area. Segmentation of larger point clouds was also tested, and at some point failed due to a lack of enough available computer memory. The threshold level depends on the computer, but at some point strategies to reduce the memory usage have to be found. A first strategy was to voxelize the data: all points inside a 3D voxel were aggregated to a single point, its coherence set as the average coherence (the same for other potential attributes). The segmentation was then achieved on the reduced number of voxels, with the results of the segmentation fed back to the individual points of the point cloud. Voxelizing the point clouds delays the moment where the computing limits are reached, but does not completely eliminate the problem. For even larger point clouds, a block processing method with overlapping edges has to be introduced, where merging the various segmented blocks might be a complicated task.

5 SYNOPSIS

5.1 Main results

In the last years, height measurements using SAR interferometry has reached in some contexts an operational status. The airborne GeoSAR system, that combines X- and P-band InSAR data, was matured into a commercial system. It is able to provide DTMs and DSMs at ~3 – 5 m resolution while covering large areas. The spaceborne TanDEM-X mission is providing a moderate-resolution DEM (~12 m) with near-worldwide coverage. In parallel, ALS has been increasingly used by authorities to map whole countries, delivering highly accurate DTMs, DSMs and point clouds. The development of full-waveform ALS, increasing point densities and sub-meter resolution contribute to its growing use for monitoring ecosystems.

The results accomplished in this thesis have to be considered in that context. They were achieved using the experimental MEMPHIS system, starting from its raw, "out of the sensor", data. These data were focused and interferometrically processed, resulting in accurate, high resolution (~0.4 – 2 m) topography data, therefore approaching the characteristics of ALS-based products. The generation of InSAR-based 3D point clouds with high point density was demonstrated. The utility of such products was proven by accurately detecting single trees and deriving some of their characteristics from a 3D point cloud of a forest canopy.

As such, this thesis shows that InSAR technology can be pushed to provide data characteristics that were often thought to be only attainable using ALS technology. As SAR resolution is independent of the range distance, an operational system with similar characteristics and wide coverage could be designed that would be able to provide valuable, high resolution topography data, potentially at a lower cost compared to ALS.

In the following, the main achievements of this thesis are structured according to the research questions presented in Section 1.4.

5.1.1 What are the prerequisites for generating high resolution images, accurate geolocation, and a trustworthy interferometric phase?

Basic focusing of millimeter wave SAR data and the computation of the interferometric phase are in principle no complicated tasks. However, focusing SAR data with a resolution close to the theoretically achievable value, achieving a geolocation accuracy in the same order of magnitude as the resolution, and calculating an interferometric phase that enables accurate topography measurement required sophisticated solutions.

(a) Navigation data: High quality navigation data is a major prerequisite. Navigation data consist of the sensor position, velocity, and attitude information corresponding to each radar pulse. Through a combination of several measurements, MEMPHIS navigation data were brought to a state of the art quality:

- The lever arms between GPS antenna, INS and SAR antennas were measured with centimeter accuracy using terrestrial surveying methods.
- DGPS measurements were collected at a 20 Hz sampling rate. A precise IMU delivered inertial measurements with a 500 Hz sampling rate. The DGPS, inertial and SAR data were synchronized using event and second marks. The DGPS and inertial data were combined together using Kalman filtering, resulting in absolute positioning accuracy better than 0.1 m.
- The antenna tilt angle was reliably measured by combining measurements from an accelerometer fixed on the antenna assembly with those from the IMU.

- Pitch and heading constant offsets were successfully calculated by comparing the Doppler centroid measurements from the navigation data with those estimated from the SAR data.

These high quality navigation data were crucial for several elements of the data processing: they made accurate motion compensation possible, in order to generate well-focused, accurately geolocated SAR images; they enabled precise antenna pointing estimation, necessary for elevation angle-dependent phase correction; the phase-to-height calculation relied on accurate navigation data.

(b) Reliable radar measurements: SAR focusing and InSAR processing require reliable radar measurements. This depends predominantly on the hardware generating, transmitting, receiving and sampling the signals. However, reliability can be enhanced through calibration of the radar measurements:

- Chirp replicas were measured for each receiving antenna and each stepped chirp. They enabled a synthesis of the full bandwidth resulting in optimum resolution.
- Elevation antenna phase patterns were calculated for each receiving antenna to compensate for elevation angle-dependent phase errors. This correction removed recurring height errors of up to 0.5 m when using the C2F approach. It enabled the use of the ML phase estimation algorithm, which would deliver erratic results without this calibration. A first implementation relied on the depression angle. It was subsequently improved by accounting for platform attitude variations.

(c) Auxiliary information: Accurate motion compensation requires range- and topography-dependent motion compensation. Coarse resolution DEMs were used for this purpose. They were further smoothed to avoid large height variations within MEMPHIS the ~80 m synthetic aperture. These DEMs were also used for interferometric phase flattening, to simplify the phase unwrapping process.

For calibration and quality control purposes, several corner reflectors were placed on all test sites, their positions were measured with DGPS at centimeter accuracy. The signatures of the reflectors were used to (i) calibrate the sampling window start time and (ii) assess the achieved focusing quality (resolution, PSLR) and geolocation accuracy. They also served as tie points for absolute phase calibration.

This absolute phase calibration requires at least one tie point for each acquisition. Using a calibrated, operational system, the tie points do not need to be corner reflectors; they could also be flat surfaces of at least 1 m^2 with homogeneous backscatter properties (such as short grasses), when their heights and center positions are well known.

(d) Well-adapted algorithms: Appropriate algorithms were selected as components of the SAR focusing and InSAR processing. They were carefully implemented to limit loss of information, avoid aliasing, and restrict approximation errors. They were enhanced by inclusion of calibration steps. The SAR focusing and InSAR algorithms are reviewed further in Section 5.1.2.

(e) Limitations: Hardware- and data processing-related limitations were exhaustively studied in Section 2.5.1.

The antenna phase center positions define the available baselines; inaccuracies in the manufacturing of the antenna horns, a wrong antenna tilt angle, and errors in the IMU attitude measurement can result in baseline vectors that deviate from their nominal values. Non-ideal antenna shapes may also be the underlying cause of elevation angle-dependent phase errors. High quality IMU data, precise antenna tilt angle measurement, and elevation angle-dependent phase corrections were used to constrain these errors.

The motion compensation process was based on already existing DEMs. Signatures of objects at a different height than recorded in the reference DEM were, therefore, subject to residual effects

(e.g. positioning and phase offsets, defocusing). The resulting horizontal and vertical deviations depended on (i) the position difference between the real and linearized sensor positions and (ii) the height difference between the actual and reference DEM height at the object's position.

The phase-to-height conversion model used an approximated baseline calculated as the position difference between the linearized tracks. This approximation only delivers accurate results (i) when the height used for the motion compensation is accurate or (ii) when the real baseline vector matches the approximated baseline vector. The process described in Section 3.3.2.5 was implemented to compensate phase errors that can be introduced by this approximation.

Misregistration of the SLCs results in decorrelation and phase errors. The short baselines and relatively narrow elevation beam width enabled use of the SLCs without a complex coregistration step.

The magnitude of all these potential errors and their influence on the generated topography data were evaluated. Calibration and correction steps were implemented, such that the remaining errors were acceptable, as evidenced by the results reported in Sections 2.4, 3.4 and 4.4.

5.1.2 Which SAR focusing and interferometric processing algorithms are most suitable to generate point clouds or DSMs?

The choice of SAR focusing and interferometric processing algorithms was constrained by the system and raw data parameters, the stability of the airborne platform, and the requirements we set for the final data quality: a resolution close to the theoretical value, a comprehensive geometry with geolocation accuracy in the same order of magnitude as the system resolution, a minimization of SAR focusing artifacts, and reliable phase information uncorrupted by systematic errors.

(a) Range compression and stepped-frequency processing: The selected method used matched filtering to focus the individual chirps, and then synthesized the full stepped-frequency bandwidth by concatenating the bandwidth parts in the frequency domain. The following points were crucial to generate well-focused data.

- Chirp replica were used for the matched filtering. They were also used to generate a frequency domain weighting filter that ensured that all frequencies composing the full bandwidth were weighted equally.
- The stepped-frequency processing included a phase matching algorithm that was used to match the phase values of the overlapping frequencies. Without phase matching, target signatures can appear multiple times in the time domain range compressed image, i.e., up to 8 times with slight range shifts.

(b) Azimuth focusing: A frequency-domain algorithm was selected for the azimuth focusing. This was made possible by the stability of the C-160 platform used for MEMPHIS acquisitions. Lighter platforms that have difficulties following straight flight paths and show less stable attitude behavior might require a time-domain azimuth focusing.

The Extended Omega-K algorithm was found to be most suitable for azimuth focusing: it supports range- and topography-dependent motion compensation. In contrast to the Extended Chirp Scaling algorithm, it only deals with the *azimuth* focusing and therefore directly supports stepped-frequency data.

The implemented range- and topography-dependent motion compensation used the beam center approximation, suitable due to the narrow azimuth beam width. The implemented algorithm also included handling of a Doppler centroid varying in range and azimuth directions (through the use of a block processing). The range spectrum shift caused by the azimuth focusing in the presence of squint was compensated to avoid interferometric phase errors. All algorithm steps were verified to not provoke unintended losses that would lower the SNR. Finally, a relative

radiometric compensation was added that corrected the beam amplitude using the antenna patterns and the range spreading losses.

(c) Focusing results: The results of the SAR focusing were analyzed and fulfilled the requirements. The target signatures were well focused in range, did not appear multiple times, confirming the phase matching effectiveness. Resolutions of ~0.17 m and ~0.1 m were measured in range and azimuth respectively, very close to the theoretical values. The zero-Doppler geometry yielded high geolocation accuracy, with errors typically below 0.1 m in both the range and azimuth directions in *Memmingen*. In the *Feldberg* test site, they were also typically below 0.1 m in range and for three of the four acquisitions, and below 0.2 m in azimuth. Similar results were obtained for other test sites not reported on within this thesis.

(d) Interferometric processing: Interferogram generation requires well co-registered channels. Using signatures of corner reflectors, the misregistration was measured with sub-pixel accuracy. For the longest baseline, the largest measured misregistrations were 2.1 cm in range and 1.3 cm in azimuth. This corresponds to ~1/24 and ~1/46 the size of the considered resolution cells (3 range and 12 azimuth looks) that were later used for generating the interferograms. The maximum misregistration was also calculated analytically, yielding similar results. Both the expected and measured misregistrations were low enough to ensure that the processor did not cause artificially low coherence.

For the interferometric phase estimation and unwrapping, the simple but robust C2F algorithm was first developed. It started with calculation of the interferograms computed from SLC pairs. The interferogram generated from the shortest baseline/largest ambiguity height was first unwrapped with the reliable SNAPHU algorithm. Interferograms with longer baselines were then sequentially unwrapped using information from the previously unwrapped interferograms. The C2F algorithm was then compared to and eventually replaced by the ML algorithm. The reason for this is discussed in Section 5.1.3.

The range, azimuth and phase values, were transformed into 3D Cartesian coordinates using straightforward geometric calculations. Working in global Cartesian coordinates allowed to avoid errors with Earth curvature. These were then transformed back into local map coordinates for further steps. DSMs were generated by regridding and filtering the results; they were used to assess the height accuracy, by comparing them to ALS-based DTMs.

Error sources were considered, and corrected when possible. They included elevation-dependent phase errors, motion compensation-induced phase errors, and constant phase offsets.

The validity of the SAR focusing and interferometric processing was confirmed by the resulting highly accurate products, such as those illustrated in Fig. 5.1.

(e) Limitations: One major limitation came in a small number of acquisitions with very large and rapid Doppler centroid variations, changing up to one PRF within a synthetic aperture. These variations could not be managed properly and resulted in ghost targets with related phase errors. Better results might have been possible using a time-domain processor.

The MEMPHIS system uses very short pulses, which result in strong range sidelobes when illuminating targets with intense backscattering, as it is often the case with man-made objects. These sidelobes could be moderately mitigated using multi-step adaptive processing (Méndez Domínguez et al., 2016). They were not found in acquisitions mapping natural environments such as grasslands or forests.

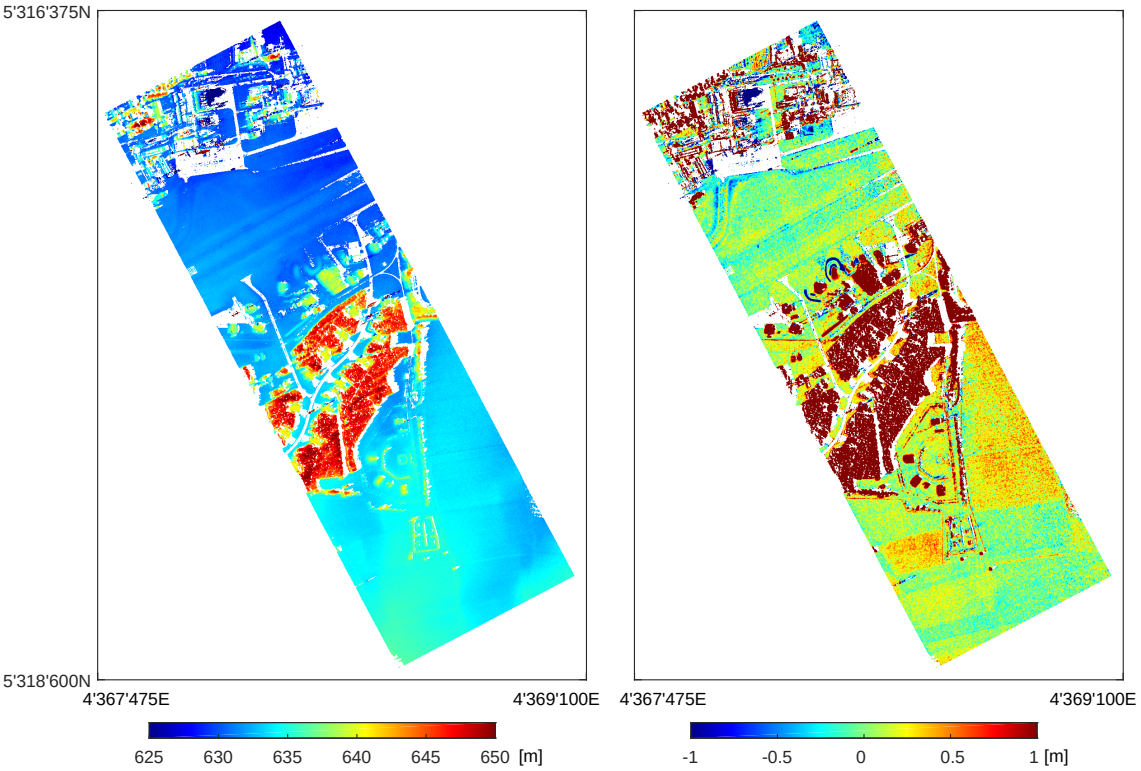

Fig. 5.1 Left: InSAR-based DSM using acquisition M3 at *Memmingen*. Right: difference between the InSAR-DSM and an ALS-based reference DTM. Coordinate system: Gauss-Krüger zone 4.

5.1.3 Can we use a maximum likelihood phase estimation algorithm that takes into account the information from all receiving antennas to achieve better phase estimation, and is it superior to using the longest baseline alone?

The study carried out in Chapter 0 demonstrated that ML phase estimation was the most suitable technique for experimental airborne multibaseline data. The ML method combined in an optimal way the information from all receiving antennas to compute partially unwrapped phase values.

(a) Data calibration: MEMPHIS data originally did not match well enough the assumptions made in the model behind the ML phase estimation, i.e., measurements corresponding to perfectly aligned phase centers. Carefully designed calibration steps were required to bring the data closer to the ML model. These calibration steps included elevation angle-dependent phase correction for the three slave receivers extended from the depression angle-dependent phase correction presented in Chapter 2, as well as a constant phase offset applied to two of the four SLC datasets. The calibration steps were enhanced by an improved estimation of the antenna tilt angle and a refined estimation of the beam orientation.

(b) Phase noise comparison: Phase noise results using ML phase estimation were compared to those using the C2F method. For this, the two processing chains were designed to be as similar as possible (see Fig. 3.1). Flat grassland areas were selected for comparisons using acquisitions made over the Memmingen test site.

The results showed that with only four looks, the noise level was marginally higher with the ML approach in comparison to the C2F method. However, with more looks, the ML method consistently delivered lower noise (see Fig. 3.9): noise variance using the C2F approach was steadily ~1.05 times the variance obtained with ML method, with a similar number of outliers for

both methods. The difference between the results from both methods was validated with a significance analysis.

The theory tells us that the higher the spatial decorrelation, the better the ML method should be in comparison with the C2F method. This spatial decorrelation is typically found in terrain slopes facing the illumination direction, and more generally in steep topography, rising with the baseline length. ML phase estimation was shown to perform slightly better than C2F method in the scenario least favorable for ML, i.e., using data acquired of flat grassland areas where spatial decorrelation does not drastically increase with baseline length. This implies that we can expect ML to perform universally better than the C2F method.

Hence, through the study conducted here, ML phase estimation was shown to be well adapted to an experimental single-pass, multibaseline airborne SAR interferometric system, after careful SAR data focusing, and all necessary calibration steps.

(c) Limitations: Both C2F and ML phase estimation methods require a minimum number of looks to yield reliable results. Using a very low number of looks resulted in numerous outliers and significant phase noise. Acceptable results were obtained using at least 16 looks; outliers almost disappeared with 36 looks. As a consequence, the required multilooking limited the highest useful spatial resolution to approximately 0.4 – 0.6 m.

The measured phase noise was significantly larger than the estimation from Cramer-Rao bound. This difference can be explained by real world parameters such as variations in vegetation height, residual topography, as well as system and processing imperfections.

5.1.4 How does the point cloud of a temperate coniferous forest generated from multi-aspect, multibaseline InSAR data compare to equivalent products from other sensors?

InSAR data were acquired over a temperate coniferous forest and processed into point clouds using ML phase estimation. These point clouds were aggregated into a single point cloud with high point density. A region of interest (Fig. 5.2) was defined based on the available reference data. This InSAR-based point cloud was compared to ALS- and stereo-photogrammetry-based point clouds.

(a) Data comparison: The vertical structures of the point clouds were investigated using profiles. They had noticeable differences: while ALS data mapped the canopy down to the ground with some gaps, the InSAR results showed only limited penetration into the canopy. The stereo-photogrammetry-based point clouds typically only mapped the canopy surface.

Canopy height models (CHMs) were generated to compare the data sets. Using cross-correlation of the CHMs, the geolocation was shown to be almost identical for all products. Scatter plots were generated to compare the CHMs. While the height of the InSAR CHM was slightly lower than that from the other sensors, very high coefficients of determination were measured when calculating regression lines, with R^2 values between 0.8 and 0.9. Possible reasons for the InSAR-height underestimation are discussed in Section 5.1.5.

(b) Limitations: The depression angle of the radar beam resulted in some shadowed areas behind trees. Clearings or areas with low trees surrounded by larger trees were therefore typically in shadow and no or very little information was available in the InSAR point cloud.

Directionality effects caused by the radar illumination directions used during the acquisition campaign were also noticeable. Due to flight safety restrictions, the test area was only able to be illuminated from the South, South-East and East. As a consequence, the South or East sides of trees showed higher point densities than their North and West sides.

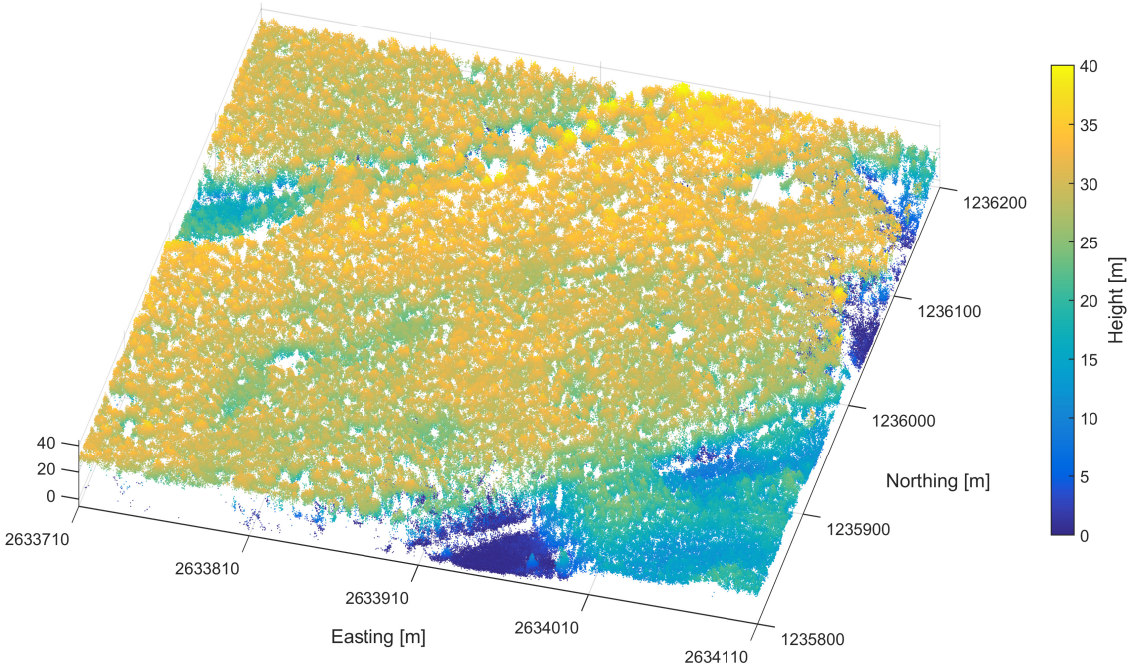

Fig. 5.2 Aggregated InSAR-based point cloud of a forest canopy near *Vordemwald*, Aargau. Coordinate system: LV95.

5.1.5 How do the tree parameters estimated from the segmented point cloud compare to reference forestry data and alternative remote sensing approaches?

The InSAR-based point cloud generated of the reference forested area was segmented using a two-step approach. Approximate tree positions were first estimated by finding the local maxima of the point density map of that area. The point cloud was then effectively segmented using a normalized cut technique which considered the number and locations of the local maxima detected in the first step. The results were used to compute the tree positions, heights, and crown diameters.

(a) Tree detection and parameters estimation: The detected trees were matched to the trees sampled in the reference forestry database, as shown in Fig. 4.11. The understory trees and trees with a thin stem diameter were not considered. Most of the larger trees and approximately half of the smaller trees were detected (see Fig. 4.12). This is very likely explained by the limited penetration depth of the Ka-band radar waves. Trees detected on InSAR data were also matched to local maxima detected on the ALS- and photogrammetry-based CHMs, with success rates between 93 and 95%.

The localization of the detected trees was found to be shifted slightly in the South-East direction, very likely due to the higher point density on the South and East sides of the trees caused by the used illumination directions. The comparison with the forestry data and the local maxima detected on the ALS- and photogrammetry-based CHMs yielded similar results. In addition to this constant shift, the localization of the detected trees agreed well with the results of the other data sources.

The tree height was found to have been underestimated by 1–1.5 m. That could be due to several factors:

- The field measurements were not extremely reliable due to the difficulty of accurately determine the tree tops from the ground.

- The ALS and photogrammetry data were acquired more recently than the InSAR data and thus some growth very likely happened during that interval.
- The radar waves still penetrate into the canopy to some extent, even with a Ka-band wavelength.
- Differences in the reference geometry were excluded by comparing results in non-forested areas.

Aside from this systematic underestimation, good agreement was observed between the independent tree height estimates, with a R^2 value of 0.627 in comparison with the forestry data and R^2 values between 0.8 and 0.9 in comparison with the ALS and photogrammetry-based tree height estimates.

The crown diameter was accurately estimated in the mean, however with a low coefficient of determination.

(b) Limitations: Using the InSAR technique, the smaller the tree, the lower the detection rate. In particular understory trees were typically not detected. Broad-leaved trees were also less reliably detected than conifers: this was noticeable in the larger standard deviations measured for the estimated tree localizations and crown diameters. These issues are shared by the other airborne remote sensing techniques.

In addition, the limitations reported in the previous section also apply here: areas with low trees surrounded by tall trees were typically in shadow and the low trees were not detected. A steeper depression angle would help mitigate this deficiency.

The underestimated height is not a major limitation: implementing a correction should be possible once it has been well characterized. Neither is the observed South-East tree localization shift: more homogeneous illumination directions should solve this issue.

5.2 Conclusions & Outlook

The potential of millimeter wave multibaseline SAR interferometry for carrying out reliable and accurate high resolution topography measurements was demonstrated using data from an experimental airborne system. The advances achieved within this thesis include contributions to hardware improvements, system and data calibration, and the development of a complete pipeline from raw data to the generation of DSMs or 3D point clouds. All elements of the data processing underwent strict quality control, ensuring that the obtained results were as accurate as possible.

In the following, the major achievements of the thesis are summarized. The prerequisites necessary for generating high resolution images, accurate geolocation, and a trustworthy interferometric phase were investigated. These prerequisites, such as using highly accurate DGPS and IMU systems, would be very similar using a different InSAR system. Height measurements with high absolute accuracy were demonstrated, with the results matching closely those from precise ALS measurements. The ML phase estimation was shown to be the most effective method for single-pass airborne multibaseline InSAR. Finally, the thesis proved that detection and estimation of the height, position and crown diameter of single trees using an InSAR-based point cloud of a forest canopy was possible, validating millimeter wave multibaseline InSAR-data as a credible alternative to other remote sensing techniques such as ALS and stereo-photogrammetry for monitoring forest ecosystems.

The data processing could be enhanced in several ways: (i) The strong range sidelobes found around targets with intense backscattering could be partially remedied using multi-step adaptive pulse compression (Méndez Domínguez et al., 2016). A reduction of these sidelobes reveals areas that are currently covered by these sidelobes, thus improving the quality of the height estimates and increasing the coverage in complicated terrain such as built-up areas. (ii) The phase estimation relies on a boxcar window; areas where the local stationarity assumption does not hold, such

as in built-up areas, would benefit from a more elaborate sample selection. Example of developments in that direction include non-local InSAR (Deledalle et al., 2011) or adaptive sample selection (Vasile et al., 2006). (iii) The MEMPHIS system operated with four receiving antennas. This would allow for detection of up to three independent scatterers within each resolution cell, using SAR tomography (Capon, 1969; Schmidt, 1986; Schmitt & Stilla, 2014b). Built-up areas would benefit the most from developments in this direction.

In the domain of forest assessment, additional information from SAR polarimetry would allow determination of the nature of the mapped trees (Touzi et al., 2004). First experiments with dual-polarization MEMPHIS data clearly showed different polarization ratios for broad-leaved trees and conifers. This information could be fed into the normalized cuts segmentation to improve the reliability of the segmentation.

In addition to the monitoring of forest ecosystems, the advances presented here also open up new possibilities for monitoring various land cover types, in land cover classification, and in the 3D-mapping and analysis of man-made objects. For these applications, the results could also be enhanced using polarimetric data. First experiments using InSAR-based point clouds of man-made objects show that the physical dimensions of objects such as (but not limited to) construction cranes, electric poles, or aircraft can be accurately estimated.

InSAR-based point clouds have promising applications in the field of change detection: (i) the inherent geolocation of the points removes the need for a precise external DTM or DSM; (ii) shadowed areas can be filtered using a coherence threshold, reducing the number of false alarms. The combination of the geolocation, height information, and coherence threshold make it possible to detect changes using different acquisition geometries without suffering from high false alarm rates. Change detection using these point clouds has a significant potential in disaster monitoring, ecosystem assessment, agriculture, and urban studies.

The results of the thesis encourage further development of millimeter wave SAR interferometry: in improved methods, new applications, and upgraded hardware. A new, more operational system could be designed based on the major findings presented here; compared to the MEMPHIS system, enhancements for larger coverage, higher resolution and simultaneous polarimetry and interferometry measurements should be considered. The design of a spaceborne millimeter wave system, as considered by ESA (Dupuis et al., 2013), is also encouraged. While potential stumbling blocks such as assuring stable multiple baselines and atmospheric disturbances would have to be addressed, this would have the advantages of near-worldwide coverage, larger swath widths, and potentially short revisit times.

LIST OF ABBREVIATIONS

A/D	Analog-to-Digital
ALS	Airborne Laser Scanning
C2F	Coarse-to-Fine
CHM	Canopy Height Model
CNC	Computerized Numerical Control
CPU	Central Processing Unit
DBH	Diameter at Breast Height
DC	Doppler Centroid
DEM	Digital Elevation Model
DGPS	Differential Global Positioning System
DLR	*Deutsches Zentrum für Luft- und Raumfahrt e.V.* (German Aerospace Center)
DSM	Digital Surface Model
DTM	Digital Terrain Model
ESA	European Space Agency
FFT	Fast Fourier Transform
Fraunhofer/FHR	Fraunhofer Institute for High Frequency Physics and Radar Techniques
GIS	Geographic Information System
GMTI	Ground Moving Target Indication
GPS	Global Positioning System
GPU	Graphics Processing Unit
IFFT	Inverse Fast Fourier Transform
IMU	Inertial Measurement Unit
INS	Inertial Navigation System
InSAR	SAR Interferometry
JPL	Jet Propulsion Laboratory
LWF	*Langfristige Waldökosystem-Forschung* (Long term forest ecosystem research programme)
Matlab	Matrix Laboratory
MEMPHIS	Millimeterwave Experimental Multifrequency Polarimetric High-resolution Interferometric System
ML	Maximum Likelihood
NMEA	National Marine Electronics Association
PolInSAR	Polarimetric SAR Interferometry
PRF	Pulse Repetition Frequency
PSLR	Peak Sidelobe Ratio
RC	Range-Compressed
RCM	Range Cell Migration
SAR	Synthetic Aperture Radar
SLC	Single Look Complex (range-compressed and azimuth-focused complex SAR data)
SNAPHU	Statistical-cost Network-flow Algorithm for Phase Unwrapping

SNR	Signal-to-Noise Ratio
SRTM	Shuttle Radar Topography Mission
TanDEM-X	TerraSAR-X add-on for Digital Elevation Measurements
TomoSAR	SAR Tomography
UAV	Unmanned Aerial Vehicle
UTM	Universal Transverse Mercator coordinate system
WSL	*Eidg. Forschungsanstalt für Wald, Schnee und Landschaft* (Swiss Federal Institute for Forest, Snow and Landscape Research)

REFERENCES

Arce, G. R. (2005). *Nonlinear signal processing: a statistical approach*. Hoboken, New Jersey, USA: John Wiley & Sons.

Balzter, H., Rowland, C. S., & Saich, P. (2007). Forest canopy height and carbon estimation at Monks Wood National Nature Reserve, UK, using dual-wavelength SAR interferometry. *Remote Sensing of Environment, 108*(3), 224-239. doi:10.1016/j.rse.2006.11.014

Bamler, R., & Hartl, P. (1998). Synthetic aperture radar interferometry. *Inverse problems, 14*(4), R1. doi:10.1088/0266-5611/14/4/001

Bara, M., Scheiber, R., Broquetas, A., & Moreira, A. (2000). Interferometric SAR signal analysis in the presence of squint. *IEEE Transactions on Geoscience and Remote Sensing, 38*(5), 2164-2178. doi:10.1109/36.868875

Blunt, S. D., & Gerlach, K. (2006). Adaptive pulse compression via MMSE estimation. *IEEE Transactions on Aerospace and Electronic Systems, 42*(2), 572-584. doi:10.1109/TAES.2006.1642573

Brenner, A. R., & Roessing, L. (2008). Radar imaging of urban areas by means of very high-resolution SAR and interferometric SAR. *IEEE Transactions on Geoscience and Remote Sensing, 46*(10), 2971-2982. doi:10.1109/TGRS.2008.920911

Brenner, A. R., Roessing, L., & Berens, P. (2010). *Potential of very high resolution SAR interferometry for urban building analysis.* Paper presented at the 8th European Conference on Synthetic Aperture Radar (EUSAR), Aachen, Germany.

Cafforio, C., Prati, C., & Rocca, F. (1991). SAR data focusing using seismic migration techniques. *IEEE Transactions on Aerospace and Electronic Systems, 27*(2), 194-207. doi:10.1109/7.78293

Capaldo, P., Crespi, M., Fratarcangeli, F., Nascetti, A., & Pieralice, F. (2011). High-resolution SAR radargrammetry: A first application with COSMO-SkyMed spotlight imagery. *IEEE Geoscience and Remote Sensing Letters, 8*(6), 1100-1104. doi:10.1109/LGRS.2011.2157803

Capon, J. (1969). High-resolution frequency-wavenumber spectrum analysis. *Proceedings of the IEEE, 57*(8), 1408-1418. doi:10.1109/PROC.1969.7278

Chen, C. W. (2001). *Statistical-Cost Network-Flow Approaches to Two-Dimensional Phase Unwrapping for Radar Interferometry.* (Ph.D. dissertation), Stanford University, Stanford, California, USA.

Chen, C. W., & Zebker, H. A. (2001). Two-dimensional phase unwrapping with use of statistical models for cost functions in nonlinear optimization. *Journal of the Optical Society of America A, 18*(2), 338-351. doi:10.1364/JOSAA.18.000338

Cherubini, P., & Innes, J. (2000). Switzerland: The Swiss long-term forest ecosystem research programme. In J. Gosz, C. French, P. Sprott, & M. White (Eds.), *The International Long Term Ecological Research Network 2000: Perspectives from Participating Networks* (pp. 56-59).

University of New Mexico, Albuquerque, New Mexico, USA: US Long Term Ecological Research Network Office.

Comaniciu, D., & Meer, P. (2002). Mean shift: A robust approach toward feature space analysis. *IEEE Transactions on Pattern Analysis and Machine Intelligence, 24*(5), 603-619. doi:10.1109/34.1000236

Corsini, G., Diani, M., Lombardini, F., & Pinelli, G. (1999). Simulated analysis and optimization of a three-antenna airborne InSAR system for topographic mapping. *IEEE Transactions on Geoscience and Remote Sensing, 37*(5), 2518-2529. doi:10.1109/36.789647

Cour, T., Stella, Y., & Jianbo, S. (2004). MATLAB Normalized Cuts Segmentation Code. *www.cis.upenn.edu/~jshi/software/*.

Curlander, J. C., & McDonough, R. N. (1991). *Synthetic aperture radar*. Hoboken, New Jersey, USA: John Wiley & Sons.

D'Errico, J. (2004). Inpaint_nans. *www.mathworks.com/matlabcentral/fileexchange/4551-inpaint-nans*.

Deledalle, C.-A., Denis, L., & Tupin, F. (2011). NL-InSAR: Nonlocal interferogram estimation. *IEEE Transactions on Geoscience and Remote Sensing, 49*(4), 1441-1452. doi:10.1109/TGRS.2010.2076376

Dorobantu, R., & Gerlach, C. (2004). *Investigation of a navigation grade RLG SIMU type INAV-RQH* (3934205151). Retrieved from Munich, Germany:

Dubois-Fernandez, P., Ruault Du Plessis, O., Le Coz, D., Dupas, J., Vaizan, B., Dupuis, X., Cantalloube, H., Coulombeix, C., Titin-Schnaider, C., Dreuillet, P., Boutry, J., Canny, J., Kaisermertz, L., Peyret, J., Martineau, P., Chanteclerc, M., Pastore, L., & Bruyant, J. (2002). *The ONERA RAMSES SAR system.* Paper presented at the IEEE International Geoscience and Remote Sensing Symposium (IGARSS), Toronto, Canada. doi:10.1109/IGARSS.2002.1026233

Duncanson, L., Rourke, O., & Dubayah, R. (2015). Small Sample Sizes Yield Biased Allometric Equations in Temperate Forests. *Scientific Reports, 5*, 17153. doi:10.1038/srep17153

Dupuis, X., Nouvel, J.-F., & Dubois-Fernandez, P. (2013). *KaSAR final report*. Retrieved from Salon de Provence, France: *earth.esa.int/documents/10174/134665/KaSAR_Final_Report.pdf*

Esposito, C., Amaral, T., Lanari, R., Câmara de Macedo, K. A., Moreira, J., Vaz, E., Wimmer, C., & Perna, S. (2013). *Generation of high resolution interferograms in urban areas via airborne SAR sensors.* Paper presented at the Joint Urban Remote Sensing Event (JURSE), São Paulo, Brazil. doi:10.1109/JURSE.2013.6550709

Essen, H., Brehm, T., & Boehmsdorff, S. (2007). *Multibaseline interferometric SAR at millimeterwaves, test of an algorithm on real data and a synthetic scene.* Paper presented at the SPIE Florence, Italy. doi:10.1117/12.726293

Farr, T. G., Rosen, P. A., Caro, E., Crippen, R., Duren, R., Hensley, S., Kobrick, M., Paller, M., Rodriguez, E., Roth, L., Seal, D., Shaffer, S., Shimada, J., Umland, J., Werner, M., Oskin, M., Burbank, D., & Alsdorf, D. (2007). The shuttle radar topography mission. *Reviews of geophysics, 45*(2), 1-33. doi:10.1029/2005RG000183

Ferraiuolo, G., Pascazio, V., & Schirinzi, G. (2004). Maximum a posteriori estimation of height profiles in InSAR imaging. *IEEE Geoscience and Remote Sensing Letters, 1*(2), 66-70. doi:10.1109/LGRS.2003.822882

Ferretti, A., Prati, C., & Rocca, F. (1999). Multibaseline InSAR DEM reconstruction: The wavelet approach. *IEEE Transactions on Geoscience and Remote Sensing, 37*(2), 705-715. doi:10.1109/36.752187

Fornaro, G., Monti Guarnieri, A., Pauciullo, A., & De-Zan, F. (2006). Maximum likelihood multi-baseline SAR interferometry. *IEE Proceedings-Radar, Sonar and Navigation, 153*(3), 279-288. doi:10.1049/ip-rsn:20045113

Fornaro, G., Monti Guarnieri, A., Pauciullo, A., & Tebaldini, S. (2005). Joint multi-baseline SAR interferometry. *EURASIP Journal on Applied Signal Processing, 2005*, 3194-3205. doi:10.1155/ASP.2005.3194

Frey, O., Magnard, C., Rüegg, M., & Meier, E. (2009). Focusing of airborne synthetic aperture radar data from highly nonlinear flight tracks. *IEEE Transactions on Geoscience and Remote Sensing, 47*(6), 1844-1858. doi:10.1109/TGRS.2008.2007591

Frey, O., & Meier, E. (2011). 3-D time-domain SAR imaging of a forest using airborne multibaseline data at L-and P-bands. *IEEE Transactions on Geoscience and Remote Sensing, 49*(10), 3660-3664. doi:10.1109/TGRS.2011.2128875

Graham, L. C. (1974). Synthetic interferometer radar for topographic mapping. *Proceedings of the IEEE, 62*(6), 763-768. doi:10.1109/PROC.1974.9516

Gray, A. L., & Farris-Manning, P. J. (1993). Repeat-pass interferometry with airborne synthetic aperture radar. *IEEE Transactions on Geoscience and Remote Sensing, 31*(1), 180-191. doi:10.1109/36.210459

Guizar-Sicairos, M., Thurman, S. T., & Fienup, J. R. (2008). Efficient subpixel image registration algorithms. *Optics letters, 33*(2), 156-158. doi:10.1364/OL.33.000156

Hensley, S., Chapin, E., Freedman, A., Le, C., Madsen, S. N., Michel, T., Rodriguez, E., Siqueira, P., & Wheeler, K. (2001). *First P-band results using the GeoSAR mapping system.* Paper presented at the IEEE International Geoscience and Remote Sensing Symposium (IGARSS), Sydney, NSW, Australia. doi:10.1109/IGARSS.2001.976078

Horn, R. (1996). *The DLR airborne SAR project E-SAR.* Paper presented at the International Geoscience and Remote Sensing Symposium (IGARSS), Lincoln, NE, USA. doi:10.1109/IGARSS.1996.516751

Hyyppä, J., Kelle, O., Lehikoinen, M., & Inkinen, M. (2001). A segmentation-based method to retrieve stem volume estimates from 3-D tree height models produced by laser scanners. *IEEE Transactions on Geoscience and Remote Sensing, 39*(5), 969-975. doi:10.1109/36.921414

iMAR. (2010). Technical Data of iNAV-RQH-0018. *www.imar-navigation.de/downloads/nav_rqh_0018_en.pdf*.

Jain, A. K., & Dubes, R. C. (1988). *Algorithms for clustering data*. Upper Saddle River, NJ, USA: Prentice-Hall, Inc.

James, M. R., & Robson, S. (2012). Straightforward reconstruction of 3D surfaces and topography with a camera: Accuracy and geoscience application. *Journal of Geophysical Research: Earth Surface (2003–2012), 117*(F3). doi:10.1029/2011JF002289

Joerg, P. C., Morsdorf, F., & Zemp, M. (2012). Uncertainty assessment of multi-temporal airborne laser scanning data: A case study on an Alpine glacier. *Remote Sensing of Environment, 127*, 118-129. doi:10.1016/j.rse.2012.08.012

Kaartinen, H., Hyyppä, J., Yu, X., Vastaranta, M., Hyyppä, H., Kukko, A., Holopainen, M., Heipke, C., Hirschmugl, M., Morsdorf, F., Næsset, E., Pitkänen, J., Popescu, S., Solberg, S., Wolf, B. M., & Wu, J.-C. (2012). An international comparison of individual tree detection and extraction using airborne laser scanning. *Remote Sensing, 4*(4), 950-974. doi:10.3390/rs4040950

Karam, M., Fung, A. K., Lang, R. H., & Chauhan, N. S. (1992). A microwave scattering model for layered vegetation. *IEEE Transactions on Geoscience and Remote Sensing, 30*(4), 767-784. doi:10.1109/36.158872

Krieger, G., Moreira, A., Fiedler, H., Hajnsek, I., Werner, M., Younis, M., & Zink, M. (2007). TanDEM-X: A satellite formation for high-resolution SAR interferometry. *IEEE Transactions on Geoscience and Remote Sensing, 45*(11), 3317-3341. doi:10.1109/TGRS.2007.900693

Le Toan, T., Beaudoin, A., Riom, J., & Guyon, D. (1992). Relating forest biomass to SAR data. *IEEE Transactions on Geoscience and Remote Sensing, 30*(2), 403-411. doi:10.1109/36.134089

Lee, H., & Liu, J. G. (2001). Analysis of topographic decorrelation in SAR interferometry using ratio coherence imagery. *IEEE Transactions on Geoscience and Remote Sensing, 39*(2), 223-232. doi:10.1109/36.905230

Leiterer, R., Torabzadeh, H., Furrer, R., Schaepman, M. E., & Morsdorf, F. (2015). Towards automated characterization of canopy layering in mixed temperate forests using airborne laser scanning. *Forests, 6*(11), 4146-4167. doi:10.3390/f6114146

Levanon, N., & Mozeson, E. (2004). *Radar signals*. Hoboken, New Jersey, USA: John Wiley & Sons.

Lombardini, F., & Griffiths, H. D. (2001). Optimum and suboptimum estimator performance for multibaseline InSAR. *Frequenz, 55*(3-4), 114-118. doi:10.1515/FREQ.2001.55.3-4.114

Lombardo, P., & Lombardini, F. (1997). *Multi-baseline SAR interferometry for terrain slope adaptivity.* Paper presented at the IEEE National Radar Conference, Syracuse, NY, USA. doi:10.1109/NRC.1997.588303

López-Dekker, P., & Mallorquí, J. J. (2010). Capon- and APES-based SAR processing: Performance and practical considerations. *IEEE Transactions on Geoscience and Remote Sensing, 48*(5), 2388-2402. doi:10.1109/TGRS.2009.2038902

Lord, R. T. (2000). *Aspects of Stepped-Frequency Processing for Low-Frequency SAR Systems.* (Ph.D. dissertation), University of Cape Town, Rondebosch, South Africa.

Madsen, S. N. (1989). Estimating the Doppler centroid of SAR data. *IEEE Transactions on Aerospace and Electronic Systems, 25*(2), 134-140. doi:10.1109/7.18675

Magnard, C., Frioud, M., Small, D., Brehm, T., Essen, H., & Meier, E. (2014). Processing of MEMPHIS Ka-Band Multibaseline Interferometric SAR Data: From Raw Data to Digital Surface Models. *IEEE Journal of Selected Topics in Applied Earth Observations and Remote Sensing, 7*(7), 2927-2941. doi:10.1109/JSTARS.2014.2315896

Magnard, C., Frioud, M., Small, D., Brehm, T., & Meier, E. (2016a). Analysis of a maximum likelihood phase estimation method for airborne multibaseline SAR interferometry. *IEEE Journal of Selected Topics in Applied Earth Observations and Remote Sensing, 9*(3), 1072-1085. doi:10.1109/JSTARS.2015.2487685

Magnard, C., Meier, E., Rüegg, M., Brehm, T., & Essen, H. (2007). *High resolution millimeter wave SAR interferometry.* Paper presented at the IEEE International Geoscience and Remote Sensing Symposium (IGARSS), Barcelona, Spain. doi:10.1109/IGARSS.2007.4423999

Magnard, C., Morsdorf, F., Small, D., Stilla, U., Schaepman, M. E., & Meier, E. (2016b). Single tree identification using airborne multibaseline SAR interferometry data. *Remote Sensing of Environment, (submitted)*.

Meier, E., Frei, U., & Nüesch, D. (1993). Precise terrain corrected geocoded images. In G. Schreier (Ed.), *SAR Geocoding: Data and Systems* (pp. 173-186). Karlsruhe, Germany: Wichmann.

Méndez Domínguez, E., Magnard, C., Frioud, M., Small, D., & Meier, E. (2016). Analysis of Adaptive Pulse Compression for Range Focusing in SAR Imagery. *IEEE Journal of Selected Topics in Applied Earth Observations and Remote Sensing, (in preparation)*.

Mette, T., Papathanassiou, K., & Hajnsek, I. (2004). *Biomass estimation from polarimetric SAR interferometry over heterogeneous forest terrain.* Paper presented at the IEEE International Geoscience and Remote Sensing Symposium (IGARSS), Anchorage, AK, USA. doi:10.1109/IGARSS.2004.1369076

Moller, D., Hensley, S., Sadowy, G. A., Fisher, C. D., Michel, T., Zawadzki, M., & Rignot, E. (2011). The Glacier and land ice surface topography interferometer: An airborne proof-of-concept demonstration of high-precision ka-band single-pass elevation mapping. *IEEE Transactions on Geoscience and Remote Sensing, 49*(2), 827-842. doi:10.1109/TGRS.2010.2057254

Moreira, A., Mittermayer, J., & Scheiber, R. (1996). Extended chirp scaling algorithm for air-and spaceborne SAR data processing in stripmap and ScanSAR imaging modes. *IEEE Transactions on Geoscience and Remote Sensing, 34*(5), 1123-1136. doi:10.1109/36.536528

Morsdorf, F., Meier, E., Kötz, B., Itten, K. I., Dobbertin, M., & Allgöwer, B. (2004). LIDAR-based geometric reconstruction of boreal type forest stands at single tree level for forest and wildland fire management. *Remote Sensing of Environment, 92*(3), 353-362. doi:10.1016/j.rse.2004.05.013

Papathanassiou, K. P., & Cloude, S. R. (2001). Single-baseline polarimetric SAR interferometry. *IEEE Transactions on Geoscience and Remote Sensing, 39*(11), 2352-2363. doi:10.1109/36.964971

Perna, S., Wimmer, C., Moreira, J., & Fornaro, G. (2008). X-band airborne differential interferometry: Results of the OrbiSAR campaign over the Perugia area. *IEEE Transactions on Geoscience and Remote Sensing, 46*(2), 489-503. doi:10.1109/TGRS.2007.908871

Praks, J., Antropov, O., & Hallikainen, M. T. (2012). LIDAR-aided SAR interferometry studies in boreal forest: Scattering phase center and extinction coefficient at X-and L-band. *IEEE Transactions on Geoscience and Remote Sensing, 50*(10), 3831-3843. doi:10.1109/TGRS.2012.2185803

Prats, P., Câmara De Macedo, K. A., Reigber, A., Scheiber, R., & Mallorqui, J. J. (2007). Comparison of topography-and aperture-dependent motion compensation algorithms for airborne SAR. *IEEE Geoscience and Remote Sensing Letters, 4*(3), 349-353. doi:10.1109/LGRS.2007.895712

Prats, P., & Mallorqui, J. J. (2003). Estimation of azimuth phase undulations with multisquint processing in airborne interferometric SAR images. *IEEE Transactions on Geoscience and Remote Sensing, 41*(6), 1530-1533. doi:10.1109/TGRS.2003.814140

Prats, P., Reigber, A., & Mallorqui, J. J. (2004). Interpolation-free coregistration and phase-correction of airborne SAR interferograms. *IEEE Geoscience and Remote Sensing Letters, 1*(3), 188-191. doi:10.1109/LGRS.2004.828181

Puliti, S., Ørka, H. O., Gobakken, T., & Næsset, E. (2015). Inventory of Small Forest Areas Using an Unmanned Aerial System. *Remote Sensing, 7*(8), 9632-9654. doi:10.3390/rs70809632

Raksiri, C., & Parnichkun, M. (2004). Geometric and force errors compensation in a 3-axis CNC milling machine. *International Journal of Machine Tools and Manufacture, 44*(12-13), 1283-1291. doi:10.1016/j.ijmachtools.2004.04.016

Reigber, A., Alivizatos, E., Potsis, A., & Moreira, A. (2006). Extended wavenumber-domain synthetic aperture radar focusing with integrated motion compensation. *IEE Proceedings-Radar, Sonar and Navigation, 153*(3), 301-310. doi:10.1049/ip-rsn:20045087

Reigber, A., Jäger, M., Pinheiro, M., Scheiber, R., Prats, P., Fischer, J., Horn, R., & Nottensteiner, A. (2012). *Performance of the P-band subsystem and the X-band interferometer of the F-SAR airborne SAR instrument.* Paper presented at the IEEE International Geoscience and Remote Sensing Symposium (IGARSS), Munich, Germany. doi:10.1109/IGARSS.2012.6352479

Reitberger, J., Schnörr, C., Krzystek, P., & Stilla, U. (2009). 3D segmentation of single trees exploiting full waveform LIDAR data. *ISPRS Journal of Photogrammetry and Remote Sensing, 64*(6), 561-574. doi:10.1016/j.isprsjprs.2009.04.002

Rodriguez, E., & Martin, J. (1992). Theory and design of interferometric synthetic aperture radars. *IEE Proceedings F (Radar and Signal Processing), 139*(2), 147-159. doi:10.1049/ip-f-2.1992.0018

Rosen, P., Hensley, S., Joughin, I. R., Li, F. K., Madsen, S. N., Rodriguez, E., & Goldstein, R. M. (2000). Synthetic aperture radar interferometry. *Proceedings of the IEEE, 88*(3), 333-382. doi:10.1109/5.838084

Ruault Du Plessis, O., Nouvel, J.-F., Baqué, R., Bonin, G., Dreuillet, P., Coulombeix, C., & Oriot, H. (2011). ONERA SAR facilities. *IEEE Aerospace and Electronic Systems Magazine, 26*(11), 24-30. doi:10.1109/MAES.2011.6070278

Rüegg, M., Meier, E., & Nüesch, D. (2007). Capabilities of dual-frequency millimeter wave SAR with monopulse processing for ground moving target indication. *IEEE Transactions on Geoscience and Remote Sensing, 45*(3), 539-553. doi:10.1109/TGRS.2006.888464

Sandberg, G., Ulander, L. M., Fransson, J., Holmgren, J., & Le Toan, T. (2011). L-and P-band backscatter intensity for biomass retrieval in hemiboreal forest. *Remote Sensing of Environment, 115*(11), 2874-2886. doi:10.1016/j.rse.2010.03.018

Scheiber, R. (2004). *Hochauflösende Interferometrie für Radar mit synthetischer Apertur.* (Ph.D. dissertation), Deutsches Zentrum für Luft- und Raumfahrt (DLR), Köln, Germany. (DLR-Forschungsbericht 2004-12)

Schimpf, H., Essen, H., Boehmsdorff, S., & Brehm, T. (2002). *MEMPHIS – a fully polarimetric experimental radar.* Paper presented at the IEEE International Geoscience and Remote Sensing Symposium (IGARSS), Toronto, Canada. doi:10.1109/IGARSS.2002.1026230

Schimpf, H., Wahlen, A., & Essen, H. (2003). High range resolution by means of synthetic bandwidth generated by frequency-stepped chirps. *Electronics Letters, 39*(18), 1346-1348. doi:10.1049/el:20030829

Schmidt, R. O. (1986). Multiple emitter location and signal parameter estimation. *IEEE Transactions on Antennas and Propagation, 34*(3), 276-280. doi:10.1109/TAP.1986.1143830

Schmitt, M., Brück, A., Schönberger, J., & Stilla, U. (2013). *Potential of airborne single-pass millimeterwave InSAR data for individual tree recognition.* Paper presented at the Dreiländertagung DGPF, OVG und SGPF Freiburg im Breisgau, Germany.

Schmitt, M., Shahzad, M., & Zhu, X. X. (2015). Reconstruction of individual trees from multi-aspect TomoSAR data. *Remote Sensing of Environment, 165*, 175-185. doi:10.1016/j.rse.2015.05.012

Schmitt, M., & Stilla, U. (2014a). Adaptive multilooking of airborne single-pass multi-baseline InSAR stacks. *IEEE Transactions on Geoscience and Remote Sensing, 52*(1), 305-312. doi:10.1109/TGRS.2013.2238947

Schmitt, M., & Stilla, U. (2014b). Maximum-likelihood-based approach for single-pass synthetic aperture radar tomography over urban areas. *IET Radar, Sonar & Navigation, 8*(9), 1145-1153. doi:10.1049/iet-rsn.2013.0378

Schmitt, M., & Stilla, U. (2014c). Maximum-likelihood estimation for multi-aspect multi-baseline SAR interferometry of urban areas. *ISPRS Journal of Photogrammetry and Remote Sensing, 87*, 68-77. doi:10.1016/j.isprsjprs.2013.10.006

senseFly. (2014). eBee. *www.sensefly.com/fileadmin/user_upload/sensefly/documents/brochures/eBee_en.pdf*.

Shi, J., & Malik, J. (2000). Normalized cuts and image segmentation. *IEEE Transactions on Pattern Analysis and Machine Intelligence, 22*(8), 888-905. doi:10.1109/34.868688

Small, D. (1998). *Generation of digital elevation models through spaceborne SAR interferometry.* (Ph.D. dissertation), University of Zurich, Zurich, Switzerland.

Small, D., Werner, C. L., & Nüesch, D. (1993). *Baseline modelling for ERS-1 SAR interferometry.* Paper presented at the IEEE International Geoscience and Remote Sensing Symposium (IGARSS), Tokyo, Japan. doi:10.1109/IGARSS.1993.322661

Small, D., Werner, C. L., & Nüesch, D. (1995). Geocoding and validation of ERS-1 InSAR-derived digital elevation models. *EARSeL Advances in Remote Sensing, 4*, 26-39.

Touzi, R., Landry, R., & Charbonneau, F. J. (2004). Forest type discrimination using calibrated C-band polarimetric SAR data. *Canadian Journal of Remote Sensing, 30*(3), 543-551. doi:10.5589/m03-072

Unser, M., Aldroubi, A., & Eden, M. (1993a). B-spline signal processing: Part I – Theory. *IEEE Transactions on Signal Processing, 41*(2), 821-833. doi:10.1109/78.193220

Unser, M., Aldroubi, A., & Eden, M. (1993b). B-spline signal processing: Part II – Efficient design and applications. *IEEE Transactions on Signal Processing, 41*(2), 834-848. doi:10.1109/78.193221

Vasile, G., Trouvé, E., Lee, J.-S., & Buzuloiu, V. (2006). Intensity-driven adaptive-neighborhood technique for polarimetric and interferometric SAR parameters estimation. *IEEE Transactions on Geoscience and Remote Sensing, 44*(6), 1609-1621. doi:10.1109/TGRS.2005.864142

Vu, V. T., Sjögren, T. K., Pettersson, M. I., & Gustavsson, A. (2008). *Definition on SAR image quality measurements for UWB SAR.* Paper presented at the SPIE. doi:10.1117/12.799478

Wahl, D. E., Eichel, P. H., Ghiglia, D. C., & Jakowatz, C. V. (1994). Phase gradient autofocus – a robust tool for high resolution SAR phase correction. *IEEE Transactions on Aerospace and Electronic Systems, 30*(3), 827-835. doi:10.1109/7.303752

Wehr, A., & Lohr, U. (1999). Airborne laser scanning – an introduction and overview. *ISPRS Journal of Photogrammetry and Remote Sensing, 54*(2), 68-82. doi:10.1016/S0924-2716(99)00011-8

Wilkinson, A. J., Lord, R. T., & Inggs, M. R. (1998). *Stepped-Frequency Processing Reconstruction of Target Reflectivity.* Paper presented at the South African Symposium on Comunications and Signal Processing (COMSIG), Rondebosch, South Africa. doi:10.1109/COMSIG.1998.736930

Wimmer, C., Siegmund, R., Schwabisch, M., & Moreira, J. (2000). Generation of high precision DEMs of the Wadden Sea with airborne interferometric SAR. *IEEE Transactions on Geoscience and Remote Sensing, 38*(5), 2234-2245. doi:10.1109/36.868881

Zebker, H. A., & Goldstein, R. M. (1986). Topographic mapping from interferometric synthetic aperture radar observations. *Journal of Geophysical Research: Solid Earth, 91*(B5), 4993-4999. doi:10.1029/JB091iB05p04993

Graduate courses

- Ph.D. Seminar I & II
- Graduate School Retreat I & II

Oral contributions

- Photogrammetric Image Analysis (PIA), 2015, Munich, Germany.
- Progress in Electromagnetics Research Symposium (PIERS), 2012, Kuala Lumpur, Malaysia.
- Swisstopo colloquium, 2012, Bern, Switzerland.
- NATO – Partnership for Peace conference, 2011, Thun, Switzerland.
- IEEE International Geoscience and Remote Sensing Symposium (IGARSS), 2010, Honolulu, HI, USA.
- *Dreiländertagung* OVG, DGPF & SGPF, 2010, Vienna, Austria.
- 7th European Conference on Synthetic Aperture Radar (EUSAR), 2008, Friedrichshafen, Germany.
- IEEE International Geoscience and Remote Sensing Symposium (IGARSS), 2007, Barcelona, Spain.

Teaching

- GEO 443, Lecture SAR III (2010 – 2015)

Publications

Peer-reviewed first author publications:

Magnard, C., Morsdorf, F., Small, D., Stilla, U., Schaepman, M. E., & Meier, E. (2016) Single tree identification using airborne multibaseline SAR interferometry data. *Remote Sensing of Environment, (submitted)*.

Magnard, C., Frioud, M., Small, D., Brehm, T., & Meier, E. (2016). Analysis of a maximum likelihood phase estimation method for airborne multibaseline SAR interferometry. *IEEE Journal of Selected Topics in Applied Earth Observations and Remote Sensing*, *9*(3), 1072-1085.

Magnard, C., Frioud, M., Small, D., Brehm, T., Essen, H., & Meier, E. (2014). Processing of MEMPHIS Ka-Band Multibaseline Interferometric SAR Data: From Raw Data to Digital Surface Models. *IEEE Journal of Selected Topics in Applied Earth Observations and Remote Sensing, 7*(7), 2927-2941.

Other scientific publications

Peer-reviewed publications:

Méndez Domínguez, E., **Magnard, C.,** Frioud, M., Small, D., & Meier, E. (2016). Analysis of Adaptive Pulse Compression for Range Focusing in SAR Imagery. *IEEE Journal of Selected Topics in Applied Earth Observations and Remote Sensing, (in preparation)*.

Schmitt, M., Maksymiuk, O., **Magnard, C.,** & Stilla, U. (2013). Radargrammetric registration of airborne multi-aspect SAR data of urban areas. *ISPRS Journal of Photogrammetry and Remote Sensing, 86*, 11-20.

Schmitt, M., **Magnard, C.,** Stanko, S., Ackermann, C., & Stilla, U. (2013). Advanced High Resolution SAR Interferometry of Urban Areas with Airborne Millimetrewave Radar. *Photogrammetrie-Fernerkundung-Geoinformation, 2013*(6), 603-617.

Henke D., **Magnard C.,** Frioud M., Small D., Meier E., & Schaepman M. E. (2012). Moving-Target Tracking in Single-Channel Wide-Beam SAR. *IEEE Transactions on Geoscience and Remote Sensing, 50*(11), 4735 - 4747.

Frey, O., **Magnard, C.,** Rüegg, M., & Meier, E. (2009). Focusing of airborne synthetic aperture radar data from highly nonlinear flight tracks. *IEEE Transactions on Geoscience and Remote Sensing, 47*(6), 1844-1858.

Conference contributions:

Magnard, C., Small, D., & Meier, E. (2015). *Phase Noise Investigation of Maximum Likelihood Estimation Method for Airborne Multibaseline SAR Interferometry.* Paper presented at the Photogrammetric Image Analysis (PIA), Munich, Germany.

Frey, O., Werner, C. L., Wegmuller, U., Wiesmann, A., Henke, D., & **Magnard, C.** (2013). *A car-borne SAR and InSAR experiment.* Paper presented at the IEEE International Geoscience and Remote Sensing Symposium (IGARSS), Melbourne, VIC, Australia.

Magnard, C., Brehm, T., Essen, H., & Meier, E. (2012). *High resolution MEMPHIS SAR data processing and applications.* Paper presented at the Progress in Electromagnetics Research Symposium (PIERS), Kuala Lumpur, Malaysia.

Schmitt, M., **Magnard, C.,** Brehm, T., & Stilla, U. (2011). *Towards airborne single pass decimeter resolution SAR interferometry over urban areas.* Paper presented at the Photogrammetric Image Analysis (PIA), Munich, Germany.

Magnard, C., Meier, E., Small, D., Essen, H., & Brehm, T. (2010). *Processing of MEMPHIS millimeter wave multi-baseline InSAR data.* Paper presented at the IEEE International Geoscience and Remote Sensing Symposium (IGARSS), Honolulu, HI, USA.

Magnard, C., Frioud, M., & Meier, E. (2010). *Processing, geocoding and mosaicking of MiSAR data.* Paper presented at the Dreiländertagung DGPF, OVG und SGPF, Vienna, Austria.

Frey, O., **Magnard, C.,** Rüegg, M., & Meier, E. (2008). *Focusing SAR data acquired from non-linear sensor trajectories.* Paper presented at the IEEE International Geoscience and Remote Sensing Symposium (IGARSS), Boston, MA, USA.

Magnard, C., Frey, O., Rüegg, M., & Meier, E. (2008). *Improved airborne SAR data processing by blockwise focusing, mosaicking and geocoding.* Paper presented at the 7th European Conference on Synthetic Aperture Radar (EUSAR), Friedrichshafen, Germany.

Frey, O., **Magnard, C.,** Rüegg, M., & Meier, E. (2008). *Non-linear SAR data processing by time-domain back-projection.* Paper presented at the 7th European Conference on Synthetic Aperture Radar (EUSAR), Friedrichshafen, Germany.

Magnard, C., Meier, E., Rüegg, M., Brehm, T., & Essen, H. (2007). *High resolution millimeter wave SAR interferometry.* Paper presented at the IEEE International Geoscience and Remote Sensing Symposium (IGARSS), Barcelona, Spain.

Reports (report authors listed in alphabetical order):

Fagir, J., Frioud, M., **Magnard, C.,** Meier, E., Méndez Domínguez, E., & Schubert, A. (2016). Annual report 2015: SAR Signatures. In, *Report to the Federal Authorities of the Swiss Confederation* (p. 159). Zurich, Switzerland: Remote Sensing Laboratories, Department of Geography, University of Zurich.

Frioud, M., **Magnard, C.,** Meier, E., & Méndez Domínguez, E. (2015). Annual report 2014: Development of a Modular and Flexible SAR Processor. In, *Report to the Federal Authorities of the Swiss Confederation* (p. 94). Zurich, Switzerland: Remote Sensing Laboratories, Department of Geography, University of Zurich.

Frioud, M., **Magnard, C.,** Meier, E., Méndez Domínguez, E., & Schubert, A. (2014). Annual report 2013: SAR Signatures. In, *Report to the Federal Authorities of the Swiss Confederation* (p. 209). Zurich, Switzerland: Remote Sensing Laboratories, Department of Geography, University of Zurich.

Frioud, M., **Magnard, C.,** & Meier, E. (2014). Annual report 2013: Development of a Modular and Flexible SAR Processor. In, *Report to the Federal Authorities of the Swiss Confederation* (p. 70). Zurich, Switzerland: Remote Sensing Laboratories, Department of Geography, University of Zurich.

Frioud, M., **Magnard, C.,** Meier, E., Méndez Domínguez, E., & Schubert, A. (2013). Bericht 2012: SAR-Signaturen. In, *Report to the Federal Authorities of the Swiss Confederation* (p. 131). Zurich, Switzerland: Remote Sensing Laboratories, Department of Geography, University of Zurich.

Frioud, M., **Magnard, C.,** Meier, E., & Méndez Domínguez, E. (2013). Annual report 2012: Development of a Modular and Flexible SAR Processor. In, *Report to the Federal Authorities of the Swiss Confederation* (p. 101). Zurich, Switzerland: Remote Sensing Laboratories, Department of Geography, University of Zurich.

Magnard, C., Meier, E., & Schubert, A. (2012). Bericht 2011: SAR-Signaturen. In, *Report to the Federal Authorities of the Swiss Confederation* (p. 72). Zurich, Switzerland: Remote Sensing Laboratories, Department of Geography, University of Zurich.

Frioud, M., **Magnard, C.,** Meier, E., & Méndez Domínguez, E. (2012). Annual report 2011: Development of a Modular and Flexible SAR Processor. In, *Report to the Federal Authorities of the Swiss Confederation* (p. 125). Zurich, Switzerland: Remote Sensing Laboratories, Department of Geography, University of Zurich.

Magnard, C., Meier, E., & Zuberbühler, L. (2011). Bericht 2010: SAR-Signaturen. In, *Report to the Federal Authorities of the Swiss Confederation* (p. 82). Zurich, Switzerland: Remote Sensing Laboratories, Department of Geography, University of Zurich.

Frey, O., Frioud, M., **Magnard, C.,** & Meier, E. (2011). Annual report 2010: Development of a Modular and Flexible SAR Processor. In, *Report to the Federal Authorities of the Swiss Confederation* (p. 52). Zurich, Switzerland: Remote Sensing Laboratories, Department of Geography, University of Zurich.

Jehle, M., **Magnard, C.,** Meier, E., & Zuberbühler, L. (2010). Bericht 2009: SAR-Signaturen. In, *Report to the Federal Authorities of the Swiss Confederation* (p. 95). Zurich, Switzerland: Remote Sensing Laboratories, Department of Geography, University of Zurich.

Frey, O., Frioud, M., **Magnard, C.,** & Meier, E. (2010). Annual report 2009: Development of a Modular and Flexible SAR Processor. In, *Report to the Federal Authorities of the Swiss Confederation* (p. 67). Zurich, Switzerland: Remote Sensing Laboratories, Department of Geography, University of Zurich.

Magnard, C., Meier, E., & Zuberbühler, L. (2009). Bericht 2008: SAR-Signaturen. In, *Report to the Federal Authorities of the Swiss Confederation* (p. 92). Zurich, Switzerland: Remote Sensing Laboratories, Department of Geography, University of Zurich.

Frey, O., Frioud, M., **Magnard, C.,** & Meier, E. (2009). Annual report 2008: Development of a Modular and Flexible SAR Processor. In, *Report to the Federal Authorities of the Swiss Confederation* (p. 90). Zurich, Switzerland: Remote Sensing Laboratories, Department of Geography, University of Zurich.

Magnard, C., Meier, E., & Zuberbühler, L. (2008). Bericht 2007: SAR-Signaturen. In, *Report to the Federal Authorities of the Swiss Confederation* (p. 56). Zurich, Switzerland: Remote Sensing Laboratories, Department of Geography, University of Zurich.

Frey, O., Frioud, M., **Magnard, C.**, & Meier, E. (2008). Annual report 2007: Development of a Modular and Flexible SAR Processor. In, *Report to the Federal Authorities of the Swiss Confederation* (p. 54). Zurich, Switzerland: Remote Sensing Laboratories, Department of Geography, University of Zurich.

Magnard, C., Meier, E., Schubert, A., & Zuberbühler, L. (2007). Jahresbericht 2006/2007: SAR-Signaturen. In, *Report to the Federal Authorities of the Swiss Confederation* (p. 151). Zurich, Switzerland: Remote Sensing Laboratories, Department of Geography, University of Zurich.

Frey, O., **Magnard, C.,** Meier, E., & Rüegg, M. (2007). Annual report 2006/2007: Development of a Modular and Flexible SAR Processor. In, *Report to the Federal Authorities of the Swiss Confederation* (p. 72). Zurich, Switzerland: Remote Sensing Laboratories, Department of Geography, University of Zurich.

Frey, O., **Magnard, C.,** Meier, E., Rüegg, M., & Weyermann, J. (2007). Jahresbericht 2005/2006: SAR-Signaturen. In, *Report to the Federal Authorities of the Swiss Confederation* (p. 96). Zurich, Switzerland: Remote Sensing Laboratories, Department of Geography, University of Zurich.

ACKNOWLEDGMENTS

I would like to thank the following people and institutions; this thesis would not have been possible without their help and their many contributions.

First, I would like to particularly thank my supervisor Erich Meier. He hugely supported my work along all these years through his involvement, his broad knowledge, his advice and feedback, his imaginative ideas and his never-ending motivation. I am very grateful for his confidence in me, for always being available to discuss issues or ideas, and at the same time for the freedom he gave me to realize my research. I also thank him for the very good working atmosphere at the SARLab that made these years very enjoyable.

I wish to thank David Small for sharing his huge knowledge and experience on SAR interferometry, for his contribution to my research, and for his many and very detailed revisions to draft versions of manuscripts.

Many thanks to Michael Schaepman and Uwe Stilla for their support, their good advice and suggestions. They helped me greatly with their broad knowledge in remote sensing related topics and with their substantial experience in publishing scientific work.

I also would like to thank Klaus Itten and Daniel Nüesch who supported me at the beginning of my time at RSL.

I would like to thank all current and former colleagues at RSL. My special thanks to Max Frioud who greatly contributed to parts of this thesis and generally for his good advice, Maurice Rüegg for his great help at the start of my PhD, Elías Méndez Domínguez, Daniel Henke, Felix Morsdorf, Othmar Frey, Adrian Schubert, Lukas Zuberbühler, Michael Jehle, Philipp Jörg, Reik Leiterer, Jörg Weyermann for the good cooperation, for their advice and for the fruitful discussions. Many thanks to Julian Fagir, Emiliano Casalini and Christoph Rohner for the good atmosphere in the office, Gillian Milani, Hossein Torabzadeh and Gabriela Schaepman-Strüb for their help carrying out eBee measurements. I also wish to thank Rita Ott, Sandra Altorfer, Giulia Ghielmetti, Mathias Kneubühler, Bruno Weber, Damien Markulin and Benjamin Kellenberger for their great support.

Many thanks to armasuisse W+T staff for their financial, technical, logistical and scientific support: in particular Peter Wellig for the long standing support of the SARLab, for linking us to other research institutions, for the organization of acquisition campaigns and research seminars, Christian Sennhauser and Matthias Renker for the good cooperation and for their help during acquisition campaigns.

I would like to thank Fraunhofer/FHR staff, and in particular Thorsten Brehm for the organization and execution of the measurement campaigns with the MEMPHIS sensor. He was always there to fulfill our wishes for the measurement campaigns, to implement the proposed hardware improvements, and to answer my many questions. I also wish to thank Stephan Palm, Stefan Sieger, Anika Maresch and Winfried Johannes for their help carrying out MEMPHIS campaigns, Alfred Wahlen for his deep knowledge of the MEMPHIS system, Manfred Hägelen and Stephan Böhmsdorf for their contributions to MEMPHIS data processing, and Nils Pohl and Stephan Stanko for their support. Finally, a special mention goes to Helmut Essen who sadly passed away in 2013. He led the development of millimeter wave radar systems at Fraunhofer/FHR, with MEMPHIS among them. He was an endless source of ideas for new possibilities, new methods, new applications, and contributed immensely to my PhD thesis.

Many thanks to Antje Thiele from Fraunhofer/IOSB and Karlsruhe Institute of Technology for her help and for the collection of ground truth data during acquisition campaigns.

I would like to thank the following colleagues from the *Technische Universitaet Muenchen*: in particular, Christian Ackermann for lending the IMU hardware and for his invaluable technical assistance, Peter Wasmeier for the measurement of the lever arms on the C-160 Transall, and Michael Schmitt for the good cooperation and sharing of ideas.

I want to acknowledge Wolfgang Schermeier and all other C-160 pilots who flew for our missions with MEMPHIS, as well as Herbert Spies and his ground team at WTD-61 in Manching.

Many thanks to Arthur Gessler, Christian Hug, Peter Jakob, Flurin Sutter, Peter Waldner and the WSL team for performing and providing the measurements at the Vordemwald LWF test site.

I also would like to thank the following institutions for their support: *Bayern Landesamt für Vermessung und Geoinformation*, *Baden-Württemberg Landesamt für Geoinformation und Landentwicklung*, Swisstopo, Allnav AG for their DGPS products and for their assistance using them, Sensefly for the possibilities offered by their small eBee UAV, the OFCOM and Skyguide.

Finally, I would like to extend my thanks to my current and former flat mates Lukas, Agnieszka, Patrik, Ludivine, Aurel, Magdalena, Mike and Pierre who made this time in Zurich very enjoyable, to my friends, and above all I would like to thank my family for their never-ending support.